

NASA TECHNICAL
MEMORANDUM

NASA TM X-73,188

NASA TM X-73,188

(NASA-TM-X-73188) TURBULENCE MODELING FOR
COMPRESSIBLE FLOWS (NASA) 110 p HC A06/MF
A01 CSCL 20D

N77-15341

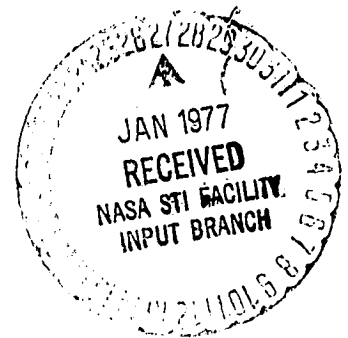
G3/34 11491
Unclas

TURBULENCE MODELING FOR COMPRESSIBLE FLOWS

Joseph G. Marvin

Ames Research Center
Moffett Field, Calif. 94035

January 1977



1. Report No. NASA TM X-73,188	2. Government Accession No.	3. Recipient's Catalog No.	
4. Title and Subtitle TURBULENCE MODELING FOR COMPRESSIBLE FLOWS		5. Report Date	
		6. Performing Organization Code	
7. Author(s) Joseph G. Marvin		8. Performing Organization Report No. A-6849	
9. Performing Organization Name and Address Ames Research Center Moffett Field, Calif. 94035		10. Work Unit No. 505-06-13-01-00-21	
		11. Contract or Grant No.	
12. Sponsoring Agency Name and Address National Aeronautics and Space Administration Washington, D. C. 20546		13. Type of Report and Period Covered Technical Memorandum	
		14. Sponsoring Agency Code	
15. Supplementary Notes			
16. Abstract Material prepared for a short course on "Applications and Fundamentals of Turbulence" given at the University of Tennessee Space Institute, Tullahoma, Tennessee, January 10 and 11, 1977, is presented. A complete concept of turbulence modeling is described and examples of progress for its use in computational aerodynamics is given. Modeling concepts, experiments, and computations using the concepts are reviewed in a manner that provides an up-to-date statement on the status of this problem for compressible flows.			
17. Key Words (Suggested by Author(s)) Viscous flows Compressible turbulent flows Attached and separated flows		18. Distribution Statement Unlimited STAR Category - 34	
19. Security Classif. (of this report) Unclassified	20. Security Classif. (of this page) Unclassified	21. No. of Pages 111	22. Price* \$5.25

COMPRESSIBLE EFFECTS AND MODELING

Joseph G. Marvin

Ames Research Center, NASA

Moffett Field, California 94035

I. INTRODUCTION

The rapid development of faster, larger computers has been paralleled by an equally rapid development of computational aerodynamics. In light of this, it has been suggested that the computer and the wind tunnel will perform equal and complementary roles in the development of new aerospace vehicles.⁽¹⁾ To make that suggestion a reality it will be necessary that the understanding of turbulence be enhanced and that some practical means of modeling it in computations be provided.

Table I is a simplified summary of the status of computational aerodynamics that illustrates its rapid development, particularly since the start of this decade. The stage of approximation of the governing equations has been divided into four progressively more complex categories, culminating with the viscous, time-dependent Navier-Stokes equations. Beginning in the 1930's and progressing through the 1960's, inviscid linearized theory in various refined stages has been used in the design of many aircraft; however, limitations in this theory required that much of the configuration design be accomplished experimentally. In the 1970's, development of inviscid nonlinear theory advanced more rapidly and is now nearing completion.

Computations for transonic and hypersonic flight have been made for realistic aerospace vehicle geometries (notable examples are refs. 2-4). The major limitation of these computations is that they cannot handle separated flows. To provide that capability, the next stage of equation approximation requires utilization of the Navier-Stokes equations or their approximation. For turbulent flows, which are ubiquitous and very important in most aerospace vehicle applications, computations employing the time-averaged Navier-Stokes equations are in the early stages of development. The limitation of these

computations is the accuracy of the turbulence model used to complete the system of governing equations; this item now paces the development.

Once this stage of approximation reaches the point of practical utility, it is expected that the development of computations using the complete Navier-Stokes equations in time-dependent form will begin. However, because the resolution scale for the smaller turbulent eddies precludes the use of any present day computers, an advanced computer is essential before practical computations can be made available. Thus, within the next decade, it would be possible to numerically simulate the flow about aircraft, including important viscous effects, if the ability to model turbulence can be improved.

The Navier-Stokes equations are the basic governing equations used to describe most fluid mechanics phenomena. They also apply to problems involving turbulent flow where turbulence appears as a random, dissipative, three-dimensional phenomenon that involves many characteristic scales. To avoid the difficulty of describing every discrete turbulent motion possible, some type of averaging must be employed. Of the many possibilities, Reynolds time-averaging⁽⁵⁾ has proved the most successful. Time averaging eliminates some information contained in the original equations, however, and also results in more unknowns than governing equations through the introduction of apparent Reynolds stresses for the actual transfer of momentum by velocity fluctuations. Deriving additional equations for those Reynolds stresses only results in the introduction of additional unknowns.

Therefore, the extra unknowns must be represented by physically plausible combinations of quantities for which transport equations are expressed in terms of constants or empirical functions considered as known or expressible in terms of the mean variables. The problem of reducing the unknowns to equal

the number of equations is referred to as the closure problem; the process of expressing the unknowns as transport equations in terms of empirical functions or constants is referred to as "turbulence modeling."

Historically, progress in turbulence modeling has been slow and deliberate, and has relied substantially on a few carefully controlled experiments performed over a range of test conditions. Such experiments could be called "building-block experiments" because they provided the gage for establishing the credibility of computational techniques and even more importantly because they provided physically meaningful concepts that were used to enhance heuristic modeling ideas. The conference on the computation of turbulent flows held at Stanford University in 1968⁽⁶⁾ used these key experiments to assess progress in predicting incompressible, attached, turbulent flows. Later that same year, the conference on compressible turbulent flows held at Langley Research Center⁽⁷⁾ concluded that very few, if any, compressible flow experiments in the building-block category were being performed.

If progress in modeling for compressible flows is to be made, it will also come through combining a broad experimental effort with developments in computational techniques and modeling ideas. For compressible flow, however, progress is even more difficult to achieve because compressibility introduces additional complexities, not only in the modeling concepts, but also in the experiments. The complete concept of turbulence modeling has three elements: experiments, intuitive modeling concepts, and the computer code (see fig. 1). Each element is essential, and the elements are not easily separated.

The process could start with the modeling concept or with the experiments. Historically, the process began with experimental observations that later led to modeling concepts. This trend is beginning to change in that model

développement and experiment are being performed in parallel and coordinated efforts. Once the modeling concepts are established, the computer code can be assembled. This particular sequence is essential for complicated equation systems because the modeling concepts can often alter the order of the equation system or method of solution. Once the code has been established, it can be compared with and verified by the experiments. If the experiments provide enough detail, they can guide changes in the modeling concepts and the process can be continued until the predictive capability of the code is established. An important aspect of the computation code development is that it be directed specifically to the geometry of the experiment and that it use exact experimental initial conditions so that no doubt can be cast on the comparative results.

The status of modeling for compressible flows can be broadly summarized as shown in figure 2. For constant pressure flows, that is, flat plates or bodies of revolution where the boundary layers are thin and the outer inviscid flow can be described, adequate turbulence models are available and there are apparently sufficient data to verify them. Pressure gradients introduce complexities that begin to test our ability to model turbulence. For mild gradients, adjusting the constants in the models that handle constant pressure flows will usually suffice. For severe pressure gradients, however, models are not generally available and there is only a limited range of quality data to verify models now under development. Turbulence models are not yet available for the case when pressure gradients are strong enough to separate the flow, and there are only a limited number of quality experiments for verification.

In the course of this presentation, a concept of turbulence modeling for compressible flows will be reviewed. This review will provide an up-to-date status of the problem and an assessment of the progress being made to solve it. A description of turbulence modeling will be given first, and various modeling concepts will be introduced. Because turbulence modeling relies substantially on experiment, the next section will define what an adequate experiment is, and what the present capabilities of measurement techniques are. In the final section, the status of turbulence modeling for two-dimensional flows will be discussed and examples will be given for attached and separated flow problems.

II. MODELING CONCEPTS FOR COMPRESSIBLE FLOWS

Before describing the various concepts for the turbulence modeling used later in describing the status of modeling for compressible flows it is worthwhile to show briefly how they were developed from the basic governing equations.

A. Governing Equations in Mass-Averaged Variables

The Navier-Stokes equations for a compressible, heat conducting, perfect gas may be written as follows:

Continuity

$$\frac{\partial \rho}{\partial t} + \frac{\partial}{\partial x_j} (\rho u_j) = 0 \quad (1)$$

Momentum

$$\frac{\partial}{\partial t} (\rho u_i) + \frac{\partial}{\partial x_j} (\rho u_i u_j) = - \frac{\partial p}{\partial x_i} + \frac{\partial}{\partial x_j} \tau_{ij} \quad (2)$$

Energy

$$\frac{\partial}{\partial t} (\rho h) + \frac{\partial}{\partial x_j} (\rho h u_j) = \frac{\partial p}{\partial t} + u_j \frac{\partial p}{\partial x_j} + \tau_{ij} \frac{\partial u_i}{\partial x_j} - \frac{\partial q_j}{\partial x_j} \quad (3)$$

where the stress tensor τ_{ij} and the heat flux vector q_j are given by

$$\tau_{ij} = \lambda \delta_{ij} \frac{\partial u_k}{\partial x_k} + \mu \left(\frac{\partial u_i}{\partial x_j} + \frac{\partial u_j}{\partial x_i} \right) \quad (4)$$

$$q_j = -k \frac{\partial T}{\partial x_j} \quad (5)$$

The bulk viscosity λ is equal to $-2/3 \mu$, where μ is the dynamic viscosity; the thermal conductivity is k ; δ_{ij} is the Kronecker delta, equaling 1 when $i = j$ and equaling 0 when $i \neq j$. A summation is implied when indices are repeated.

As is well known, when dealing with flows that are turbulent, the solution to equations (1) through (3) becomes practical only if one employs some type of averaging. Following Reynolds, for example, the equations are averaged over a time that is long compared to the time associated with the predominant frequencies of the turbulence. For compressible flows, however, mass-weighted averaging is often used, rather than the usual time averaging, because the compressible form of the equations can be reduced to a form analogous to the incompressible form (see, e.g., ref. 8).

The advantage of mass averaging can be illustrated as follows. In the usual averaging procedure, velocity is usually written

$$u_i(x_i, t) = \overline{u_i(x_i)} + u_i''(x_i, t) \quad (6)$$

where the bar denotes the time average of $u_i''(x_i, t)$. The time average of a quantity is obtained from

$$\bar{Q} = \lim_{\Delta t \rightarrow \infty} \frac{1}{\Delta t} \int_{t_0}^{t_0 + \Delta t} Q(t) dt \quad (7)$$

Introducing the concept of time averaging into the continuity and momentum equations, the following equations result:

$$\frac{\partial \bar{\rho}}{\partial t} + \frac{\partial}{\partial x_j} (\bar{\rho} \bar{u}_j + \overline{\rho'' u_j''}) = 0 \quad (8)$$

$$\begin{aligned} \frac{\partial}{\partial t} (\bar{\rho} \bar{u}_i + \overline{\rho'' u_i''}) + \frac{\partial}{\partial x_j} (\bar{\rho} \bar{u}_i \bar{u}_j + \overline{u_i \rho'' u_j''}) = & - \frac{\partial \bar{p}}{\partial x_i} \\ & + \frac{\partial}{\partial x_j} (\bar{\tau}_{ij} - \bar{u}_j \overline{\rho'' u_i''} - \overline{\rho u_i'' u_j''} - \overline{\rho'' u_i'' u_j''}) \end{aligned} \quad (9)$$

Note that for incompressible flows $d\rho = 0$ and the equations reduce to the familiar incompressible form. However, aside from the usual problem of supplying additional relationships for the mean effects of turbulence, for example, $\overline{\rho u_i'' u_j''}$, the compressible form of the equations contains fluctuating density-generated terms such as $\overline{\rho'' u_j''}$. This complexity can be formally avoided by introducing mass-weighted averaging.

Define the following mass-weighted velocity

$$\tilde{u}_i = \overline{\rho u_i} / \bar{\rho} \quad (10)$$

where the bar denotes the usual time-averaged value and the tilde denotes mass-weighted averaging. The instantaneous velocity can be written

$$u_i(x_i, t) = \tilde{u}_i(x_i) + u_i'(x_i, t) \quad (11)$$

where u_i' is the superimposed velocity fluctuation. The relation between $\overline{u_i}$ and \tilde{u}_i is obtained as follows:

$$\overline{\rho u_i'(x_i)} = \overline{(\bar{\rho} + \rho'') u_i'(x_i)} = 0$$

or

$$\overline{u_i'(x_i)} = -\overline{\rho'' u_i'(x_i)} / \bar{\rho}$$

Taking the average of equation (11) and rearranging

$$\tilde{u}_i(x_i) - \overline{u_i(x_i)} = -\overline{u_i'(x_i)}$$

or

$$\tilde{u}_i(x_i) - \overline{u_i(x_i)} = \overline{\rho'' u_i'(x_i)} / \bar{\rho}$$

From the definition of $u_i(x,t)$ it follows that

$$\tilde{u}_i(x_i) + u_i'(x_i, t) = \overline{u_i(x_i)} + u_i''(x_i, t)$$

Multiplying by ρ and averaging

$$\bar{\rho} \tilde{u}_i(x_i) + \overline{\rho u_i'}(x_i) = \bar{\rho} \bar{u}_i + \overline{\rho u_i''}(x_i)$$

But $\overline{\rho u_i'}(x_i) = 0$ and $\overline{\rho u_i''}(x_i)$ can be written $(\bar{\rho} + \rho'') \bar{u}_i'' = \bar{\rho}'' \bar{u}_i''$, so it follows that

$$\tilde{u}_i(x_i) - \overline{u_i(x_i)} = \bar{\rho}'' \bar{u}_i'' / \bar{\rho} \quad (12)$$

Thus the difference between the mass-weighted and time-averaged velocities depends on a density-velocity correlation. Similar relationships exist for temperature and enthalpy. Later, relationships between various shear stress and heat flux quantities in mass-weighted and time-averaged systems will be needed. Without derivation, these are written as follows:

$$\overline{\rho u' v'} = \overline{\rho u'' v''} - \frac{\overline{\rho'' v''} \overline{\rho'' u''}}{\bar{\rho}} \quad (12a)$$

$$\overline{\rho v' h'} = \overline{\rho v'' h''} - \frac{\overline{\rho'' v''} \overline{\rho'' h''}}{\bar{\rho}} \quad (12b)$$

Substituting mass-averaged variables into equations (1) to (3) yields:

Continuity

$$\frac{\partial \bar{\rho}}{\partial t} + \frac{\partial}{\partial x_j} (\bar{\rho} \tilde{u}_j) = 0 \quad (13)$$

Momentum

$$\frac{\partial}{\partial t} (\bar{\rho} \tilde{u}_i) + \frac{\partial}{\partial x_j} (\bar{\rho} \tilde{u}_i \tilde{u}_j) = - \frac{\partial \bar{p}}{\partial x_i} + \frac{\partial}{\partial x_j} (\bar{\tau}_{ij} - \overline{\rho u_i' u_j'}) \quad (14)$$

Energy

$$\frac{\partial}{\partial t} \bar{\rho} \tilde{h} + \frac{\partial}{\partial x_j} (\bar{\rho} \tilde{h} \tilde{u}_j) = \frac{\partial \bar{p}}{\partial t} + \tilde{u}_j \frac{\partial \bar{p}}{\partial x_j} + \overline{u_j' \frac{\partial p}{\partial x_j}} + \frac{\partial}{\partial x_j} (-\bar{q}_j - \overline{\rho h' u_j'}) + \overline{\tau_{ij} \frac{\partial u_i}{\partial x_j}} \quad (15)$$

Equations (13) to (15) now have the same form as the laminar Navier-Stokes equations except that the averaged variables appear throughout and the so-called turbulent Reynolds stresses and heat fluxes appear. The equations are simpler than those given when the usual time averaging is introduced. These equations also have the same form as the incompressible time-averaged equations except that the so-called Reynolds stresses, $-\overline{\rho u_i' u_j'}$, include fluctuations in density. This latter fact does indeed complicate the process of modeling the turbulence.

The equations in their averaged form have additional unknowns: the turbulent Reynolds stresses and heat fluxes. The problem of reducing the number of unknowns to equal the number of equations is called the closure problem. The process of expressing the unknowns as transport equations or functions in terms of known quantities is called turbulence modeling.

The governing equations can be supplemented by additional equations for the turbulent kinetic energy and the various Reynolds stresses.⁽⁹⁾ Following the development in chapter 2 of reference 9, these may be written as:

Turbulent Kinetic Energy

$$\frac{\partial}{\partial t} \left(\frac{1}{2} \overline{\rho u_i' u_i'} \right) + \frac{\partial}{\partial x_k} \tilde{u}_k \left(\frac{1}{2} \overline{\rho u_i' u_i'} \right) + \frac{\partial}{\partial x_k} u_k' \left(\frac{1}{2} \overline{\rho u_i' u_i'} \right) = -\overline{u_i' \frac{\partial p}{\partial x_i}} + \overline{u_i' \frac{\partial \tau_{ik}''}{\partial x_k}} - \overline{\rho u_i' u_k'} \frac{\partial \tilde{u}_i}{\partial x_k} \quad (16)$$

Reynolds Stresses

$$\begin{aligned} \frac{\partial}{\partial t} (\overline{\rho u_i' u_j'}) + \frac{\partial}{\partial x_k} \tilde{u}_k (\overline{\rho u_i' u_j'}) + \frac{\partial}{\partial x_k} (\overline{\rho u_i' u_j' u_k'}) = & -\overline{u_j' \frac{\partial p}{\partial x_i}} - \overline{u_i' \frac{\partial p}{\partial x_j}} \\ & + \overline{u_j' \frac{\partial \tau_{ik}''}{\partial x_k}} + \overline{u_i' \frac{\partial \tau_{jk}''}{\partial x_k}} - \overline{\rho u_i' u_k'} \frac{\partial \tilde{u}_j}{\partial x_k} - \overline{\rho u_j' u_k'} \frac{\partial \tilde{u}_i}{\partial x_k} \end{aligned} \quad (17)$$

Inspection of the conservation equations shows that the number of unknowns exceeds the number of equations. Thus, the next step in arriving at a closed

set of equations will be to model certain of the terms. This can be accomplished in progressively more complex steps in the same manner as for incompressible flows.

B. Modeling Concepts

1. An Algebraic Closure Model

A straightforward technique that has received much attention and verification for a broad range of boundary-layer flows is to express the turbulent shear stress and heat flux in terms of the mean flow variables. Bousinesq's eddy viscosity concept is introduced. Define the turbulent Reynolds stress tensor as

$$\bar{R}_{ij} = -\rho \overline{u_i' u_j'}$$

then let

$$\bar{R}_{ij} = \hat{\epsilon} \left(\frac{\partial \bar{u}_i}{\partial x_j} + \frac{\partial \bar{u}_j}{\partial x_i} \right) \quad (18)$$

where $\hat{\epsilon}$ is considered a scalar quantity referred to as the eddy viscosity because equation (18) now has the same form as the laminar stress tensor, τ_{ij} . The problem of modeling is now reduced to one of describing the behavior of the eddy viscosity in terms of the mean flow variables. Several techniques for accomplishing this when the flow is compressible are described below. Essentially they are extensions of techniques used for incompressible flows.

A successful model was developed by Cebeci and Smith. It uses Prandtl's mixing-length hypothesis (i.e., $\hat{\epsilon} = \ell^2 [(\partial \bar{u}_i / \partial x_j) + (\partial \bar{u}_j / \partial x_i)]$) in the inner region with Clauser's eddy viscosity in the outer region to arrive at a two-layer model.⁽⁹⁾ Also, in order to appropriately model the region of the sub-layer and the inner log-law region, van Driest's damping function is

introduced. The model has been successfully applied to many compressible equilibrium turbulent boundary-layer flows.

Inner region

$$\hat{\epsilon}_{inner} = \bar{\rho} (kyD)^2 \left(\frac{\partial u_i}{\partial x_j} + \frac{\partial u_j}{\partial x_i} \right) \quad (19)$$

Outer region

$$\hat{\epsilon}_{outer} = 0.0168 \bar{\rho}_e \bar{u}_e \delta_k^* / 1 + 5.5(y/\delta)^6 \quad (20)$$

where

$$D = [1 - \exp(-y/A)] \quad (21)$$

and

$$A = A^+ \nu (\tau_w / \bar{\rho}_r)^{1/2} \quad (22)$$

and

$$\delta_k^* = \int_0^{y_{edge}} (1 - u/u_e) dy \quad (23)$$

Following Morkovin's hypothesis that compressibility does not affect the description of the length scales, the constants in equations (19) to (23) are given values derived for use in incompressible flows. In equation (22), A^+ contains a reference density which the originators assume to be the local density across the sublayer and in most applications the wall density is used to represent this reference value. The value of A^+ can be adjusted to account for pressure gradient and mass transfer at a wall in the same way as for incompressible flows. (See chapter 6 of ref. 9 for a discussion and suitable derivation of eq. (22) for compressible flows.) Hereafter, this model with $A^+ = 26$ will be referred to as the baseline turbulence model.

For flows with compressibility it is also required that the energy equation be solved. To express the turbulent heat flux an eddy conductivity is introduced and a turbulent Prandtl number is formed

$$\text{Pr}_t = \frac{\hat{\epsilon}}{\epsilon_h} \quad (24)$$

Expressions for the turbulent Prandtl number have been developed for boundary-layer applications. (See, e.g., chapter 6 of ref. 9.)

2. An Algebraic Closure Model with Relaxation

The baseline turbulence model is not always successful. For equilibrium turbulent flows with mild wall pressure gradient, modifications to Λ^+ will usually result in adequate predictions, but for flows with rather severe pressure gradients, such as those ahead of separation where the flow is not in turbulent equilibrium, modifications to the model are required. Recently, several studies have shown limited improvements for these situations can be obtained by introducing the concept of relaxation. See, for example, references 10 and 11. An additional differential equation for eddy viscosity has been written as

$$\frac{d\epsilon}{dx} = \frac{\epsilon - \epsilon_{eq}}{L} \quad (25)$$

where L is some relaxation length and ϵ_{eq} is the eddy viscosity given by the usual prescription, for example, equations (19) to (23). Some authors have applied the relaxation concept to the outer eddy viscosity only, arguing that the smaller eddies in an inner region should be able to adjust immediately to changes in the mean flow.^(10,11) Another author applied the concept across the entire boundary layer.⁽¹²⁾ In either case, the relaxation concept is introduced to account for the experimentally observed fact that turbulence

cannot adjust instantaneously to changes in the mean flow. However, this particular relaxation concept has not been successfully generalized and the relaxation length scale, L , usually expressed in terms of boundary-layer thicknesses, is not universal. Examples employing this concept will be shown later. Hereafter this model will be referred to as the relaxation model.

3. A Single Transport Equation Model

A more straightforward approach to modeling for nonequilibrium turbulent flows is to introduce the transport equations for Reynolds stresses. The approach is much more complicated than for incompressible flow, however, because terms involving compressibility must also be modeled. Little experimental evidence is available to help in this latter process. To illustrate the problem, the development of these additional modeled terms for the one-equation model derived in reference 13 is briefly described. The eddy viscosity in this application is formed from the product of an algebraic length scale, expressed in terms of a turbulent Reynolds number, and a velocity formed from a solution of the turbulent kinetic energy equation. The method is an extension of Glushko's incompressible model.⁽¹⁴⁾

A more general scalar eddy-viscosity relationship, described by Hinze,⁽¹⁵⁾ wherein the average turbulence pressure is extracted from the stresses, can be written for the turbulent stresses.

$$\bar{R}_{ij} = -\frac{2}{3} \delta_{ij} \bar{\rho} \bar{k} + \hat{\epsilon} \left(\frac{\partial \tilde{u}_i}{\partial x_j} + \frac{\partial \tilde{u}_j}{\partial x_i} \right) \quad (26)$$

where

$$\bar{k} = \frac{1}{2\bar{\rho}} \overline{\rho u_i' u_i'} \quad (26a)$$

Introducing equation (26a) into equation (16) and restructuring the terms involving velocity-pressure gradient and velocity-shear stress correlations, the following turbulent kinetic energy equation is obtained:

$$\begin{aligned} \frac{\partial}{\partial t} (\bar{\rho} \bar{k}) + \frac{\partial}{\partial x_j} (\bar{\rho} u_j \bar{k}) = & -\overline{\rho u_i' u_k'} \frac{\partial \bar{u}}{\partial x_k} - \frac{\partial}{\partial x_k} \overline{\rho u_i' k} - \frac{\partial}{\partial x_i} (\overline{u_i' p}) \\ & + \bar{p} \frac{\partial \overline{u_i'}}{\partial x_i} + \frac{\partial}{\partial x_k} \overline{u_i' \tau_{ik}} - \overline{\tau_{ik} \frac{\partial u_i'}{\partial x_k}} \end{aligned} \quad (27)$$

The turbulent kinetic energy equation in the mass-weighted averaged system has the same form as the incompressible equation but the problem of modeling the terms on the right-hand side of equation (27) differs from the incompressible approach because extra pressure velocity correlations and molecular-shear and velocity correlations are introduced through the mass-weighted averaging process. (See ref. 13 for a complete discussion.) To exemplify this, consider the pressure-velocity correlations. Substituting $p = \bar{p} + p''$ into those terms results in the following group of terms

$$\overline{p v} = - \frac{\partial}{\partial x_i} (\overline{u_i' \bar{p}}) - \frac{\partial}{\partial x_i} \overline{u_i' p''} + \bar{p} \frac{\partial \overline{u_i'}}{\partial x_i} + p'' \frac{\partial \overline{u_i'}}{\partial x_i} \quad (28)$$

Both $\overline{u_i'}$ and its derivative are zero for an incompressible flow and only the second term on the right-hand side remains; it is usually grouped with the second term on the right-hand side of equation (27) and modeled in terms of a gradient of \bar{k} . (See chapter 5 of ref. 9.) The choice for compressible flow is either to assume that these remaining correlations are negligible or to model them in such a way that they tend to zero when the flow is incompressible. Following the procedure of reference 13, rewrite equation (28) as

$$\overline{p v} + \frac{\partial}{\partial x_i} \overline{u_i' p''} = -\overline{u_i'} \frac{\partial \bar{p}}{\partial x_i} + p'' \frac{\partial \overline{u_i'}}{\partial x_i}$$

Equations for $\overline{u_1'}$ have been obtained for two cases: one based on the assumption of constant total temperature within an eddy and the other based on the assumption that the state variables in an eddy behave in a polytropic fashion. In either case, generality is maintained by assuming that pressure fluctuations can be expressed in terms of density and temperature fluctuations. Assuming that the gas behaves in a polytropic manner, then

$$\frac{p''}{\bar{p}} = n \frac{\rho''}{\bar{\rho}} = \frac{n}{n-1} \frac{T'}{\bar{T}} \quad (29)$$

where n is the polytropic coefficient and terms of second order are neglected. Using this expression to relate pressure and temperature, Rubesin arrived at the following equations

$$\overline{u_1'} = \frac{\gamma-1}{n-1} \frac{\epsilon_h}{\bar{\rho} \bar{a}^2} \frac{\partial \bar{h}}{\partial x_1} \quad (30)$$

and

$$\overline{p'' \frac{\partial u_1'}{\partial x_1}} = \xi \bar{p} \frac{\bar{u}_1^2}{\bar{a}^2} \frac{\bar{k}}{\bar{a}^2} \frac{\partial \bar{u}_j}{\partial x_j} \quad (31)$$

where a is a speed of sound and ξ is a coefficient also containing the polytropic exponent. Thus, it is possible to arrive at expressions for the additional correlation terms introduced by compressibility, but they must also be modeled through the introduction of values for n and ξ . The appropriateness of the values suggested by Rubesin, however, has not yet been demonstrated. Experimental measurements of the terms are not available, and the model is only now being tested extensively against experiment.

The complete equations describing the one-equation model are given by equations (75) through (91) of reference 13; they will not be repeated here. Examples shown later refer to this as the 1-equation model.

4. A Two Equation Model

A more generalized model can be developed by forming an eddy viscosity from a velocity and length scale that are both described by transport equations. For example, the previous one-equation model could be generalized to a two-equation model by providing one additional transport equation for the length scale as originally proposed by Rotta.⁽¹⁶⁾

Another approach that is receiving close attention now and for which some results will be presented later is the two-equation model recently developed by Wilcox⁽¹⁷⁾ for the boundary-layer approximations to the Navier-Stokes equations. This model uses an energy equation and a dissipation-rate equation that is a modified form of Saffman's pseudo-vorticity equation. Compressibility has been introduced through mass-weighted averaging as described previously. The modeled form of the equations developed in reference 17 are

$$\frac{\partial}{\partial t} (\bar{\rho} \bar{k}) + \frac{\partial}{\partial x_j} (\bar{\rho} \tilde{u}_j \bar{k}) = \left(\alpha^* \bar{\rho} \frac{\partial \tilde{u}}{\partial y} - \beta^* \omega \right) \bar{k} + \frac{\partial}{\partial y} \left[(\bar{\mu} + \sigma^* \bar{\rho} \epsilon) \frac{\partial \bar{k}}{\partial y} \right] - \xi^* \bar{\rho} \bar{k} \frac{\partial \tilde{u}_k}{\partial x_k} \quad (32)$$

and

$$\begin{aligned} \frac{\partial}{\partial t} \left[\bar{\rho} \left(\frac{\omega}{\bar{\rho}^m} \right)^2 \right] + \frac{\partial}{\partial x_j} \left[\bar{\rho} \tilde{u}_j \left(\frac{\omega}{\bar{\rho}^m} \right)^2 \right] = & \left\{ \alpha \bar{\rho} \frac{\partial \tilde{u}}{\partial y} - \left[\beta + 2\sigma \left(\frac{\partial \tilde{u}}{\partial x_k} \right)^2 \right] \omega \right\} \left(\frac{\omega}{\bar{\rho}^m} \right)^2 \\ & + \frac{\partial}{\partial y} \left[(\bar{\mu} + \sigma \bar{\rho} \epsilon) \frac{\partial}{\partial y} \left(\frac{\omega}{\bar{\rho}^m} \right)^2 \right] \end{aligned} \quad (33)$$

where the term containing ξ^* is an additional term that includes the dilatation of the mean flow due to compressibility and where the eddy diffusivity $(\hat{\epsilon}/\rho)$ is

$$\epsilon = \frac{\bar{\rho} \bar{k}}{\omega}$$

In their latest interpretation, Wilcox and Tracy identify \bar{k} with $9/4 \bar{v}^2$, rather than the turbulent kinetic energy. Thus, inherent in their

model interpretation is the assumption that $((u')^2) : ((w')^2) : ((v')^2) = 4:3:2$. The examples to be presented later will handle the additional compressible modeling terms ξ and m by choosing zero for both and thus reducing the equations to their form that is usually associated with incompressible flow. Thus, compressibility is accounted for only through introduction of the mean density. Examples given later refer to this model as the Wilcox-Tracy model.

5. A Complete Reynolds Stress Model

Applications of the modeled form of the full Reynolds stress equations have also been attempted for compressible flows. See for example reference 18 where Donaldson's invariant modeling ideas are applied to a compressible flow. Donaldson's approach has been receiving focused attention recently for boundary-layer flows and some examples are presented later. Rather than employing mass-weighted variables, this approach begins with the complete time-averaged Navier-Stokes equations and closure is accomplished by modeling the third- and fourth-order correlations in terms of the mean variables and second-order correlations according to the principles of invariant modeling. For the sake of brevity, the equations and the modeled terms will not be given since they comprise a set of 12 equations and 12 unknowns. The reader is referred to references 19 and 20 for a discussion and formal representation of the equations. For the examples to be given later, all the modeling constants were taken from reference 19 and were not adjusted. Later, this model is referred to as the ARAP model.

III. EXPERIMENTS FOR TURBULENCE MODELING

Turbulence modeling is heuristic by nature and therefore requires extensive experimental data for guidance and verification. While there is a rather

extensive data base to support modeling for incompressible flows, the data base for supporting compressible flow modeling is rather small. Only recently has there been a concerted attempt to rectify this imbalance.⁽²¹⁾ A significant contributor to this rather unfortunate imbalance is the difficulty of measurement when Mach number must be considered. In this section the elements of experiments to support modeling will be discussed, the status of measurement techniques will be described, and an experimental foundation for developing a model that will be useful for computing two-dimensional flow fields will be proposed.

A. Elements of Experiments Supporting Modeling

Figure 3 shows the Mach-Reynolds number domain for aerospace vehicles and it gives an indication of the range of conditions over which adequate turbulence modeling must be provided if the concept of numerical simulations of flow fields over complete aircraft is to become a reality. The upper limit on Reynolds number based on vehicle length⁽²²⁾ is shown as well as the upper limit based on a typical wing chord. Mach number varies between subsonic and hypersonic, encompassing the range encountered by commercial passenger vehicles and NASA's space shuttle vehicle. Experiments that verify and guide the modeling process will have to be performed over this range of conditions.

Experiments that support the modeling process can be classified according to the type of closure proposed. Bradshaw⁽²³⁾ broadly classified these closures as first and higher order. First-order closures correspond to closures where second-order correlations like the Reynolds stresses are expressed in terms of first-order correlations like the mean velocity, namely, algebraic mixing length or eddy viscosity formulations. Higher-order closures

refer to those in which third- and higher-order correlations are expressed in terms of second- and higher-order correlations by introducing additional appropriate transport equations.

Table II gives the elements of the experiments required, depending on the type of equation closure. By their nature, verification experiments require documentation of mean and surface quantities over the practical ranges of flight Mach and Reynolds numbers. These experiments are useful for any closure technique used. First-order modeling experiments are those that require measurements of the shear stress and heat fluxes across the flow field because these quantities provide insight into concepts used to model these terms and provide closure.

Such experiments can, but need not be, attempted over the complete Mach and Reynolds number ranges because the verification experiments can test the ability of the model to perform outside the domain where, for example, the shear stresses have been measured. But they must be performed at Reynolds numbers sufficiently high to establish fully developed turbulence. Higher-order modeling experiments require that fluctuating measurements be made across the flow field. Depending on the order of the closure, more and more information on the fluctuating field must be ascertained. As was the case for first-order modeling experiments, data need not be acquired over the complete Mach and Reynolds number domain, provided that verification experiments are available. Ideally, one well-conceived experiment could suffice for all three types listed in table II. Moreover, the same experimental apparatus and instrumentation can be used to eliminate experimental uncertainties. Coles⁽²⁴⁾ emphasized this latter aspect when commenting on the flows used as the basis for the Stanford Conference. He also emphasized the need for a reference

measurement, complete documentation for future reference, and the elimination of three-dimensional uncertainties by, for example, testing axisymmetric configurations.

As mentioned previously, there are few experiments suited to guide and verify turbulence modeling for compressible flows. Figure 4 compares the domain of available experiments that can be used to test modeling concepts with that for vehicles. The shaded area represents the domain where partially documented experiments were performed for flows where zero- or mild-pressure gradients were impressed on the flow. Reference 25 presents a table summarizing most of these experiments and their measurements. In almost all cases, the experiments were performed at low Reynolds numbers and their documentation was incomplete; that is, some experiments measured only a single quantity and no single experiment was complete, at least not insofar as including all the elements listed in table II is concerned. It has been difficult for analysts to use these experiments to predict confidently the trends in Reynolds numbers for actual flight conditions; nevertheless, there appear to be sufficient data of the verification variety to make definite conclusions regarding the ability to model turbulence for attached flow boundary layers near equilibrium as will be shown subsequently.

The unshaded area in figure 4 represents the domain of more recent experiments where shock-induced separation was studied and where specific attempts to document the complete flow field features, including the turbulent fluctuations and their correlations, have been made or are under way. These latter experiments and companion computations, which together are being used to establish adequate turbulence models, are discussed later.

Before discussing any of these experiments, the question of what can be accomplished experimentally in compressible flows where the difficult test environment of high Reynolds numbers and high Mach numbers is present must be addressed. Over the last several years, a considerable amount of instrument development has been undertaken that tends to make expectations optimistic in this regard.

B. Status of Measurement Techniques

1. Mean Flow Measurements

Mean flow measurements of the type required for verification experiments will not be discussed in detail. It suffices to say that in most instances means are at hand to measure mean-flow quantities such as velocity, pressure and temperature, and wall values of heat transfer. It is worth mentioning, however, a recent development in the technique for measuring skin friction which heretofore has been difficult in cases where pressure gradients are applied.

Ludweig's concept of measuring surface shear with a heated surface element has been reintroduced recently by Rubesin et al.⁽²⁶⁾ for use in compressible flows with rather severe pressure gradients. By imbedding small diameter wires (1 mil) in a low conductivity material contoured to the shape of the model surface, it has been possible to obtain reasonably accurate measurements of surface shear. These gages have the distinct advantage of being small in size, insensitive to pressure gradient, and they can be used whether the flow is laminar or turbulent. A disadvantage is that they must be calibrated over a range of appropriate conditions in situ, but so far this has not been a major problem. Examples of such measurements will be given later.

2. Shear Stress Measurements

In addition to mean-flow measurements shear stress distributions will be required for first-order modeling experiments. For zero pressure gradient boundary-layer flows at supersonic speeds, momentum-balance techniques using mean flow-field data have been used successfully to extract the magnitude and distribution of the shear stress. Using this technique, Sandborn was able to show that the appropriately normalized shear stress was essentially independent of Mach number and Reynolds number in the supersonic speed regime to $M \approx 7$.⁽²⁷⁾ The results are shown in figure 5 taken from reference 27. The shaded region represents the distributions from 14 different experiments covering Mach numbers between 2 and 7 and Reynolds numbers, based on momentum thickness, between 2,500 and 12,000. At higher Mach numbers the picture is not so clear, but this may be a direct result of the fact that most of the higher Mach number data were taken on nozzle walls where the boundary layer had undergone distortion by severe pressure gradients in the throat regions. Any proposed turbulence model for zero pressure gradient flows should be able to predict the normalized shear distribution in figure 5. Another important contribution of this universal shear distribution is that it can also be used as a standard against which other direct measurement techniques can be tested, as will be shown subsequently.

Unfortunately, when pressure gradients are imposed on the boundary layers, momentum-balance techniques that employ mean profile measurements are usually not satisfactory for evaluating the magnitude of the shear stresses. This is particularly true when gradients that lead to separation are imposed because the shear stresses comprise only a small part of the overall momentum balance; unfortunately, the shear stresses are the important stresses that determine

the eventual state of the flow field. Therefore, methods for measuring the shear stresses directly must be developed. Hot-wire anemometers and laser velocimeters have recently been used for this purpose and it is important to briefly review their applications and limitations.

Two major problems arise when employing hot-wire anemometers in compressible flows where high Reynolds numbers and Mach numbers are present. The first of these is the practical problem of wire durability. The second and obviously most important is the measurement interpretation.

Mikullá and Horstman⁽²⁸⁾ and subsequently Máteer and Brosh⁽²⁹⁾ developed "backed" wire probes that successfully eliminated the problems associated with wire durability. Sketches of the two probes taken from these references are shown in figures 6 and 7. The dual-wire wedge probe and the separate cross-wire wedge probe were used to obtain measurements of mass flow and vertical velocity fluctuation, and their correlation. The triple-wire probe was used to obtain the correlation of total temperature and vertical velocity fluctuations. The dual-wire probes were operated with constant temperature anemometer systems; the normal wire of the triple-wire probe was operated with a constant current system. Frequency response was considered adequate (50 kHz).

Backing the wires in this manner eliminated wire breakage and strain gaging problems; it permitted operation of cross-wires at high overheats without causing sag and maintained the wires at 45° angles so that vertical velocity fluctuations could readily be obtained when the probe was positioned in a plane normal to the wall. The main disadvantage of these backed wires was the possibility of heat conduction between the wires through the backing material; such conduction could affect the mass-flow sensitivity calibration. For the high Mach number applications of Mikullá and Horstman,⁽²⁸⁾ conduction between

the wires was sufficient to preclude a sensitivity calibration during steady-state operation because the wires were operated at temperatures significantly higher than the test total temperature (1500°R). Mikulla and Horstman were, however, able to infer the sensitivity calibration by operating the backed wire in a known boundary-layer flow previously measured with an unbacked normal wire. By relating their previously measured mass-flow fluctuations to the voltage output from the dual wire, they could infer the sensitivity coefficients. Fortunately the probe of Mateer and Brosh⁽²⁹⁾ was operated at a lower temperature and was not affected by this problem; consequently, they were able to calibrate directly.

Extracting turbulence information from hot wires operated in compressible flows can be accomplished in a straightforward manner. However, certain assumptions are inherent in the process and they require some explanation. Following Morkovin,⁽³⁰⁾ the expression for wire voltage fluctuations is written

$$\frac{E''}{E} = S_{(\bar{\rho}u)} \frac{(\rho u)''}{\bar{\rho}u} \pm S_{(\phi)} \bar{\rho} \frac{(v'')}{\bar{\rho}u} + S_{(\bar{T}_t)} (T_t'') \quad (34)$$

where $S_{(\quad)}$ represents the wire sensitivity to mass flux $(\bar{\rho}u)$, wire orientation angle (ϕ) , and total temperature (\bar{T}_t) and the double prime refers to a time varying quantity. The plus or minus sign ahead of the second term is determined by the sign convention chosen for the vertical velocity. Morkovin showed that equation (34) was restricted to wire operation such that $M_\infty \sin \phi$ was greater than 1.2, a range where the sensitivity of wires to density and velocity changes were equivalent and could be combined into a single sensitivity $S_{(\bar{\rho}u)}$.

More recently, a study⁽³¹⁾ similar to Morkovin's but including more wire calibration data, showed that equation (34) is also valid at lower Mach

numbers provided the wire overheat, $[\tau_{wr} = (T_w - T_r)/T_r]$, and wire Reynolds number, Re_r , were above 0.5 and 50, respectively. The conclusions of the study were based on calculations of the sensitivities obtained from the correlations of wire data by Berhens⁽³²⁾ and corroborated by comparisons with sensitivity data from normal wires obtained by Rose and McDaid.⁽³³⁾ Examples of the results, given in figures 8 and 9, substantiate the conclusion that equation (34) is also valid at lower Mach numbers provided the restrictions mentioned above are met.

Modal analysis techniques similar to those proposed by Morkovin⁽³⁰⁾ for a normal wire can be used to solve equation (34) for the fluctuating quantities because the sensitivities are known functions of wire temperature that are obtained by suitable calibrations. Squaring equation (34) and time averaging yields a set of equations with six unknowns, the three fluctuating time-averaged variables and their cross products. Conceptually, a solution is possible if the wire is operated at a minimum of six overheats. However, to obtain accurate values of the six unknowns extremely accurate values of the sensitivity coefficients and fluctuating voltages must be obtained. To increase the accuracy of the process a normal wire can be used to obtain $(\rho u)''$ and T_t'' and their correlation independently and the yawed wire results only used to obtain the remaining unknowns. Rose used this technique to sort out the fluctuating quantities and their correlations in a turbulent supersonic boundary layer in the presence of an adverse pressure gradient.⁽³⁴⁾ In Rose's case, this process was made easier since the terms involving T_t'' and its correlation with v'' were of smaller order than the remaining terms. An alternate technique can be employed that does not depend on wire operation at a large number of overheats. For obtaining information on the fluctuating

mass flow and vertical velocity and their correlation, the wires may be operated at high enough temperatures so that they are sensitive mainly to mass-flow fluctuations, $S_{(\rho u)} \gg S_{(T_t)}$. Conversely, they may be operated at low temperatures where they are sensitive mainly to temperature fluctuations, $S_{(T_t)} \gg S_{(\rho u)}$. (The latter application is difficult to achieve in practice with "backed wires" operated at constant temperature so they are usually operated at constant current.)

Consideration must now be given to how shear stresses might be obtained with hot wires. Provided $S_{(\rho u)} \gg S_{(T_t)}$, adding and subtracting the signals from a dual-backed wire and time averaging will provide data on the root-mean square values, $\langle(\rho u)''\rangle$ and $\langle(v)''\rangle$, and the correlation $R_{(\rho u)''v''}$. The measurements then can be used to give

$$\overline{(\rho u)''v''} = R_{(\rho u)''v''} [\langle(\rho u)''\rangle] [\langle(v)''\rangle] \quad (35)$$

Usually an independent measurement of $\langle(\rho u)''\rangle$ is obtained by operating a single normal backed wire in the same flow.

Expanding the left-hand side of equation (35),

$$\overline{(\rho u)''v''} = \overline{\rho u''v''} + \bar{u} \overline{\rho''v''} \quad (36)$$

Introducing the polytropic gas law and neglecting higher-order correlations such as $\overline{\rho''T''}/\bar{\rho}\bar{T}$ compared to $\bar{\rho}''/\bar{\rho}$ and \bar{T}''/\bar{T} , the following equation may be written

$$\frac{\overline{p''v''}}{\bar{p}} = n \frac{\overline{\rho''v''}}{\bar{\rho}} = \frac{n}{n-1} \frac{\overline{T''v''}}{\bar{T}} \quad (37)$$

Equation (37) can be written in terms of total temperature by introducing the perfect gas energy equation.

$$n \frac{\overline{\rho''v''}}{\bar{\rho}} = \frac{n}{n-1} \frac{1}{\bar{T}} \left(\overline{T_t''v''} - \frac{\bar{u}}{c_p} \overline{u''v''} \right) \quad (38)$$

Substituting equation (38) into equation (36) results in

$$\overline{\rho u'' v''} = \left\{ \frac{c_p \bar{T}}{c_p \bar{T} - [u^2 / (n - 1)]} \right\} \left[\overline{(\rho u)'' v''} - \frac{\bar{u}}{n - 1} \frac{\bar{\rho}}{\bar{T}} \overline{T_t'' v''} \right] \quad (39)$$

Recalling that the shear stress of interest in the governing equations in section II was written in mass-averaged variables, the additional relationship is required:

$$\overline{\rho u' v'} = \overline{\rho u'' v''} - \frac{\overline{\rho'' u''} \overline{\rho'' v''}}{\bar{\rho}} \quad (40)$$

In many instances the second term on the right-hand side of equation (40) can be assumed negligible compared to the first term. Equations (39) and (40) show how shear stresses can be obtained from hot-wire measurements of $\overline{(\rho u)'' v''}$ and $\overline{T_t'' v''}$. The latter correlation may be obtained by operating a normal wire at low overheat such that $S_{(\bar{T}_t)} \gg S_{(\bar{\rho} u)}$ with a constant current system along with a yawed probe operated at high overheat where $S_{(\bar{\rho} u)} \gg S_{(\bar{T}_t)}$. The triple probe⁽²⁸⁾ mentioned previously was operated in this manner. Additional manipulation of equation (39) to eliminate the temperature-velocity correlation in favor of the introduction of a turbulent Prandtl number can also be accomplished. Following the derivation in reference 35 the following is obtained.

$$\overline{\rho u'' v''} = \left\{ 1 + \frac{1}{n - 1} \frac{\gamma - 1}{Pr_t} M^2 \left[1 - c_p \frac{d\bar{T}/dy}{\bar{u}(d\bar{u}/dy)} \right] \right\}^{-1} \overline{(\rho u)'' v''} \quad (41)$$

Expression (41) has been employed for both adiabatic and nonadiabatic wall temperature flows under the assumption of isobaric turbulence ($n = 0$) and for $Pr_t = 0.9$. Use of this expression does not require a measurement of temperature-velocity correlations. In reference 35, a comparison of $\overline{\rho u'' v''}$ with similar data using measured temperature velocity correlations showed excellent agreement. In all applications of hot-wire measurements to obtain

shear stress the polytropic exponent n must be assumed. Fortunately, Kistler's measurements of adiabatic boundary layers to Mach number 5 showed that the isobaric relationship for turbulent eddies is adequate and so $n = 0$ is appropriate. No information on the exponent, n , is available above this Mach number, however.

In principle, the laser velocimeter does not depend on the assumptions relating density and velocity fluctuations to temperature and velocity fluctuations. By intersecting two coherent light beams in a small volume within a flow field a precisely known interference fringe pattern is established in a plane perpendicular to their bisection. Any particle passing across the pattern alternately emits light that can be picked up with a photo sensor. Given the known distance between fringes and the time duration of the light pulse, the velocity of the particle may be measured. Provided the particle dynamics within the flow field are understood, a flow velocity may be obtained directly with this instrument. The technique also has the advantage of being nonintrusive. The problems of measurement interpretation should not be overlooked, however. Particle seeding techniques and measurement biasing toward higher velocities are but two of many problems encountered in the application of this instrument. It is not within the scope of this paper to discuss these problems so it suffices to mention that problems do exist and that they are being studied. However, recent applications where alternate means of measurement are available suggest these problems are not significantly influencing the results in many applications. See for example, reference 36 where favorable comparisons between hot-wire measurements and laser velocimeter measurements are shown.

Turbulent shear stress may be obtained in a manner analogous to that for slanted hot wires.⁽³⁷⁾ The optical axis of the velocimeter is rotated so that the fringes of one pair of crossing beams are oriented at a +45° angle to the flow direction. The velocimeter will measure a velocity (assume $v = 0$)

$$v_1 = [(u + u'') - v''] \frac{1}{\sqrt{2}} \quad (41a)$$

Rotating the axis to -45°, the velocity measured is

$$v_2 = (u + u'' + v'') \frac{1}{\sqrt{2}} \quad (41b)$$

The mean values of v_1 and v_2 are

$$\bar{v}_1 = \frac{\sum_{i=1}^N v_{1i}}{N} \quad \text{and} \quad \bar{v}_2 = \frac{\sum_{j=1}^M v_{2j}}{M} \quad (42)$$

Where N and M are the total number of discrete velocity measurements. The variances become

$$\sigma_1^2 = \frac{\sum_{i=1}^N (v_{1i} - \bar{v}_1)^2}{N - 1} \quad \text{and} \quad \sigma_2^2 = \frac{\sum_{j=1}^M (v_{2j} - \bar{v}_2)^2}{M - 1} \quad (43)$$

Squaring and taking the difference of equations (41), multiplying by $\bar{\rho}$ results in

$$\bar{\rho} \overline{u''v''} = \frac{\bar{\rho}}{2} (\sigma_2^2 - \sigma_1^2) \quad (44)$$

Recall that

$$\overline{\rho u''v''} = \bar{\rho} \overline{u''v''} + \overline{\rho'' u''v''}$$

and therefore shear measurements with the laser velocimeter neglects the triple correlation. The shear stress in the mass-averaged variables must be obtained from equation (40).

Figure 10 shows the results from several experiments where shear stress measurements were made across turbulent boundary layers without pressure gradients. The boundary-layer-edge Mach number in these experiments ranged from subsonic through hypersonic. The solid line indicates the expected variation of the normalized total shear stress that was shown in figure 5 and which is independent of edge Mach number. The measurements, obtained with hot-wire and hot-film anemometers and a laser velocimeter, show the variation of the turbulent component of shear stress. Except for the decreases near the wall ($y/\delta < 0.3$), due mainly to the relatively large probe size and not the difference between the total and turbulent magnitudes of shear nor the neglect of triple correlations, the data agree reasonably well with the expected trends in shear distribution. Work is in progress to resolve the differences near the wall and some success had been achieved. For example, use of a split-film anemometer minimizes the probe scale effects and suppresses the decrease to a location much nearer the wall.⁽³⁸⁾ From such data, mixing lengths or eddy viscosities in the outer regions of a turbulent boundary layer can be determined for use in first-order modeling concepts.

3. Fluctuating Flow-Field Measurements

Higher order modeling experiments require measurements of the individual fluctuating flow variables such as $\langle u'' \rangle$, $\langle v'' \rangle$, $\langle w'' \rangle$, and $\langle T'' \rangle$ and perhaps their spatial derivatives. As discussed in the previous section, velocity components may be measured directly by the laser velocimeter and under certain restrictions by the hot-wire anemometer. The restrictions on the latter device involve the choice of polytropic coefficient, n , to obtain streamwise velocity fluctuations $\langle u'' \rangle$ and not on $\langle v'' \rangle$ or $\langle w'' \rangle$, which may be obtained directly from a backed wedge probe if $S(\bar{p}\bar{u}) \gg S(T_t)$.

Choice of the isobaric value, $n = 0$, involved in most instances to obtain $\langle u'' \rangle$, is substantiated at $M = 3$,⁽³⁶⁾ and can be inferred from Kistler's measurements to $M \approx 5$. Temperature fluctuations may be obtained with the hot-wire anemometer. An example of fluctuating flow data obtained in a high subsonic boundary layer is shown in figure 11. (These data were obtained with hot-wire and backed hot-wire anemometers.) The solid lines are the usual ratios of 4:3:2 for $\langle u' \rangle^2 : \langle w' \rangle^2 : \langle v' \rangle^2$ in incompressible flows. The measurements of the individual velocity components agree with the incompressible data. Density fluctuations at these relatively low Mach numbers are small compared to the velocity fluctuations. Other examples of measurements of individual fluctuating flow quantities at supersonic and hypersonic speeds were reviewed in reference 27. It does appear that reasonably accurate measurements of the fluctuating flow variables in compressible flows can be achieved.

C. Experiments Supporting Turbulence Modeling Development in Two-Dimensional Flows

In order to illustrate how the experimental foundation for turbulence modeling might be established, it is helpful to focus on a particular problem. Consider the example of transonic flow about an airfoil as sketched on the top of figure 12. Three characteristic regions are identified that have certain distinct features as listed in the left-hand column. Actually, such features are typical of those found in a variety of aeronautical applications, so turbulence models developed to solve this particular problem will obviously apply to more general cases. Building-block experiments first selected to evaluate and guide the model development for each of the regions are sketched in the

next column. The numbers in parentheses below these sketches refer to the references which contain the experimental data.

An attempt was made to select these experiments on the basis of the requirements listed previously. However, in order to establish as wide a data base as possible, not all the experiments clearly meet the complete requirements. As will be discussed in the next section, model development has proceeded to the point where unresolved issues regarding the details of the available experimental data have surfaced and the need for additional experiments to resolve these issues is clear. These issues and sketches of additional experiments complete the information in figure 12.

For the case of fully turbulent attached flows over airfoils where the boundary-layer approximation to the full Navier-Stokes equations applies, pressure gradient and wall curvature encompass the important flow features. Obviously, if the Mach number was increased heat transfer would also be important. The first experiments chosen will mainly test the ability of the model to predict the effects of adverse pressure gradient. One of the experiments also includes a favorable gradient.⁽⁴¹⁾

In the second region, separation and reattachment may occur and the list of flow features is longer and obviously the problems are more complex. For example, the inviscid-viscid interaction affects the whole flow field and the complete Navier-Stokes equations may be required to solve the problems. The flows chosen for model development all have rather severe interaction and test the ability of the model to predict separation extent and reattachment characteristics. The trailing-edge flow region has fewer experiments that provide either verification or guidance for modeling. Those first chosen test the

ability of the model to predict separation in the presence of adverse pressure gradients and how a model used in attached flows might be extended with wake or trailing-edge flows.

The additional experiments sketched in the last column might be proposed so as to obtain answers to the unresolved issues arising from a study of modeling for the building-block experiments as discussed in the next section.

IV. STATUS OF TURBULENCE MODELING FOR COMPRESSIBLE FLOWS

An experimental foundation for guiding and verifying turbulence model development was proposed in the previous section. The status of the various modeling concepts will now be reviewed by comparing computations that employ the models with the experimental data for the attached and separated flow cases.

A. Attached Flows

1. Boundary-Layer Flows with Zero or Mild Pressure Gradients

Algebraic eddy viscosity or mixing length closure models have been successfully applied to compute compressible, zero-pressure, and mild-pressure gradient boundary-layer flows. See, for example, chapter 9 of reference 9 where a large number of computations employing the baseline model described in section II is compared with experiment. For purposes of this review three additional examples are given to illustrate the success of the model and to point out where additional work may be necessary.

A comparison of the experimental data of Allen⁽⁵³⁾ on an axisymmetric ogive-cylinder body and a computation employing the baseline model is shown in figure 13. The computations were made with a boundary-layer program originally developed for laminar flow⁽⁵⁴⁾ but modified several years ago by Marvin and

Sheaffer so that turbulent flows could also be computed. Comparisons of the computations with the skin friction and velocity-profile data, obtained by three techniques, indicate the kind of agreement that can be expected when employing the baseline model at low Mach numbers on bodies at adiabatic wall temperatures. Calculations with and without transverse curvature (TVC) to account for a thick boundary layer show little difference.

At higher Mach numbers, modeling changes that account for heat transfer and density fluctuations must be considered. For Mach numbers up to 10, modifications to the baseline model apparently are sufficient to account for these effects. Shang⁽⁵⁵⁾ made this conclusion on the basis of comparisons with skin friction and heat transfer data. He accounted for the triple correlation, $\overline{\rho'u''v''}$, neglected in the baseline model in an approximate way by multiplying equations (19) and (20) by the term $[1 + (\langle \rho' \rangle / \rho)]$. The magnitude of the density ratio was obtained by solving the y-momentum equation for the turbulent fluctuating pressure and introducing its magnitude into the equation of state, along with a correlation for temperature fluctuations. Also he, as well as others before him, found that the effects of heat transfer could be adequately accounted for by the introduction of a turbulent Prandtl number, equation (24), which could be expressed as a constant, $Pr_t = 0.9$, or a variable value depending upon the location in the boundary layer. However, the solutions were not too sensitive to the choice of the Prandtl number and the value of 0.9 was recommended. Above a Mach number of 10, the adequacy of the baseline model or its modified form has not been established. Lack of sufficiently accurate data above $M = 10$ contributes substantially to this conclusion.

Figures 14 and 15, taken from reference 55, illustrate the success of employing a modified baseline model to predict skin friction and heat transfer

at hypersonic Mach numbers. At Mach 7.4, including the effects of the density fluctuations has a small influence and the unmodified baseline model predicts the data quite well. At Mach number 10.5, the effects of density fluctuations are larger and the modified model apparently yields a better prediction of the skin friction data. In both these examples the turbulent Prandtl number was held constant at 0.9 and the predictions of heat transfer are conservative. Introducing a variable Prandtl number would result in somewhat better agreement but apparently there is further need for study to resolve the question of adequately predicting the heat transfer. Also in these examples, the initial rise in skin friction subsequent to transition is not predicted very well, but this result can be attributed to the influence of low Reynolds number on the Clauser modeling constant, 0.0168. (See, e.g., chapter 6 of ref. 9.)

Uniformly distributed mass transfer at the wall is another problem of interest receiving greater attention now because of the possibility of its use to reduce drag on aerodynamic surfaces and thereby decrease aircraft fuel consumption. Modification to the baseline model to account for mass transfer at the wall is accomplished by altering the value of A^+ in equation (22). An appropriate variation of A^+ with mass transfer is found through analysis of experimental data. This is illustrated in figure 16 where experimentally determined values of A^+ are correlated with a mass transfer parameter B/c_f , where $B = \rho_w v_w / \rho_e u_e$ and c_f is the local value of skin friction. The data are adequately represented by an exponential curve.

Predictions of the skin friction and heat transfer employing this modification to A^+ have been made with the Marvin-Sheaffer⁽⁵⁴⁾ boundary-layer program. Results are shown in figure 17 where the skin friction and heat transfer normalized by their untranspired values are plotted versus a

dimensionless mass transfer parameter. The skin friction decrease with increasing mass addition is predicted reasonably well. The effects of compressibility, or Mach number, are small both theoretically and experimentally. Recently, similar results for skin friction to $M_\infty = 6.6$ were presented.⁽⁶⁶⁾ The heat transfer decrease is also predicted well to $M = 0.7$. However, not shown are results at higher Mach number where the available data indicate a far smaller decrease in heat transfer than is predicted. This latter aspect is discussed in reference 63 and still requires further theoretical and experimental study.

2. Boundary-Layer Flows with Severe Pressure Gradients

The status of turbulence modeling for compressible boundary layers encountering rather severe pressure gradients will be discussed by considering the attached flow experiments introduced in figure 12. These experiments and their test conditions are summarized in figure 18 taken from reference 20.

Attempts to predict the experimental data by using the baseline algebraic turbulence model introduced previously gave results that were not entirely satisfactory.⁽¹²⁾ However, in some instances a reasonable prediction was achieved as will be shown subsequently. The poorest prediction was obtained for the compression ramp data of Sturek and Danberg⁽⁴³⁾ as illustrated in figure 19, taken from reference 12, and serves as an example to show how modifications to the model were employed to improve the situation. In this instance the baseline model predicts no rise in skin friction in contradiction to the data. Modifying the baseline model coefficients A^+ or A^+ and k (see eqs. (19) and (22)) as suggested for incompressible flows with pressure gradient^(9,64,65) did not improve the prediction for all of the flows and in some cases produced poorer results.

The curve labeled $\lambda = 0$, where $\lambda = 1/\delta$, in figure 19 shows such a result when A^+ and k are modified to account for pressure gradient. However, Horstman was able to improve the predictions with the baseline model by introducing an additional empirical relaxation parameter (λ) in the modification for A^+ and k . For example, the curve labeled $\lambda = 7.5$ shows excellent agreement with the data. Results similar to this were obtained for each of the experiments in figure 18. However, the disadvantage of such an approach was that each experiment required a different relaxation scale to effect a good prediction and the available data were not sufficient to determine a universal correlation of relaxation scale length in terms of pressure gradient that would encompass the important parameters of Mach number and Reynolds number.

In contrast to the former results, a recent study has shown that the two-equation model of Wilcox⁽¹⁷⁾ and the full Reynolds stress model of Donaldson⁽¹⁹⁾ introduced in section II provide overall a better means of predicting these adverse pressure gradient flows.⁽²⁰⁾ Furthermore, no adjustments to modeling constants were required.

To illustrate this finding, examples of the results taken from reference 20 are shown in figures 20, 21, and 22 for the adverse pressure gradient flow of Peake et al.⁽⁴⁰⁾ In figure 20, the mean flow pressure and velocity are shown along with the skin friction and form factor, H . The baseline model prediction is labeled Marvin-Shaëffer and the Wilcox and Donaldson models are labeled Wilcox-Traci and ARAP, respectively. The rise in skin friction is predicted very well by the two-equation and Reynolds stress models.

Typical of the baseline model, the predicted increase lags the data because no additional production of turbulence other than that introduced

through changes in the mean flow is accounted for. The axial distribution of the shape factor is reproduced reasonably well by all the models, but the baseline model predicts a consistently higher magnitude. The velocity and shear stress profiles for two axial locations, one after a run of adverse pressure gradient and a second far downstream in the constant pressure region, are shown compared with the predictions in figures 21 and 22. The velocity profiles are predicted very well by the Wilcox and Donaldson models. The shear stress profiles are predicted (overall) better by the multiequation models.

The advantage of the models employing additional differential equations to describe the behavior of the turbulence results from the expectation that they are capable of predicting a wide variety of flows without modification of constants and that they might provide the best means for calculating through separated regions such as those discussed in the next section.

B. Separated Flows

In the example proposed in figure 12 at the end of section III, separation and reattachment in the region of a shock wave interaction with a boundary layer were characteristic of the flow features that would have to be predicted by a successful turbulence model. Work directed toward model development for this problem has been under way for several years, both experimentally and computationally, and the progress on both aspects will be reviewed now.

1. The Building-Block Experiments

The building-block experiments now being used by the group at Ames Research Center to study the behavior of turbulent boundary layers undergoing separation and reattachment after their interaction with an incident shock

wave are described. Each experiment, in which there is a significant coupling of the viscous and inviscid flow fields, has a companion computer simulation that uses the complete time-averaged, Navier-Stokes equations and requires a large, fast computer for a solution. The experiments, in various degrees of completeness at this time, cover a wide range of Mach numbers and Reynolds numbers.

The first two experiments involve transonic flows and particular interest is directed toward shock-boundary-layer interactions on wings. Figure 23(a) shows the experimental arrangement for a verification experiment⁽⁴⁵⁾ being performed on a wing that spans the test section of a high Reynolds number channel recently built at Ames Research Center. The facility operates in a blow-down mode, and the free-stream Mach number can be adjusted before or during tests by a translating wedge that acts as a downstream choke. The upper and lower walls are contoured so that strong shocks would not extend to the walls and choke the flow. A thick circular-arc wing (fig. 23(b)) was chosen to allow local airfoil Mach numbers to achieve values where shock-induced separation would occur, but without having the shock extend more than about two-thirds of the distance between the wing and the outer wall. Surface pressures for various Mach numbers and Reynolds numbers have been obtained as well as surface skin friction at specific Reynolds numbers.^(45,66) Still to be obtained are mean velocity data and more skin-friction data.

The wing experiment resulted in both shock-induced and trailing-edge-induced separation, depending on the free-stream Mach number. Data were obtained to Reynolds numbers, based on chord length, of 17×10^6 . At intermediate Mach numbers, some unsteadiness in the flow field occurred. The results are discussed in detail in reference 45. Reynolds-number effects for both the

trailing edge and shock-induced separation were not significant for wing-chord-based Reynolds numbers beyond 10×10^6 .

Some results obtained when shock-induced separation occurred are given in figure 24. Oil-flow patterns (lower portion of the figure) illustrate the two-dimensionality of the flow and the detail in the region downstream of separation. The shadowgraph view near the interaction clearly illustrates shock-induced separation. The pressure ratios downstream of the shock are below C_p^* , indicating that the flow is slightly supersonic and suggesting the presence of an oblique shock (also apparent in the shadowgraph).

Figure 25 presents the airfoil pressures at several Reynolds numbers and the skin-friction measurements at a single Reynolds number. The skin-friction measurements were obtained recently with surface-mounted wire gages specifically developed for this experiment.^(26,66) The location of separation, determined from the oil-flow photograph, is shown on the abscissa of the skin-friction plot. This location also corresponds to the location of the knee in the pressure curve downstream of the shock. The comparison with the computations is discussed subsequently.

Figure 26 shows the physical arrangement of another transonic flow experiment being used for code verification and model concept development.⁽²⁹⁾ These tests are also being conducted in the Ames High Reynolds Number Channel. Supersonic flow was developed at the entrance of an axisymmetric test section and a normal shock wave was positioned at a fixed location by adjusting the location of a downstream shock generator. The relative distance between the shock wave and the downstream shock generator was always about 1 m. Experimental verification data were obtained for Reynolds numbers, based on distance along the wall to the location of the shock wave, between 9×10^6 and 290×10^6 .

Over this range of Reynolds number, Mach number varied between 1.35 and 1.45 because of the differences in wall boundary-layer growth. With this arrangement, data are also being obtained at constant shock Mach number by allowing the shock position to vary along the tube surface when the Reynolds number is varied. A complete flow documentation, including turbulence measurements, has been performed at a Reynolds number of 37×10^6 where the corresponding Mach number ahead of the shock wave was 1.44.

Examples of the data are presented in figures 27 and 28. Additional results, including velocity profiles and velocity fluctuation data, are given in reference 29. The shock position is located at $x/\delta_u = 0$. The pressure rises rapidly downstream of the shock wave, causes separation, and then increases gradually. The corresponding skin friction is reduced ahead, reverses sign in the separated region, and then increases thereafter.

The shear stress data (fig. 28) were obtained with the backed cross-wire anemometer described previously. The maximum shear stress in the boundary layer shows a significant increase after the shock wave and then decreases downstream toward the value expected for a mild adverse pressure gradient. Downstream of the shock wave beyond the effective boundary layer, some measurable shear was evident. It reverses sign because the mean velocity profiles are retarded, probably resulting from a coalescence of compression waves ahead of the shock wave. (29) In this flow, the height of the separated zone was very small and no details were measured in the reversed-flow region.

Documentation of the mean flow over a wide range of Reynolds numbers is now under way. These data will be used to assess the ability of the turbulence model to predict Reynolds-number effects on such factors as interaction

lengths, pressure rise to separation, and the effects of Mach number on incipient separation.

One experiment being used to verify the computations in the supersonic regime is the adiabatic shock-impinging flow originally reported by Reda and Murphy.⁽⁴⁹⁾ Figure 29 is a schematic of the test arrangement. Shock waves of varying strength were impinged on a Mach 3 boundary layer developed along a tunnel wall. For some tests, the shocks were strong enough to separate the flow on the tunnel wall. Mean-flow profiles and surface-pressure data were reported originally. Since the original work was completed, skin-friction data have been inferred from the profile data⁽⁶⁷⁾ and shear distribution upstream and downstream of an interaction without separation were measured.⁽³⁶⁾ Currently, measurements throughout a separated region, such as velocity fluctuations, shear distributions, and surface skin friction, are being documented.

The surface pressure, normalized by the upstream total pressure, and indirectly inferred wall shear stress for a separated flow case are shown in figure 30. Separation and reattachment points from oil-flow photographs are indicated. The pressure data have a plateau near the separation. Data for various shock strengths⁽⁴²⁾ will be used to assess the ability of the Navier-Stokes codes to predict the onset of separation.

At hypersonic speeds, the axisymmetric shock expansion boundary-layer interaction flow described in reference 51 is being used to guide turbulence modeling concepts. The experiment is sketched in figure 31. The leading edge of the shock generator was varied between 5° and 20°. Measurements in the axial direction were made in finely spaced steps by traversing the shock generator in the axial direction during the tests. Complete flow documentation, including turbulence measurements across the flow field, is available

for shock generator angles of 7.5° , where unseparated interactions occurred, and at 15° , where fully separated interactions occurred. Surface pressure, skin friction, and heat transfer values are available for other generator angles⁽⁴²⁾ and will be used to verify the ability of the turbulence model to predict the effects of shock strength on separation at hypersonic speeds.

The surface pressure, skin friction, and heat transfer for separated flow are shown in figure 32. Separation and reattachment points obtained from interpreting pitot-pressure measurements on probes near the surface facing both upstream and downstream are shown. The pressure increases through the interaction region, reaches a plateau near separation, and then rises further after reattachment. The skin friction decreases, then rises downstream of reattachment; the heat transfer rises continually. The decay in pressure, skin friction, and heat transfer downstream of the interaction results from the expansion fan emanating from the corner of the generator.

Fluctuating turbulence properties, for use as guides in modeling changes, were measured across the boundary layer at four locations through the interaction.⁽³⁵⁾ An example of the measurements is shown in figure 33, where the shear stresses at the four measurement locations are plotted. It was not possible to obtain shear measurements in the reversed-flow region of the separation bubble at the second measurement station so the expected trend has been sketched. The measurements show many of the same features as for the transonic experiment shown previously. Through the interaction, the maximum level of shear stress near the separated region increases significantly. Downstream of reattachment, $(x - x_0)/\delta_0 > -1$, the shear profiles do not differ in shape from those usually found in zero or slightly favorable pressure gradients.

Turbulence memory apparently persists only for about five boundary-layer thicknesses beyond the initial rise in pressure.⁽³⁵⁾

The supersonic corner flow experiment⁽⁵²⁾ sketched in figure 34 is the last of the shock interaction experiments to be discussed. Mean flow measurements at two ramp angles, 20° and 24°, have been documented and turbulence measurements are planned for the forthcoming year for the 20° ramp angle. Data have been obtained for an extremely large range of Reynolds number, based on boundary-layer thickness: $5 \times 10^5 \leq Re_\delta \leq 7 \times 10^6$. Typical results showing surface pressure and skin-friction data for the 20° ramp angle taken from reference 52 are reproduced in figure 35. Features common to all the supersonic interactions are evident; a pressure plateau and a rapid decrease in skin friction followed by a rise after separation.

2. Companion Computations Using Various Turbulence Models

Each of the experimentally determined flow fields described above have been programmed for numerical simulation on a CDC-7600 computer. Each program uses the mass-averaged form of the time-dependent Navier-Stokes equations and solves them with the MacCormack time-marching explicit scheme with splitting⁽⁶⁸⁾ and employs the more time-efficient algorithms proposed by MacCormack.⁽⁶⁹⁾ The complete Navier-Stokes equations were used because the viscous and inviscid flows interact significantly and it was believed that use of approximate solution techniques would only introduce uncertainty when evaluating the ability of the turbulence models to predict measured trends with Mach number and Reynolds-number variations. Each of the programs and solution techniques has been reported on separately and their details will not be addressed here. Solutions for each of the flows described above have been

made employing the baseline and relaxation models discussed previously. Three of the flows have been predicted with the one-equation model and the others will be attempted in the near future. Eventually, it is likely that all the flows will require at least a two-equation model before reliable predictions can be expected. The results of the computations are discussed next.

The data from the transonic-wing experiment are compared in figure 24 with the computations performed by Deiwert.⁽⁷⁰⁾ With the baseline model, the overall features of the flow field are predicted reasonably well. For example, the trend of increasing airfoil peak Mach number with Reynolds number is predicted, as is separation due to shock interaction. Downstream of the shock, where the flow separates, the pressure recovery is overpredicted because the predicted shock wave is normal, whereas the experimental shock wave is oblique. A comparison of the predicted and measured skin friction at $Re = 10^7$ further illustrates the differences in that region as the location of predicted separation is downstream of that location determined from the oil-flow photographs. Use of the relaxation concept (eq. (25)) with one boundary-layer thickness for L (relaxation length) tends to shift the location of the shock wave closer to the leading edge and reduces the peak Mach number and resulting shock strength; nonetheless, the pressure recovery is still overpredicted.

Solutions using other choices for L did not improve the results. For Mach numbers at which the flow is not separated but at which viscous effects are still important, the computations using the baseline model compare very favorably with the data, except at the trailing edge where extensive separation occurred.⁽⁷⁰⁾ Because solutions to this problem take between 30 and 60 min of computation time, models employing differential equations for

turbulent kinetic energy or shear have not been attempted. These will be added in the near future, however, if other, more simple problems show improvement with employment of these models.

Comparisons of the computations with the data from the normal shock-wave experiment are presented in figures 27 and 28. The pressure predictions employing all the models agree well with the data. The skin friction is underestimated downstream, using either the baseline or relaxation models. However, the one-equation model of Rubesin does significantly better with regard to predicting the downstream skin friction and is considered a major improvement. The latter results were reported recently by Viegas and Coakley.⁽⁷¹⁾ The shear distributions obtained using the relaxation model are compared with the data in figure 28 at three locations downstream of the shock wave. Similar results were obtained with the baseline model. The computations fail to predict the significant increase in shear at the first station and, evidently, this continues to affect the prediction downstream. Better comparisons are expected with the one-equation model, but they were not available at the time this paper was written.

Comparisons for the oblique shock interaction using the baseline and relaxation turbulence models are shown in figure 30. For the oblique shock interaction, the baseline model predicts the overall pressure rise reasonably well and also predicts separation. However, no appreciable upstream influence in the pressure and no plateau are indicated in the calculations because the size of the separation bubble is underpredicted. Introducing the relaxation model with $L = 5$ boundary-layer thicknesses corrects this deficiency because it lowers the effective eddy viscosity near the separation, thus increasing the size of the separated zone, which in turn introduces a plateau

in the pressure-rise curve. The location of separation is predicted with the relaxation model, but the reattachment location is too far downstream.

The comparison with the wall shear downstream of reattachment where the boundary layer thins may appear better than is the actual case because these computations were made with a relatively coarse grid, and in the downstream locations the first computation point away from the wall was in the logarithmic region of the turbulent boundary layer. Since the method used to obtain derivatives at the wall requires calculated points within the sublayer region, the predicted shear is expected to be lower than the measurements, and the results would be similar to those for the transonic normal shock comparisons.

In figure 32, the predicted results and experimental data for the hypersonic shock interaction are compared. As with the supersonic oblique shock interaction, the baseline model prediction reproduces the overall trends in the data but is deficient in the separated region. Recent calculations by T. J. Coakley⁽⁷¹⁾ using the one-equation model of Rubesin improves the situation. The height of the separation was greater and the resulting upstream influence leads to a plateau in the pressure. However, Coakley had to alter the algebraic length scale in the model to affect the changes. The location where skin friction begins to decrease is predicted, but the extent of the separation in the axial direction is still overpredicted. The heat transfer is underpredicted throughout the interaction region with either model.

The supersonic corner flow has been predicted using the baseline, relaxation, and one-equation turbulence models. The latter computations were recently made by Horstman. The results are compared with the experimental data in figure 35. The baseline model predictions show no plateau in the pressure distribution as a result of the small predicted separation zone, and

the skin friction downstream of reattachment is underpredicted. The relaxation model does increase the size of the separation zone and a plateau in pressure is predicted, but the skin friction downstream of reattachment is still underpredicted. The one-equation model significantly improves the prediction of skin friction and does reasonably well in the prediction of the overall pressures. Moreover, a comparison recently made by Horstman of the velocity profiles downstream of reattachment with the computations shows a marked improvement when the one-equation model is used.

From an examination of all the comparisons, the following general observations can be made. In most cases, the pressure rise can be predicted reasonably well with a simple eddy viscosity description for the turbulence. The exception is for the transonic wing where the shock-induced separation was very large and extended from the foot of the shock beyond the trailing edge. The algebraic eddy viscosity concept is deficient in providing the proper details within the separated zone and this, in turn, apparently affects the entire flow field when the separation zones are large.

Introducing relaxation tends to improve the situation somewhat because it decreases the eddy viscosity in the region of separation, resulting in an increase in the height of the separation. However, the next decrease in eddy viscosity persists beyond the separated zone even for short relaxation lengths, and the codes underpredict the skin friction downstream. Interpretation of the modeling experiments indicated the need for an increase in effective eddy viscosity downstream of reattachment. An improved turbulence model that effectively accomplished this is the one-equation model of Rubesin. Further improvement to this model can be made by altering the algebraic length scale

as shown by Viégas and Coakley.⁽⁷¹⁾ In fact, their results suggest that a two-equation model will probably provide an even better prediction. Still needed, however, is a better model for the flow in the separated region where the flow is reversed; but the lack of data from such regions makes the guidance of model changes difficult.

V. CONCLUDING REMARKS

A complete concept of turbulence modeling has been described. The elements — experiments, modeling concepts, and computations — were each reviewed to provide an up-to-date status of the problem. Experiments were classified as verification or modeling types. Verification experiments were described as those that measured mean flow quantities and they would provide a means for assessing the ability to predict correctly over the flight ranges of Mach and Reynolds number. On the other hand, modeling experiments would require measurements of the turbulent flow itself in sufficient detail to guide and verify the turbulence models actually used in the computation codes.

Recent techniques used to measure turbulent properties in compressible flow were reviewed and the results are encouraging enough to permit the conclusion that modeling experiments can be performed at various Mach numbers. A set of experiments to evaluate and guide turbulence model development for two-dimensional flows was introduced and comparisons of computations employing various turbulence models were made. The results of the comparisons showed that algebraic eddy viscosity models were sufficient to predict most attached flows with zero or mild pressure gradients up to Mach number 10.

Models that employ additional differential equations to describe turbulent kinetic energy or shear stress are required in the case of severe

pressure gradients. Flows with separation on reattachment are also predicted better with models using additional differential equations, but the number of examples is limited at the present time and further comparison will have to be made before a predictive model is available for these flows.

REFERENCES

1. D. R. Chapman, H. Mark, and M. W. Pirtle, Computers vs. wind tunnels for aerodynamic flow simulation, Astronaut. & Aeronaut. 13(4), 22-30 (1975).
2. F. R. Bailey and W. F. Ballhaus, Comparisons of Computed and Experimental Pressures for Transonic Flows About Isolated Wings and Wing-Fuselage Configurations, NASA SP-347, vol. II (1975), pp. 1213-1232.
3. J. V. Rakich and E. G. Pegot, Flow Field and Heating on the Windward Side of the Space Shuttle Orbiter, NASA SP-347, vol. II (1975), pp. 1377-1394.
4. F. Marconi, L. Yaeger, and H. H. Hamilton, Computation of High-Speed Inviscid Flows About Real Configurations, NASA SP-347, vol. II (1975), pp. 1411-1456.
5. O. Reynolds, On the dynamical theory of incompressible viscous fluids and the determination of the criterion, Phil. Trans. A 186, 123-161, or Papers 2, 535 (1874).
6. S. J. Kline, M. V. Morkovin, G. Sovran, J. D. Cockrell, D. E. Coles, and E. A. Hirst (eds.), Proceedings, Computation of Turbulent Boundary Layers, 1968 AFOSR-IFP-Stanford Conference, vols. I and II (August 1968).

7. Anon: Compressible Turbulent Boundary Layers, NASA SP-216 (1968).
8. M. W. Rubesin and W. C. Rose, The Turbulent Mean-Flow Reynolds-Stress, and Heat Flux Equations in Mass-Averaged Dependent Variables, NASA TM X-62,248 (March 1973).
9. Cebec Tuncer and A. M. O. Smith, "Analysis of Turbulent Boundary Layers," Academic Press (1974).
10. J. S. Shang and W. L. Hankey, Jr., Numerical Solution of the Navier-Stokes Equations for Supersonic Turbulent Flow Over a Compression Corner, AIAA Paper 74-4 (1975).
11. B. S. Baldwin and W. C. Rose, Calculation of Shock-Separated Turbulent Boundary Layers, NASA SP-347, vol. I (1975), pp. 401-409.
12. C. C. Horstman, A Turbulence Model for Nonequilibrium Adverse Pressure Gradient Flows, AIAA Paper 76-412, AIAA 9th Fluid and Plasma Dynamics Conference, San Diego, California (July 14-16, 1976).
13. Morris W. Rubesin, A One-Equation Model of Turbulence for Use With the Compressible Navier-Stokes Equations, NASA TM X-73,128 (April, 1976).
14. G. S. Glushko, Turbulent boundary layer on a flat plate in an incompressible fluid, Bull. Acad. Sci. USSR, Mech. Ser. 4 (1965), pp. 13-23.

15. J. O. Hinze, "Turbulence, An Introduction to its Mechanism and Theory," McGraw-Hill, New York (1959).
16. J. C. Rotta, Statistische Theorie nichthomogener Turbulenz, Z. Phys. 129, 546 (1951).
17. D. C. Wilcox and R. M. Traci, A Complete Model of Turbulence, AIAA Paper 76-351. AIAA 9th Fluid and Plasma Dynamics Conference, San Diego, California (July 14-16, 1976).
18. V. K. Varma, R. A. Beddini, R. D. Sullivan, and C. duP. Donaldson, Application of Invariant Second-Order Closure Model to Compressible Turbulent Shear Layers, AIAA Paper 74-592 (June 1974).
19. Roger D. Sullivan, GYC: A Program to Compute the Turbulent Boundary Layer on a Rotating Cone, ARAP Working Paper No. 76-2, Aeronautical Research Associates of Princeton, Inc., 50 Washington Rd., Princeton, N. J. (August, 1976).
20. M. W. Rubesin, A. J. Crissalli, M. J. Lanfranco, C. C. Horstman, and M. Acharya, A Critique of Some Recent Second-Order Turbulence Closure Models for Compressible Boundary Layers. AIAA Paper 77-128, AIAA 15th Aerospace Sciences Meeting (January 24-26, 1977), Los Angeles, California.

21. Joseph G. Marvin, Experiments Planned Specifically for Developing Turbulence Models in Computations of Flow Fields Around Aerodynamic Shapes, Paper No. 1 presented at the AGARD Specialists Meeting on Numerical Methods and Wind-Tunnel Testing, Von Karman Institute Rhode-St-Genese, Belgium (23-24 June 1976).
22. J. Lloyd Jones, Jr., Problems of Flow Simulation in Wind Tunnels, AIAA Paper 69-660 (1969).
23. P. Bradshaw, The understanding and prediction of turbulent flow, The Aeronautical Journal 76(739) (July 1972).
24. D. E. Coles, A Young Person's Guide to the Data, Proceedings - Computation of Turbulent Boundary Layers - 1968, AFOSR-IFP-Stanford Conference, vol. II (1968), pp. 1-45.
25. P. J. Waltrup and J. A. Schetz, Supersonic turbulent boundary layer subjected to adverse pressure gradients, AIAA J. 11(1), 50-57 (Jan. 1973).
26. Morris W. Rubesin, Arthur F. Okuno, George G. Mateer, and Aviel Brosh, A Hot-Wire Surface Gage for Skin Friction and Separation Detection Measurements, NASA TM X-62,465 (July 1975).

- | | | | | | | | |
|--|--|--|--|--|--|--|--|
| | | | | | | | |
|--|--|--|--|--|--|--|--|
27. V. A. Sandborn, A Review of Turbulence Measurements in Compressible Flow, NASA TM X-62,337 (March 1974).
 28. V. Mikula and C. C. Horstman, Turbulence stress measurements in a non-adiabatic hypersonic boundary layer, AIAA J. 13(12), 1607-1613 (Dec. 1975).
 29. G. G. Mateer, A. Brosh, and J. R. Viegas, A Normal Shock-Wave Turbulent Boundary-Layer Interaction at Transonic Speeds, AIAA Paper 76-161 (1976).
 30. M. V. Morkovin, Fluctuations and Hot-Wire Anemometry in Compressible Fluids, AGARDograph No. 24 (November, 1956).
 31. C. C. Horstman and W. C. Rose, Hot-Wire Anemometry in Transonic Flow, NASA TM X-62,495 (December, 1975).
 32. W. Behrens, Total temperature thermocouple probe based on recovery temperature of circular cylinder, Int. J. Heat Mass Trans. 14 (1971), pp. 1621-1630.
 33. W. C. Rose and E. P. McDaid, Turbulence Measurement in Transonic Flow. In Proceedings for AIAA 9th Aerodynamic Testing Conference, Arlington, Texas (June 7-9, 1976).

34. W. C. Rose, The Behavior of a Compressible Turbulent Boundary Layer in a Shock-Wave Induced Adverse Pressure Gradient, Ph.D. Thesis, University of Washington (1972). (Available as NASA TN D-7092.)
35. V. Mikulla and C. C. Horstman, Turbulence Measurements in Hypersonic Shock-Wave Boundary-Layer Interaction Flows, AIAA Paper 76-162 (January, 1976).
36. W. C. Rose and D. A. Johnson, A study of shock-wave turbulent boundary layer interaction using laser velocimeter and hot-wire anemometer techniques. AIAA J. 13(7), 884-889 (July, 1975).
37. W. J. Yanta, Turbulence Measurements With a Laser Doppler Velocimeter, Ph.D. Thesis, The Catholic University of America, Washington, D.C. (1973).
38. V. A. Sandborn and H. L. Seegmiller, Evaluation of Mean and Turbulent Velocity Measurement in Subsonic Accelerated Boundary Layers, NASA TN D-8367 (1976).
39. F. J. Zwarts, The Compressible Turbulent Boundary Layer in a Pressure Gradient, Ph.D. Thesis, Dépt. of Mechanical Engineering, McGill University, Montreal, Canada (1970).

40. D. J. Peake, G. Brakmann, and J. M. Romeskié, Comparison Between Some High Reynolds Number Turbulent Boundary Layer Experiments at Mach 4, and Various Recent Calculation Procedures, in Turbulent Shear Flows, AGARD CP-93 (September, 1971).
41. J. E. Lewis, R. L. Gran, and T. Kubota, An experiment on the adiabatic compressible turbulent boundary layer in adverse and favourable pressure gradients, J. Fluid Mech. 51, Part 4 (February, 1972), pp. 657-672.
42. M. I. Kussoy and C. C. Horstman, An Experimental Documentation of a Hypersonic Shock-Wave Turbulent Boundary Layer Interaction Flow - With and Without Separation, NASA TM X-62,412 (February, 1975).
43. W. B. Sturek and J. E. Danberg, The Supersonic Turbulent Boundary Layer in an Adverse Pressure Gradient - Experiment and Data Analysis, Turbulent Shear Flows, AGARD CP-93 (September, 1971).
44. A. E. Samuel and P. N. Joubert, A boundary layer developing in an increasingly adverse pressure gradient. J. Fluid Mech. 66, Part 3 (1974), pp. 481-505.

45. John B. McDevitt, Lionel L. Levy, and George S. Deiwert, Transonic flow about a thick circular-arc airfoil, AIAA J. 14(5), 606-613 (May, 1976).
46. J. Seddon, The Flow Produced by Interaction of a Turbulent Boundary Layer With a Normal Shock Wave of Strength Sufficient to Cause Separation, ARC R & M 3502 (March, 1960).
47. J. W. Kooi, Experiment on Transonic Shock-Wave Boundary Layer Interaction. AGARD Conference on Flow Separation, AGARD-CPP-168, Paper No. 30 (1975).
48. L. F. East, The Application of a Laser Anemometer to the Investigation of Shock-Wave Boundary-Layer Interactions, Paper No. 5 presented at the AGARD Meeting on Applications of Non-Intrusive Instrumentation in Fluid Flow Research (May 3-5, 1976).
49. D. C. Reda and J. D. Murphy, Shock-Wave Turbulent Boundary-Layer Interactions in Rectangular Channels, Part II: The Influence of Sidewall Boundary Layers on Incipient Separation and Scale of the Interaction, AIAA Paper 73-234 (1973).

50. M. S. Holden, Shock Wave - Turbulent Boundary Layer Interaction in Hypersonic Flow, AIAA Paper 72-74, presented at AIAA 10th Aerospace Sciences Meeting, San Diego, California (January, 1972).
51. J. G. Marvin, C. C. Horstman, M. W. Rubesin, T. J. Coakley, and M. I. Kussoy, An Experimental and Numerical Investigation of Shock-Wave Induced Turbulent Boundary-Layer and Separation at Hypersonic Speeds, AGARD Conference Proceedings No. 168 on Flow Separation (May, 1975).
52. C. C. Horstman, G. S. Settles, I. E. Vas, S. M. Bogdonoff, and C. M. Hung, Reynolds Number Effects on Shock Wave-Turbulent Boundary-Layer Interactions - A Comparison of Numerical and Experimental Results. AIAA Paper 77-42, AIAA 15th Aerospace Sciences Meeting, Los Angeles, California (January 24-26, 1977).
53. J. M. Allen, Experimental Preston Tube and Law-of-the-Wall Study of Turbulent Skin Friction on Axisymmetric Bodies at Supersonic Speeds, NASA TN D-5660 (February, 1970).
54. J. G. Marvin and Y. S. Sheaffer, A Method for Solving the Nonsimilar Boundary-Layer Equations Including Foreign Gas Injection, NASA TN D-5516 (November, 1969).

55. J. S. Shang, A Parametric Study of Hypersonic Turbulent Boundary Layers With Heat Transfer, ARL TR 74-0003 (January, 1974).
56. R. L. Simpson, W. M. Kays, and R. J. Moffat, The Turbulent Boundary Layer on a Porous Plate: An Experimental Study of the Fluid Dynamics With Injection and Suction, Report No. HMT-2, Stanford University, Dept. of Mechanical Engineering (December, 1967).
57. Robert M. Kendall, Morris W. Rubesin, Thomas Dahm, and Michael R. Mendenhall, Mass, Momentum, and Heat Transfer Within a Turbulent Boundary Layer With Foreign Gas Mass Transfer at the Surface, Part I - Constant Fluid Properties, Report No. 111, Vidya, Division of Itek Corp. (February, 1964).
58. P. S. Andersen, W. M. Kays, and R. J. Moffat, The Turbulent Boundary Layer on a Porous Plate: An Experimental Study of the Fluid Mechanics for Adverse Free-Stream Pressure Gradients. Report No. HMT-15 (May, 1972).
59. R. J. Moffat and W. M. Kays, The Turbulent Boundary Layer on a Porous Plate: Experimental Heat Transfer With Uniform Blowing and Suction, Report No. HMT-1, Thermosciences Division, Dept. of Mechanical Engineering, Stanford University (1967).

60. H. Dershin, C. A. Leonard, and W. H. Gallaher, Direct measurement of skin friction on a porous flat plate with mass injection, AIAA J. 5, 1934-1039 (1967).
61. C. C. Pappas and A. F. Okuno, Measurement and Recovery Factor of a Compressible Turbulent Boundary Layer on a Sharp Cone With Foreign Gas Injection, NASA TN D-2230 (April, 1964).
62. D. M. Bushnell, R. D. Watson, and B. B. Holley, Mach and Reynolds Number Effects on Turbulent Skin Friction Reduction by Injection, J. Spacecraft & Rockets 12(8) (August, 1975).
63. P. Baronti, H. Fox, and D. Soll, A survey of the compressible turbulent boundary layer with mass transfer, Astronautica Acta 13, Pergamon Press Ltd., England (1967), pp. 239-249.
64. W. M. Kays, Heat Transfer to the Transpired Boundary Layer, ASME Paper No. 71-HT-44 (1971).
65. W. J. Glowacki and S. W. Chi, A Study of the Effect of Pressure Gradient on the Eddy Viscosity and Mixing Length for Incompressible Equilibrium Turbulent Boundary Layers, NOLTR 74-105, Naval Ordnance Laboratory, Silver Springs, Maryland (May, 1974).

66. M. W. Rubesin, A. F. Okuno, L. L. Lévy, Jr., J. B. McDévit, and H. L. Seegmiller, An Experimental and Computational Investigation of the Mean and Dynamic Flow Field About an Airfoil in Supercritical Flow With Turbulent Boundary-Layer Separation, Paper No. 76-15, The 10th Congress of the International Council of the Aeronautical Sciences, Ottawa, Ontario (October 4-8, 1976).
67. M. W. Rubesin, J. D. Murphy, and W. O. Rose, Wall shear in strongly retarded and separated compressible turbulent boundary layers, AIAA J. 12(10), 1442-1444 (October, 1975).
68. R. W. MacCormack and B. S. Baldwin, A Numerical Method for Solving the Navier-Stokes Equations with Application to Shock-Boundary Layer Interactions, AIAA Paper 75-1 (1975).
69. R. W. MacCormack, A Rapid Solver for Hyperbolic Systems of Equations. Paper presented at the 5th International Conference on Numerical Methods in Fluid Dynamics held at Twente University of Technology, Enschede, The Netherlands (June 28-July 2, 1976).
70. G. S. Deiwert, Computation of Separated Transonic Turbulent Flows, AIAA Paper 75-829 (June, 1975).

71. John R. Viegas and Thomas J. Coakley, Numerical Investigation of Turbulence Models for Shock Separated Boundary-Layer Flows, AIAA Paper 77-44, AIAA 15th Aerospace Sciences Meeting, Los Angeles, California (January 24-26, 1977).

TABLE I.- STATUS OF COMPUTATIONAL AERODYNAMICS

Stage of approximation for equations	Readiness time period			Limitations	Pacing item
	2D airfoils	3D wings	3D aircraft		
Inviscid linearized	1930's	1950's	1960's	Slender configurations Small angle of attack Perfect gas No transonic flow No hypersonic flow No flow separation	
Inviscid nonlinear	1971	1973	1976 ?	No flow separation	Code development
Viscous time averaged	1975	1977 ?	1979 ?	Accuracy of turbulence model	Turbulence modeling
Viscous time dependent			Mid 1980's	Accuracy of solution to Navier-Stokes eqs.	Développement of advanced computer

TABLE II.- ELEMENTS OF WELL-DOCUMENTED BUILDING-BLOCK EXPERIMENTS

Type of equation closure	Type of experiment	Documented quantities	Test conditions
First order or higher order	Verification	$C_F, C_H, p_w, \bar{T}, \bar{u}, \bar{v}, \bar{w}, \langle q_\infty \rangle$	To flight in Mach and Reynolds nos.
First order	First order modeling	$C_F, C_H, p_w, \bar{T}, \bar{u}, \bar{v}, \bar{w}, \langle q_\infty \rangle$ $\bar{\rho} \overline{v'u'}, \bar{\rho} \overline{T'v'}$	Representative flight Mach and Reynolds nos.
Higher order	Higher order modeling	$C_F, C_H, p_w, \bar{T}, \bar{u}, \bar{v}, \bar{w}, \langle q_\infty \rangle$ $\bar{\rho} \overline{v'u'}, \bar{\rho} \overline{T'v'}$ $\langle u' \rangle, \langle v' \rangle, \langle w' \rangle, \langle q \rangle, \overline{v'q'}, \frac{\partial u_1}{\partial x_j}$	Representative flight Mach and Reynolds nos.

FIGURE CAPTIONS

Figure 1.- Process of physical modeling for computer code development.

Figure 2.- Status of turbulence modeling.

Figure 3.- Mach and Reynolds number domain for aerospace vehicles.

Figure 4.- Mach and Reynolds number domain for experiments compared with that for aerospace vehicles.

Figure 5.- Comparison of estimated supersonic shear stress with incompressible measurements and the empirical prediction of Maise and McDonald. (Taken from ref. 27.)

Figure 6.- Probes developed for high-temperature applications. (Taken from ref. 28.)

Figure 7.- Supported crossed hot-wire probe. (Taken from ref. 29.)

Figure 8.- Comparison of calculated and measured velocity-density sensitivity ratios. (Taken from ref. 31.)

Figure 9.- Comparison of calculated density and velocity sensitivities and measured mass-flux sensitivity. (Taken from ref. 31.)

Figure 10.- Shear-stress measurements in compressible flows.

Figure 11.- Normalized rms velocity and density fluctuations across a compressible turbulent boundary layer.

Figure 12.- Model development for two-dimensional flows.

Figure 13.- Comparison of baseline turbulence model computation and data of Allen. (53)

(a) Skin friction.

(b) Velocity profile, $x = 2.08$ ft.

Figure 14.- Effect of density fluctuation of C_f and St at $M_c = 7.4$.

(Taken from ref. 55.)

Figure 15.- Effect of density fluctuation on C_f and St at $M_e = 10.5$.

(Taken from ref. 55.)

Figure 16.- Effects of mass transfer on baseline model constant, Λ^+ .

Figure 17.- Comparison between calculations using a modified baseline model and experiments for transpired boundary layers.

Figure 18.- Experimental test flows used as standards of comparison for the turbulence models. (Taken from ref. 20.)

Figure 19.- Comparison of measured and computed skin-friction distributions obtained using a turbulence lag model. (12)

Figure 20.- Streamwise distributions of boundary-layer characteristics, experiment of Peake, Brakmann, and Romeskie. (Taken from ref. 20.)

(a) Boundary-layer edge conditions.

(b) Local skin friction coefficient, based on free-stream dynamic pressure.

(c) Local form factor.

Figure 21.- Velocity and turbulent shear stress profiles after run of adverse pressure gradient, data of Peake et al.: $x = 52$ cm. (Taken from ref. 20.)

(a) Mean velocity profile.

(b) Turbulent shear stress profile.

Figure 22.- Mean velocity and turbulent shear stress profiles far downstream in Peake et al. experiment, $x = 67.3$ cm. (Taken from ref. 20.)

(a) Mean velocity profile.

(b) Turbulent shear stress profile.

Figure 23.- Experimental arrangement for a transonic wing undergoing shock-induced separation.

(a) Overall arrangement.

(b) Wing design.

Figure 24.- Shock-induced boundary-layer separation experiment on a biconvex circular-arc airfoil; $Re = 10.3 \times 10^6$, $M_\infty = 0.786$.

Figure 25.- Results from the shock-induced separation experiment on a biconvex circular-arc airfoil.

Figure 26.- Experimental arrangement for a normal shock-wave, turbulent boundary-layer experiment with separation.

Figure 27.- Results from normal shock-wave experiment; $M_\infty = 1.44$ and $Re_x = 37 \times 10^6$.

Figure 28.- Shear-stress profiles from the normal shock-wave experiment, $M_\infty = 1.44$ and $Re_x = 37 \times 10^6$.

Figure 29.- Experimental arrangement for a supersonic oblique shock-wave, boundary-layer interaction experiment; $M_\infty = 3.0$ and $Re_{\delta_0} = 9.73 \times 10^5$.

Figure 30.- Results from the supersonic oblique shock-wave, boundary-layer interaction experiment; $M_\infty = 3.0$ and $Re_{\delta_0} = 9.73 \times 10^5$.

Figure 31.- Experimental arrangement for an axially symmetric hypersonic oblique shock-expansion, boundary-layer interaction experiment; $M_\infty = 6.9$ and $Re_x = 13 \times 10^6$.

Figure 32.- Results from the hypersonic oblique shock-expansion, boundary-layer interaction experiment; $M_\infty = 6.9$ and $Re_x = 13 \times 10^6$.

Figure 33.- Shear-stress distributions for the hypersonic oblique shock-expansion, boundary-layer interaction experiment; $M_\infty = 6.9$ and $Re_x = 13 \times 10^6$.

Figure 34.- Sketch of 8- by 8-in. supersonic wind-tunnel and test model..

(Taken from ref. 52.)

Figure 35.- Results from the supersonic ramp flow experiment; $M_\infty = 3$, $\alpha = 20^\circ$,
and $Re_{\delta_0} = 1.65 \times 10^6$.

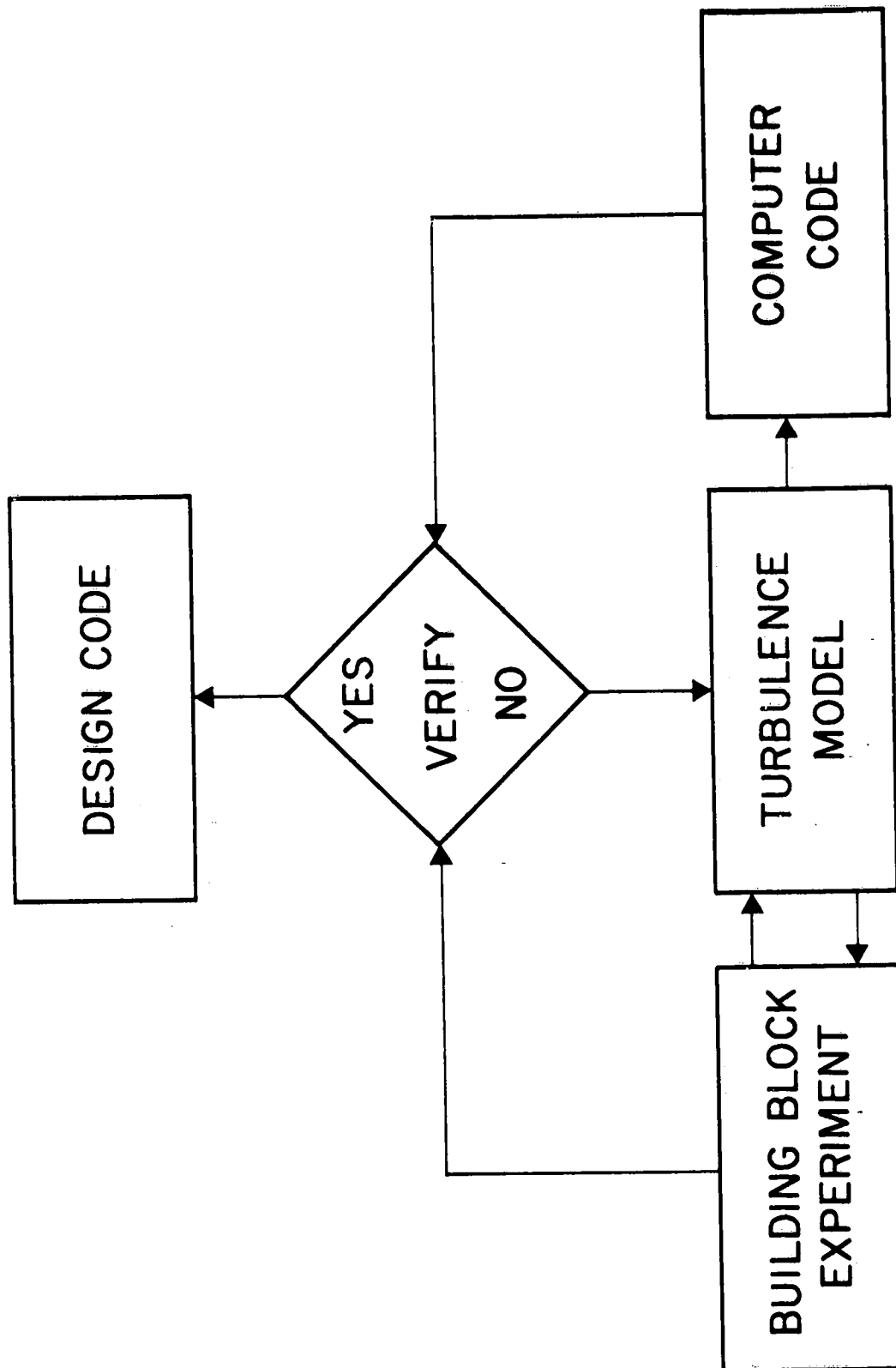


Figure 1.- Process of physical modeling for computer code development.

- CONSTANT PRESSURE FLOWS
 - MODELS IN HAND WITH FEW EXCEPTIONS
 - WIDE RANGE OF QUALITY DATA FOR VERIFICATION
- PRESSURE GRADIENT FLOWS - NO SEPARATION
 - MODELS IN HAND FOR MILD GRADIENTS
 - MORE COMPLEX MODELS UNDER DEVELOPMENT FOR SEVERE GRADIENTS
 - LIMITED RANGE OF QUALITY DATA FOR VERIFICATION FOR SEVERE GRADIENTS
- PRESSURE GRADIENT FLOWS - SEPARATION
 - MODELS NOT IN HAND
 - VERY LIMITED RANGE OF QUALITY DATA FOR VERIFICATION

Figure 2.- Status of turbulence modeling.

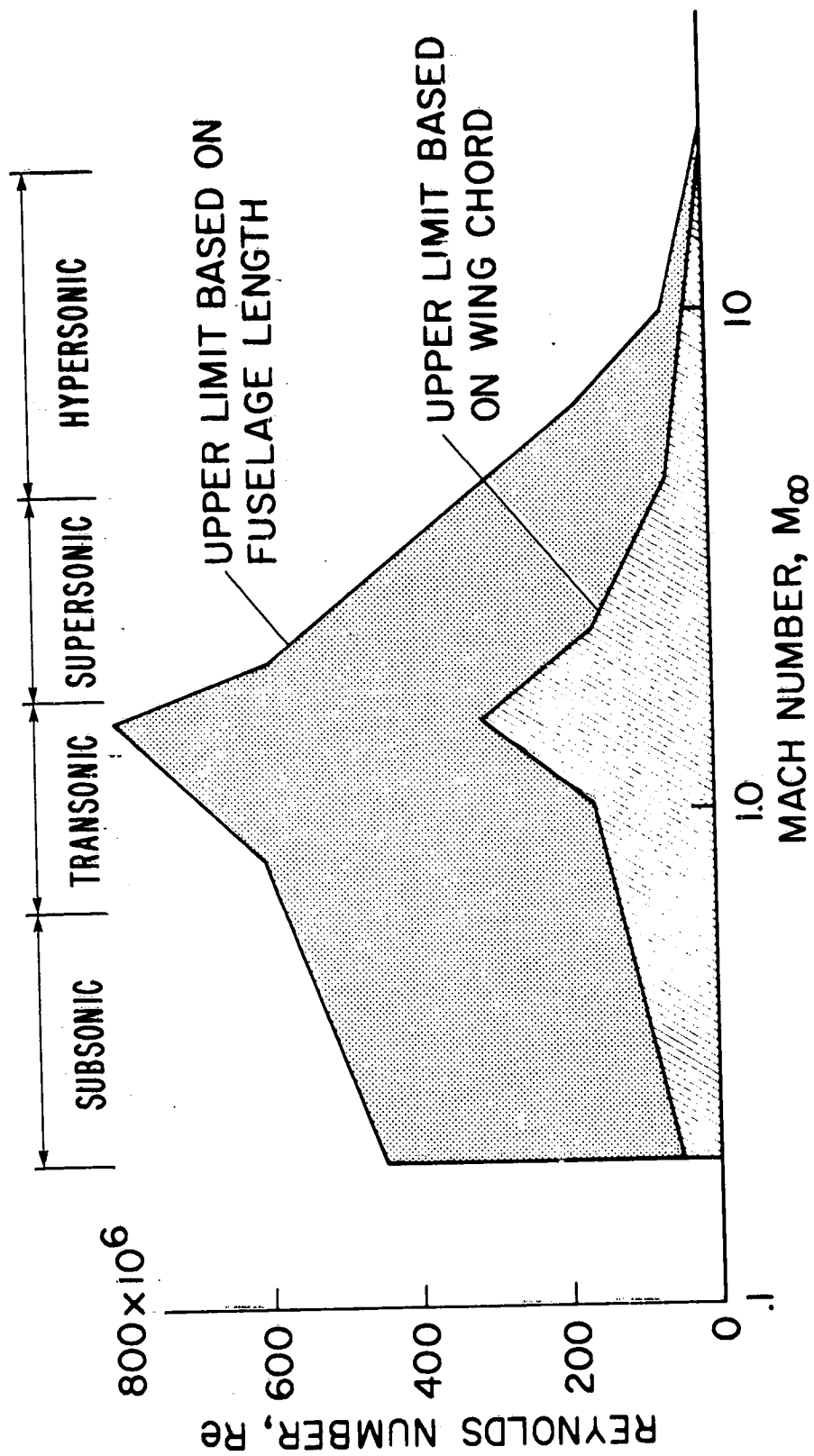


Figure 3.- Mach and Reynolds number domain for aerospace vehicles.

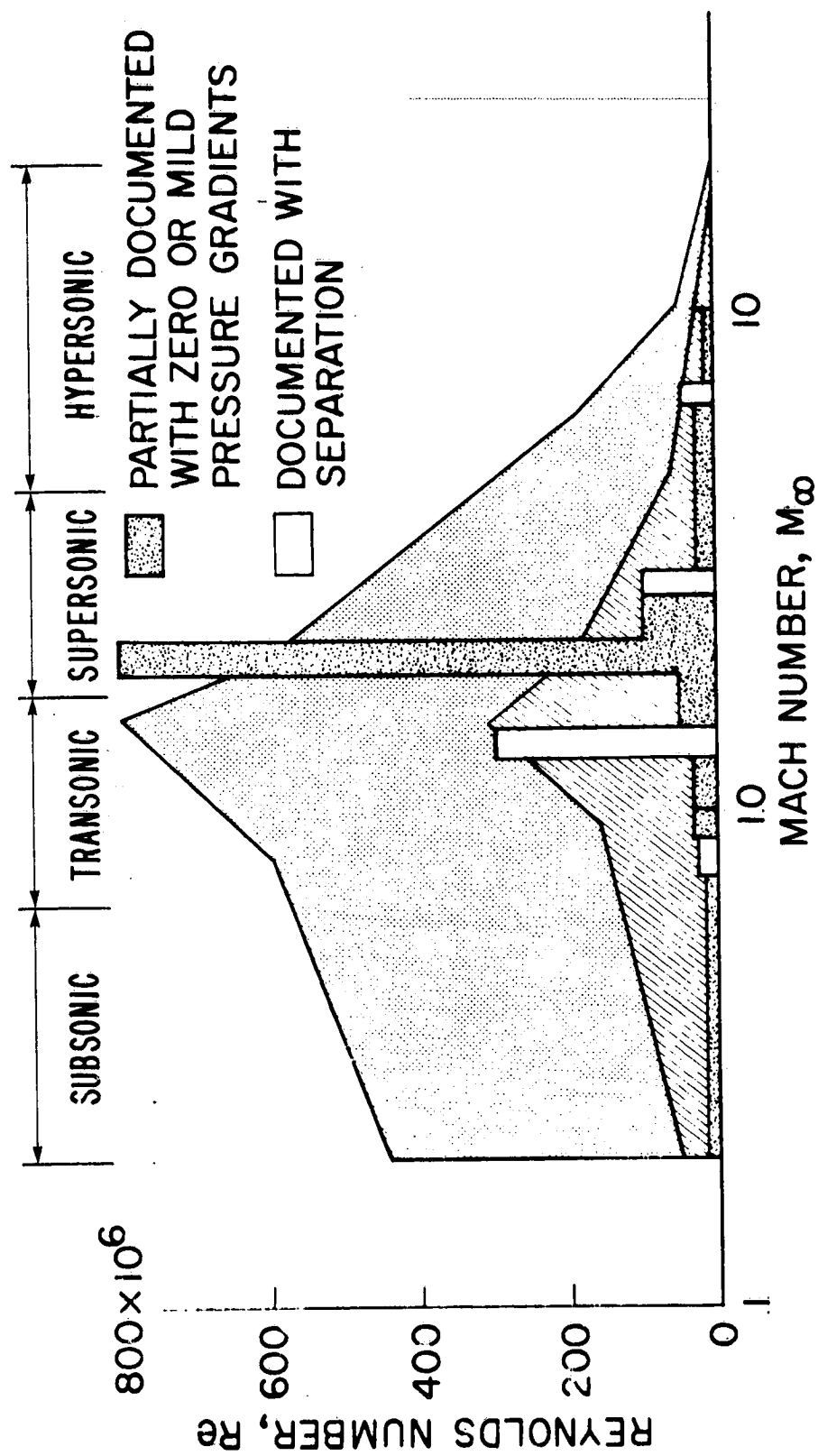


Figure 4.- Mach and Reynolds number domain for experiments compared with that for aerospace vehicles.

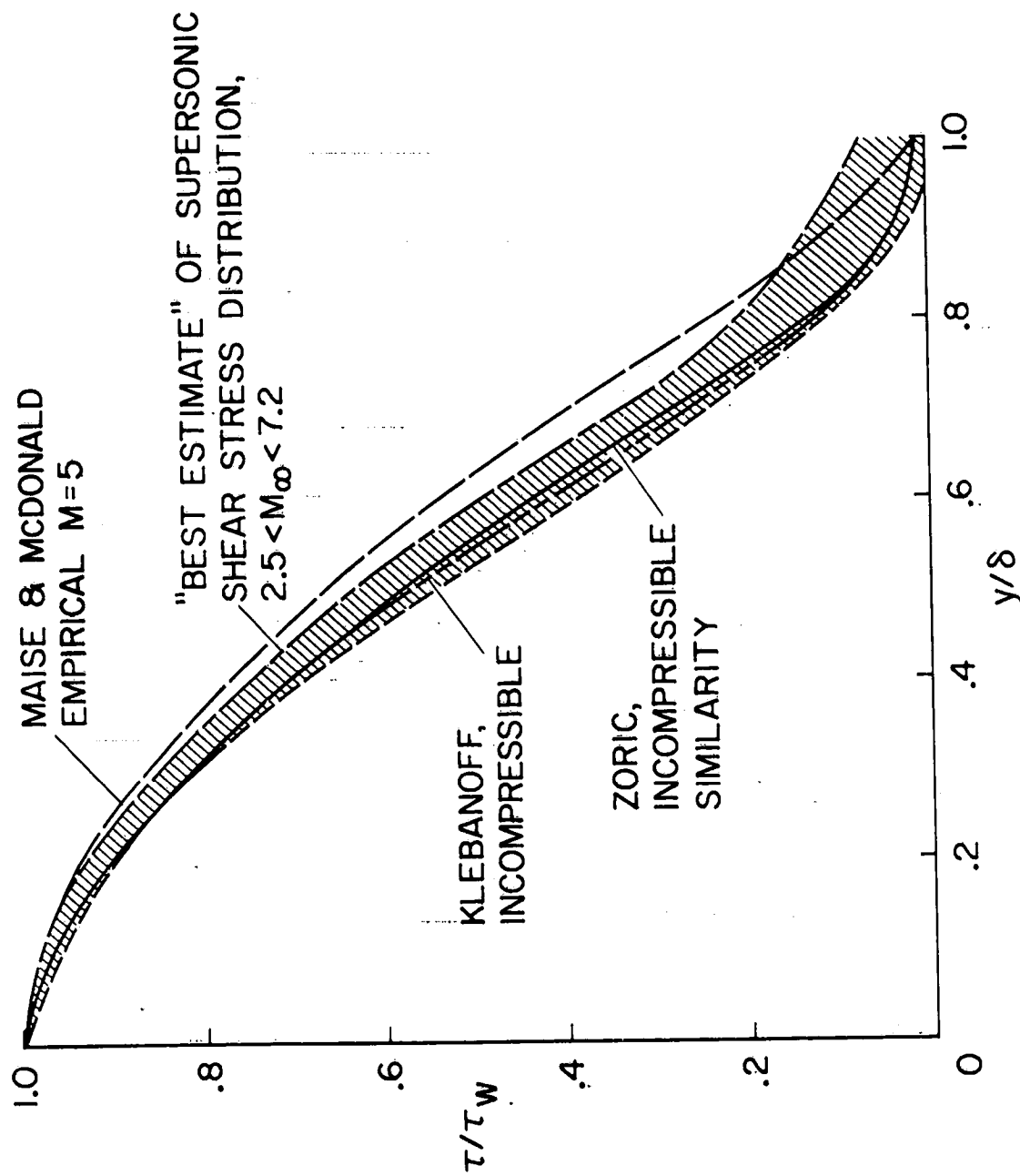


Figure 5.- Comparison of estimated supersonic shear stress with incompressible measurements and the empirical prediction of Maise and McDonald. (Taken from ref. 27.)

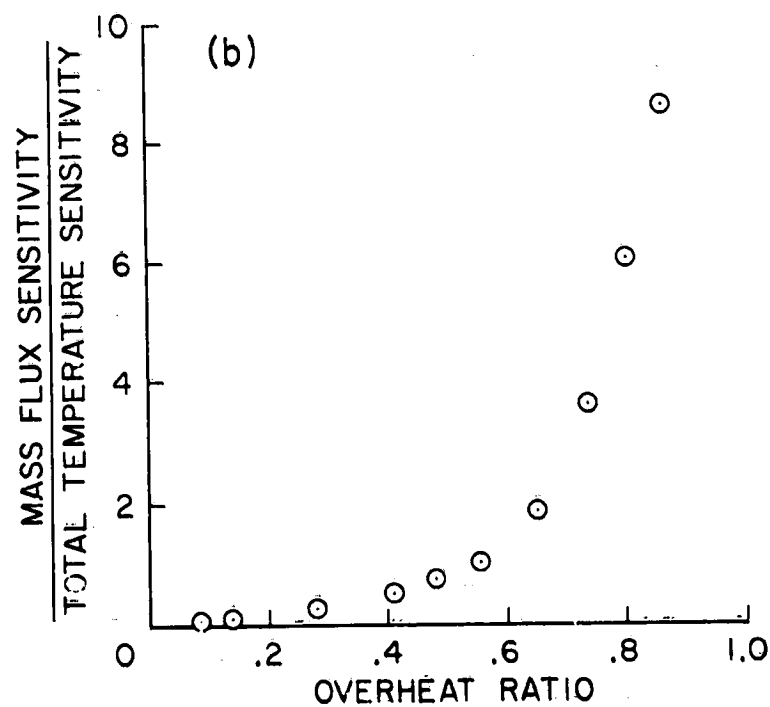
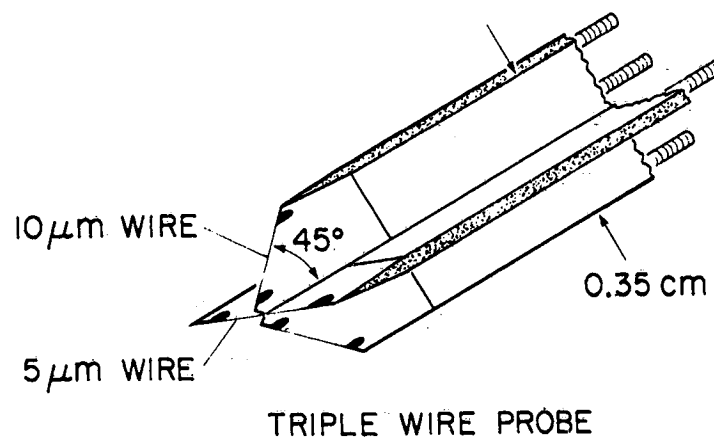
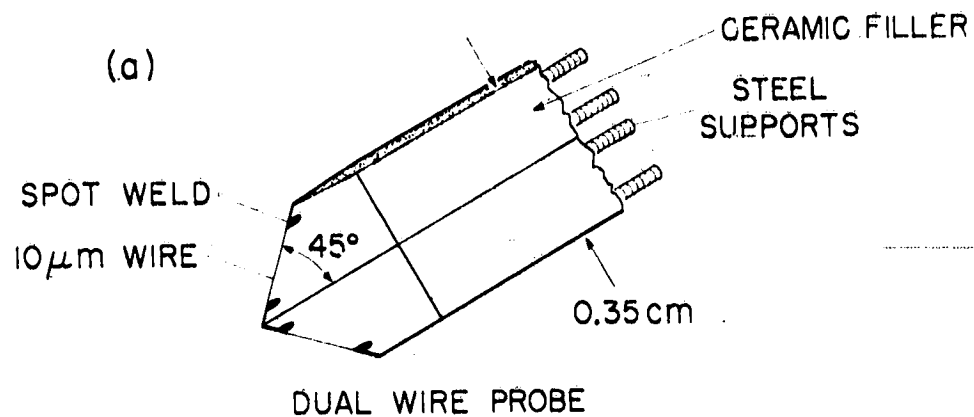


Figure 6.- Probes developed for high-temperature applications. (Taken from ref. 28.)

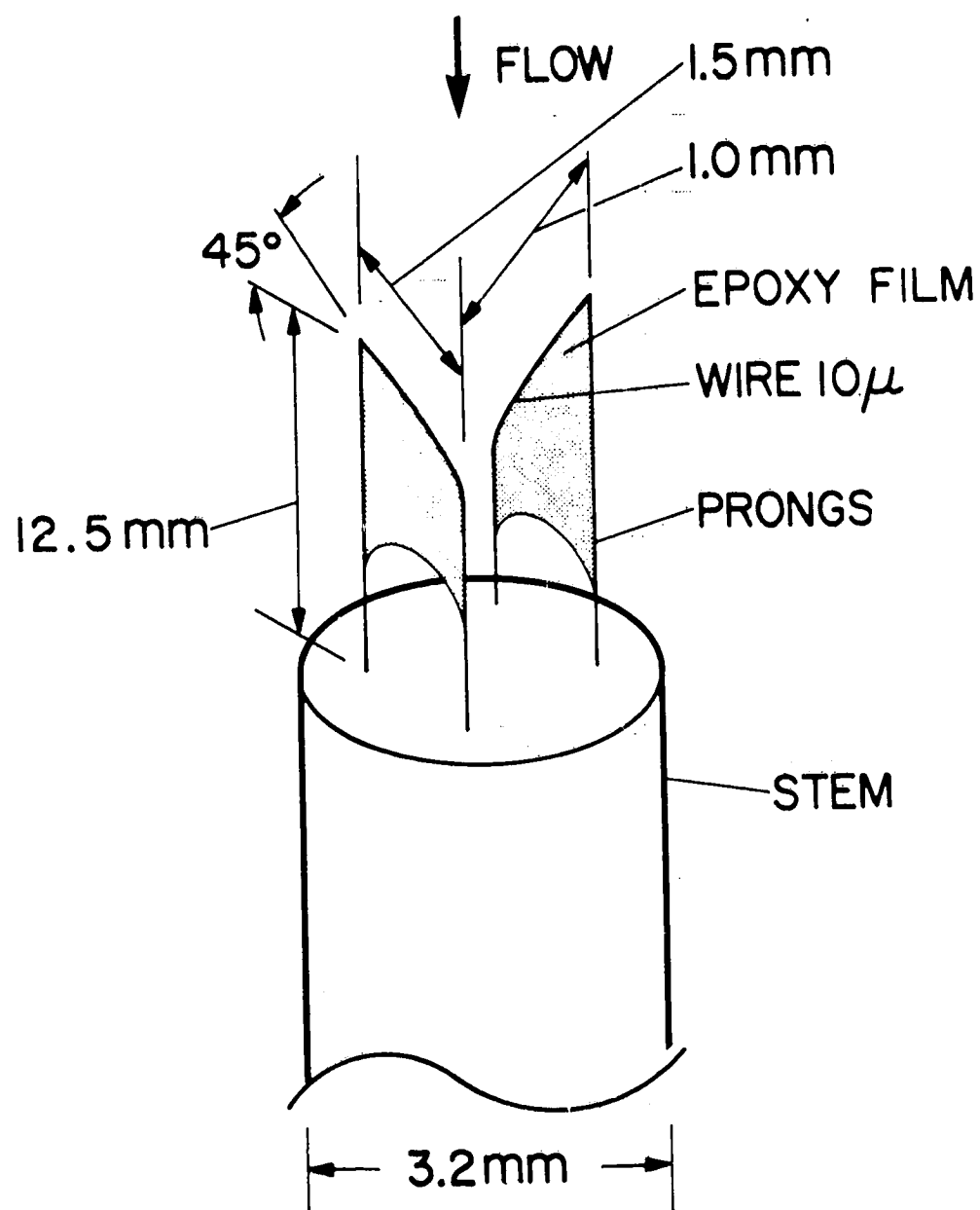


Figure 7.- Supported crossed hot-wire probe. (Taken from ref. 29.)

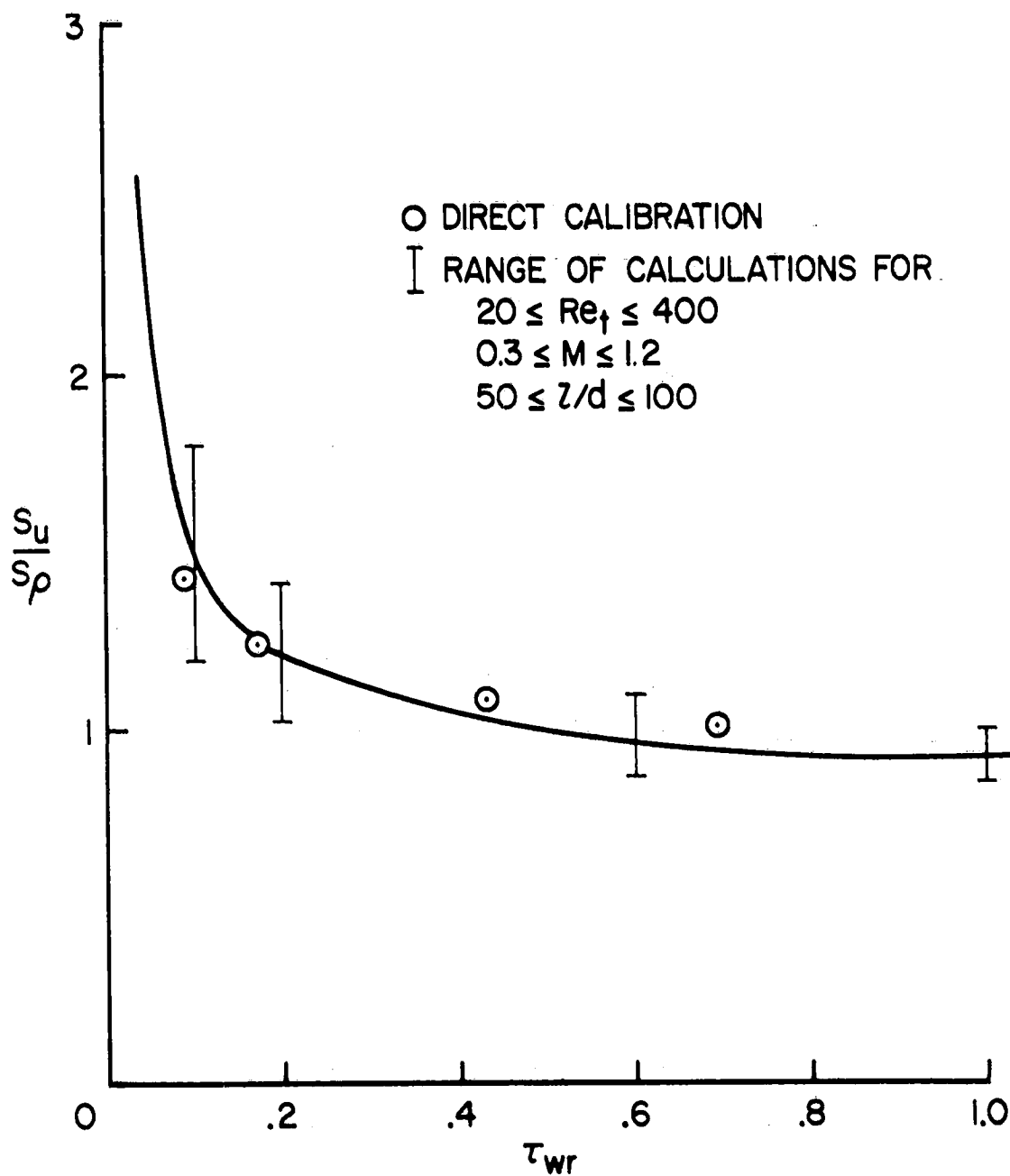


Figure 8.- Comparison of calculated and measured velocity-density sensitivity ratios. (Taken from ref. 31.)

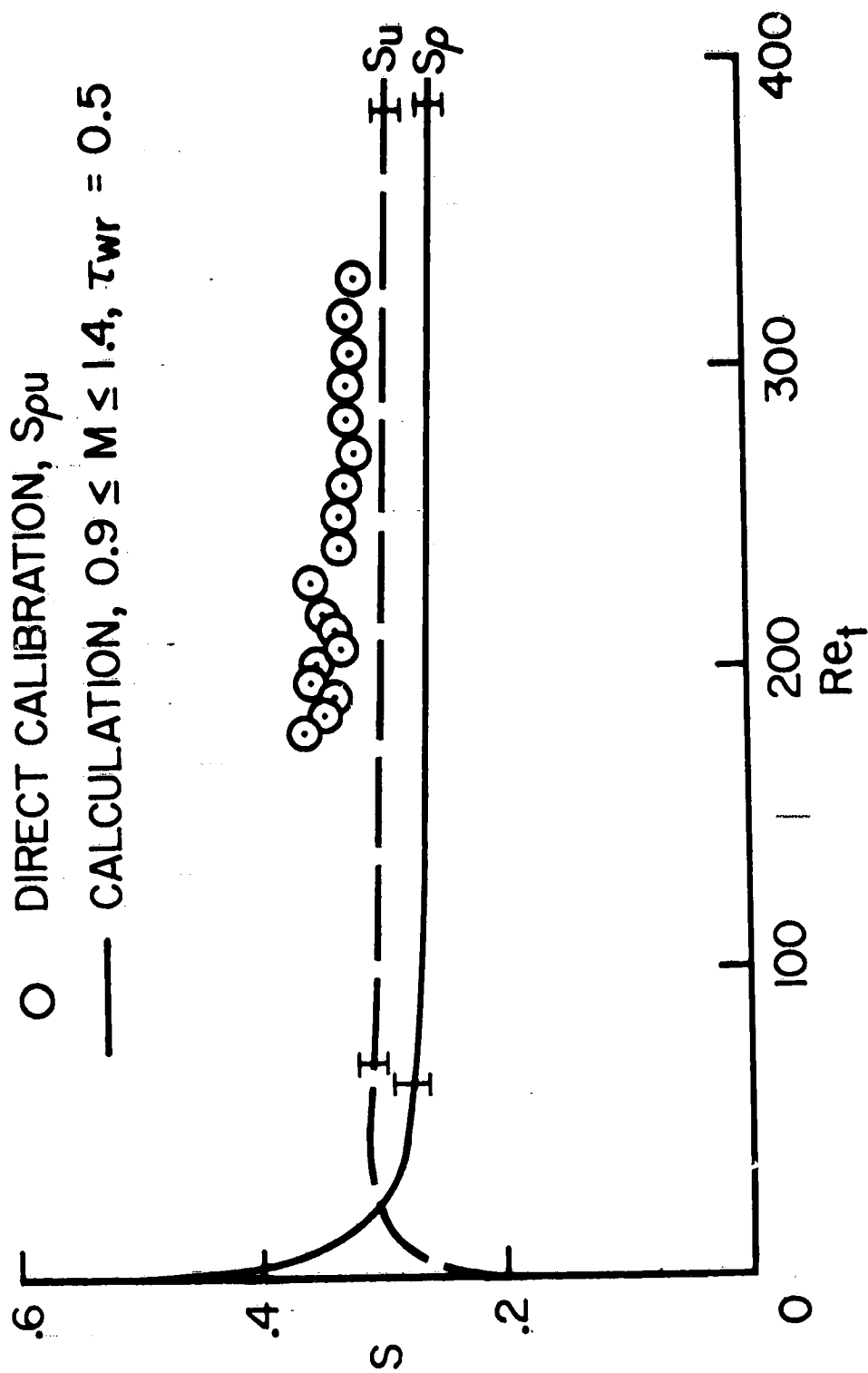


Figure 9.- Comparison of calculated density and velocity sensitivities and measured mass-flux sensitivity. (Taken from ref. 31.)

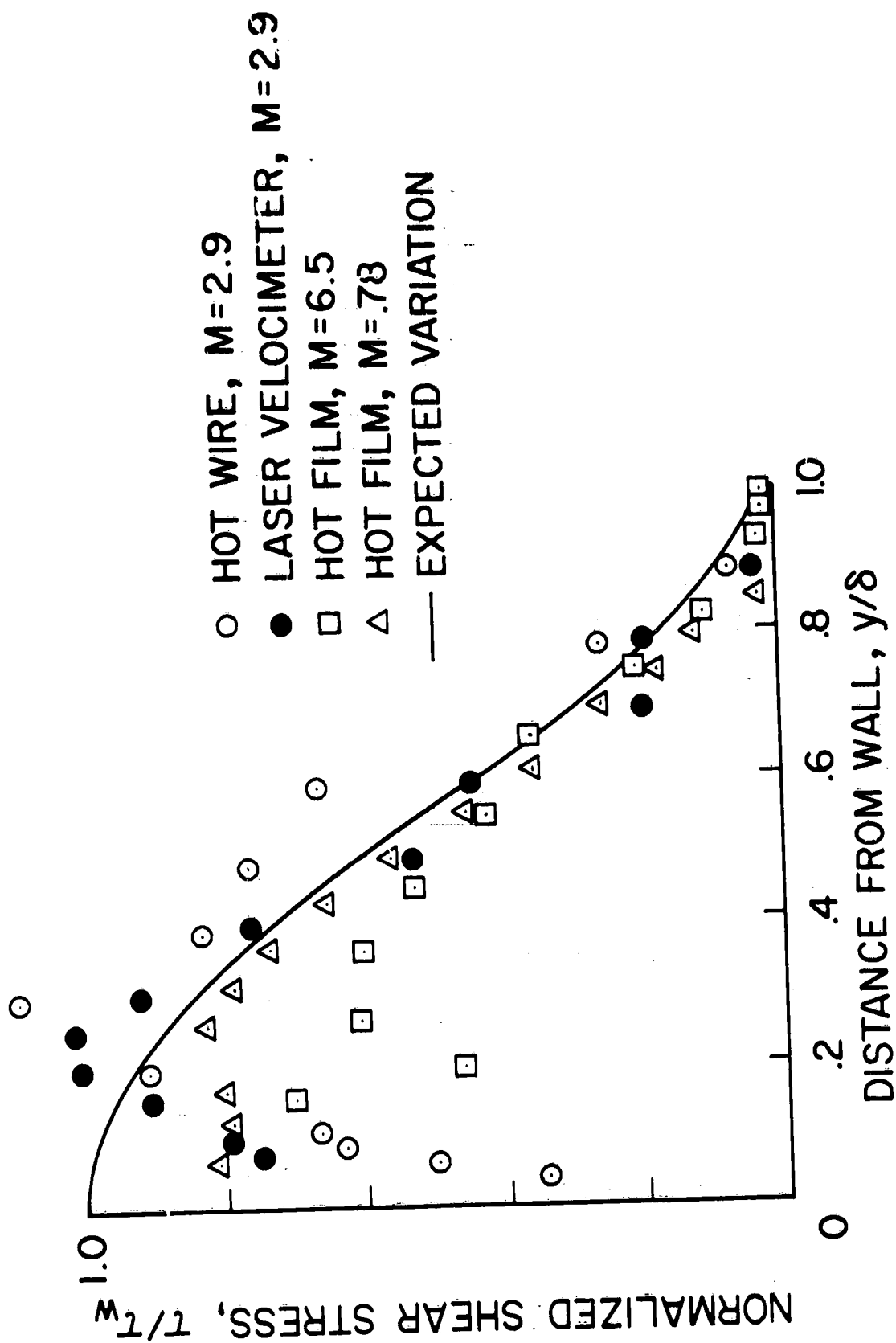


Figure 10.- Shear-stress measurements in compressible flows.

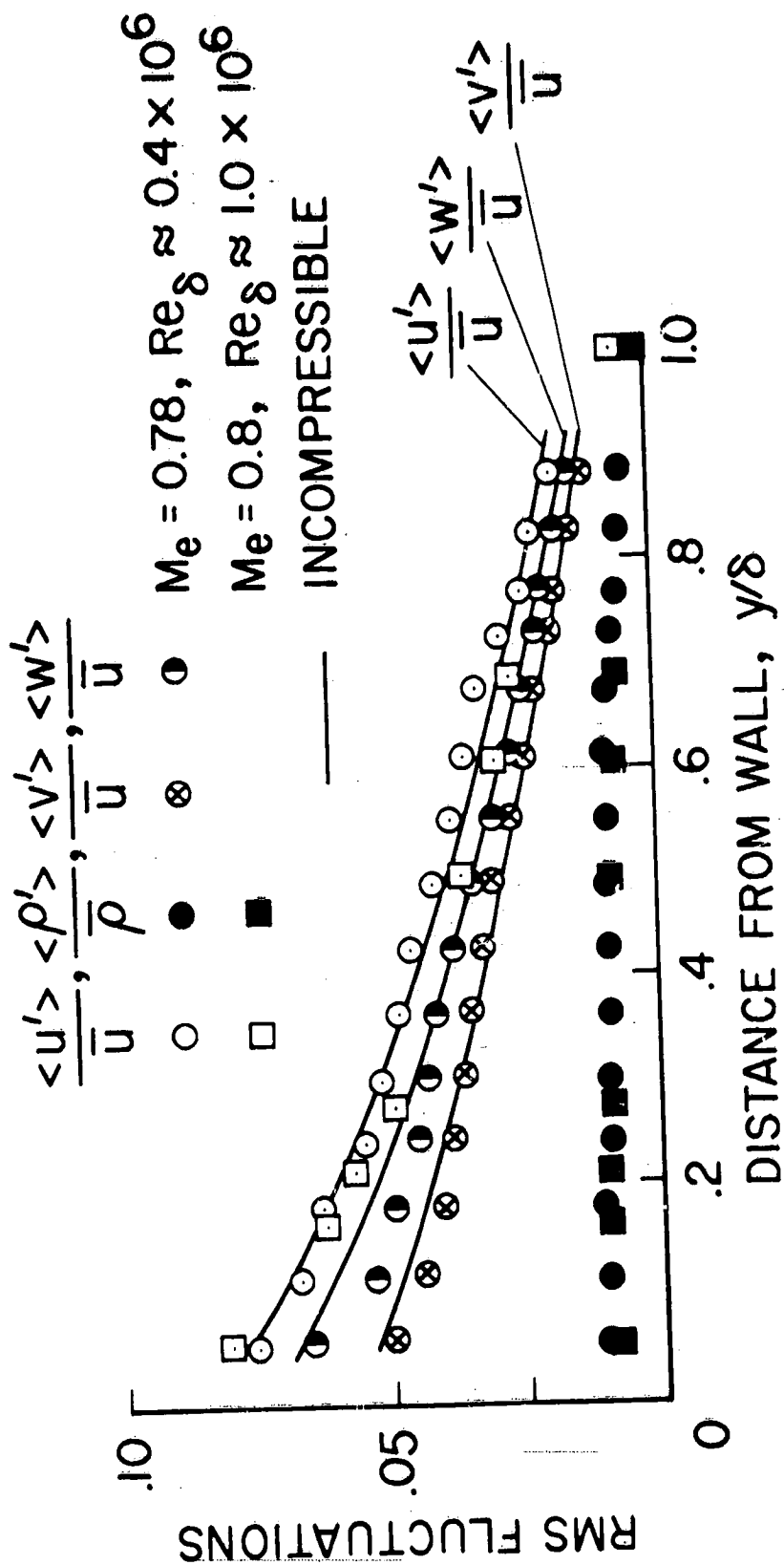
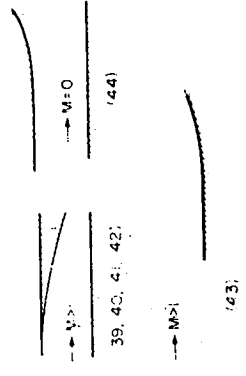
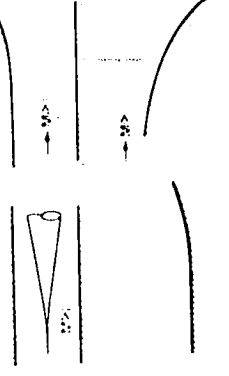
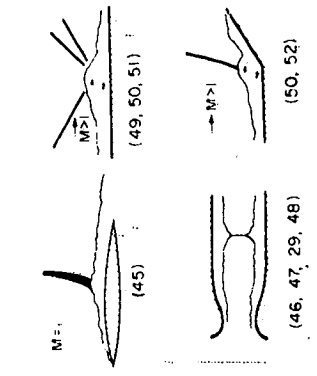
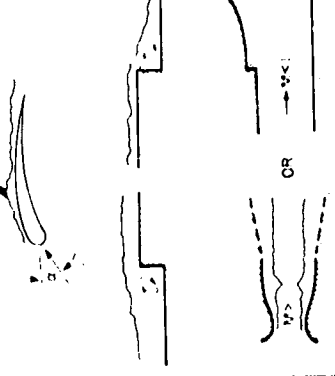
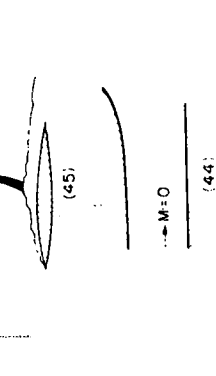
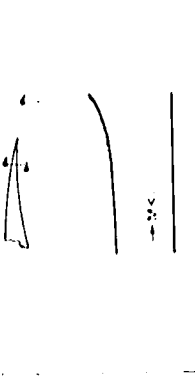
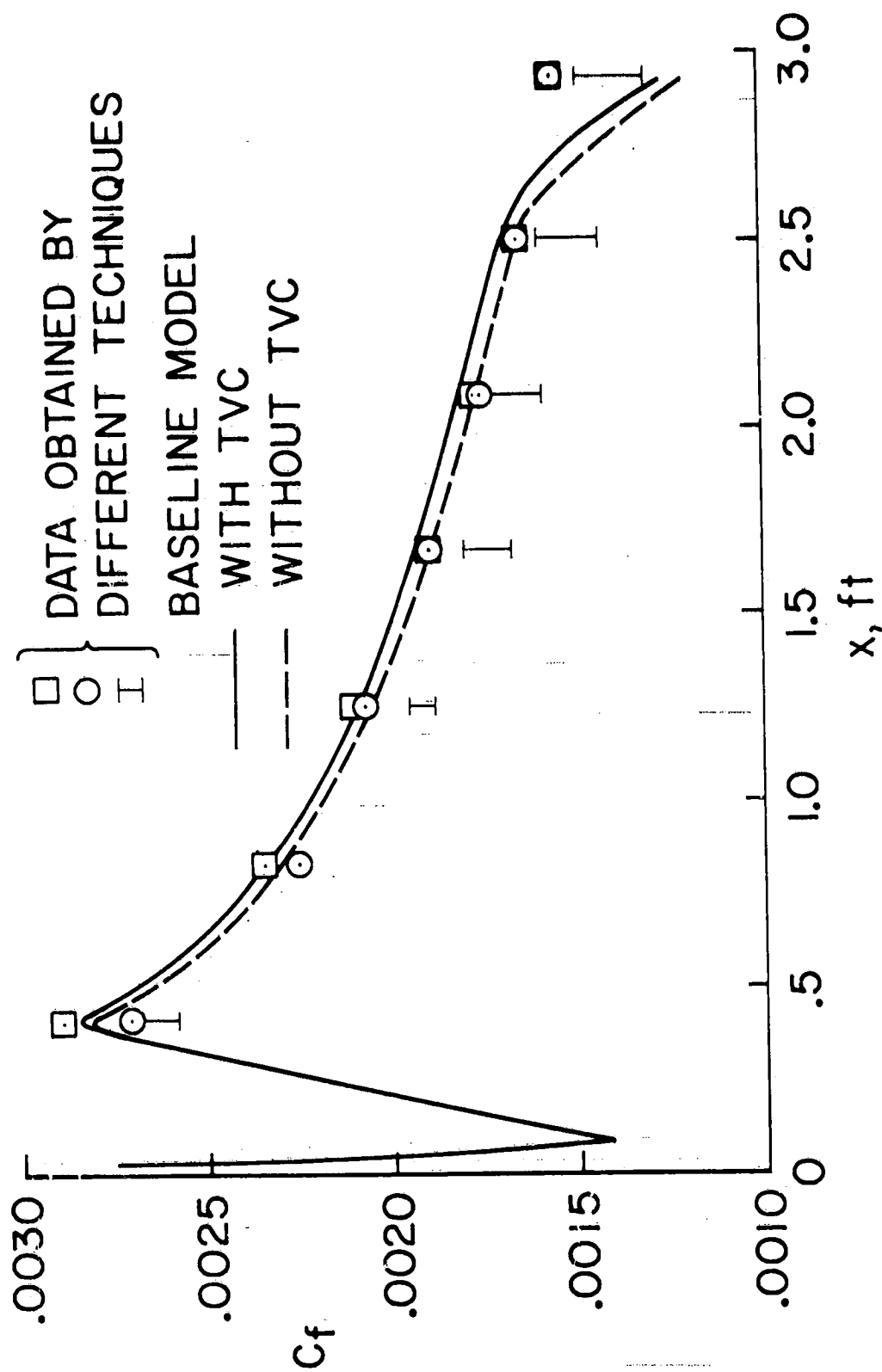


Figure 11.- Normalized rms velocity and density fluctuations across a compressible turbulent boundary layer.

FLOW FEATURES	BUILDING BLOCK EXPS	UNRESOLVED ISSUES	ADDITIONAL EXPS
① ATTACHED FLOW PRESSURE GRADIENTS WALL CURVATURE B.L. TRANSITION		RANGE OF PRESSURE GRADIENTS IS INCOMPLETE EFFECTS OF Re_∞ AND M_∞ UNKNOWN INSUFFICIENT DATA TO ASSESS WALL CURVATURE	
② SEPARATION & REATTACHMENT PRESSURE GRADIENTS SHOCK SEPARATION CORNER SEPARATION (FLAP) WALL CURVATURE STREAMLINE CURVATURE REVERSED FLOW FLOW UNSTEADINESS, ? COUPLING BETWEEN ②-③		REVERSED FLOW REGION INSUFFICIENT DATA EFFECTS OF UNSTEADINESS EFFECTS OF STREAMLINE CURVATURE EFFECTS OF PRESSURE GRADIENT UPSTREAM OF SEPARATION DOWNSTREAM OF REATTACHMENT EFFECT OF M_∞ , Re_∞ ON COUPLING	
③ TRAILING EDGE FLOW PRESSURE GRADIENTS SEPARATION REVERSE FLOW CORNER FLOW (FLAP) COUPLING BETWEEN ③-② ③-①		INSUFFICIENT DATA AT T.E. EFFECTS OF TWO B.L. MERGING EFFECTS OF PRESSURE GRADIENT AND Re ON SEPARATION	

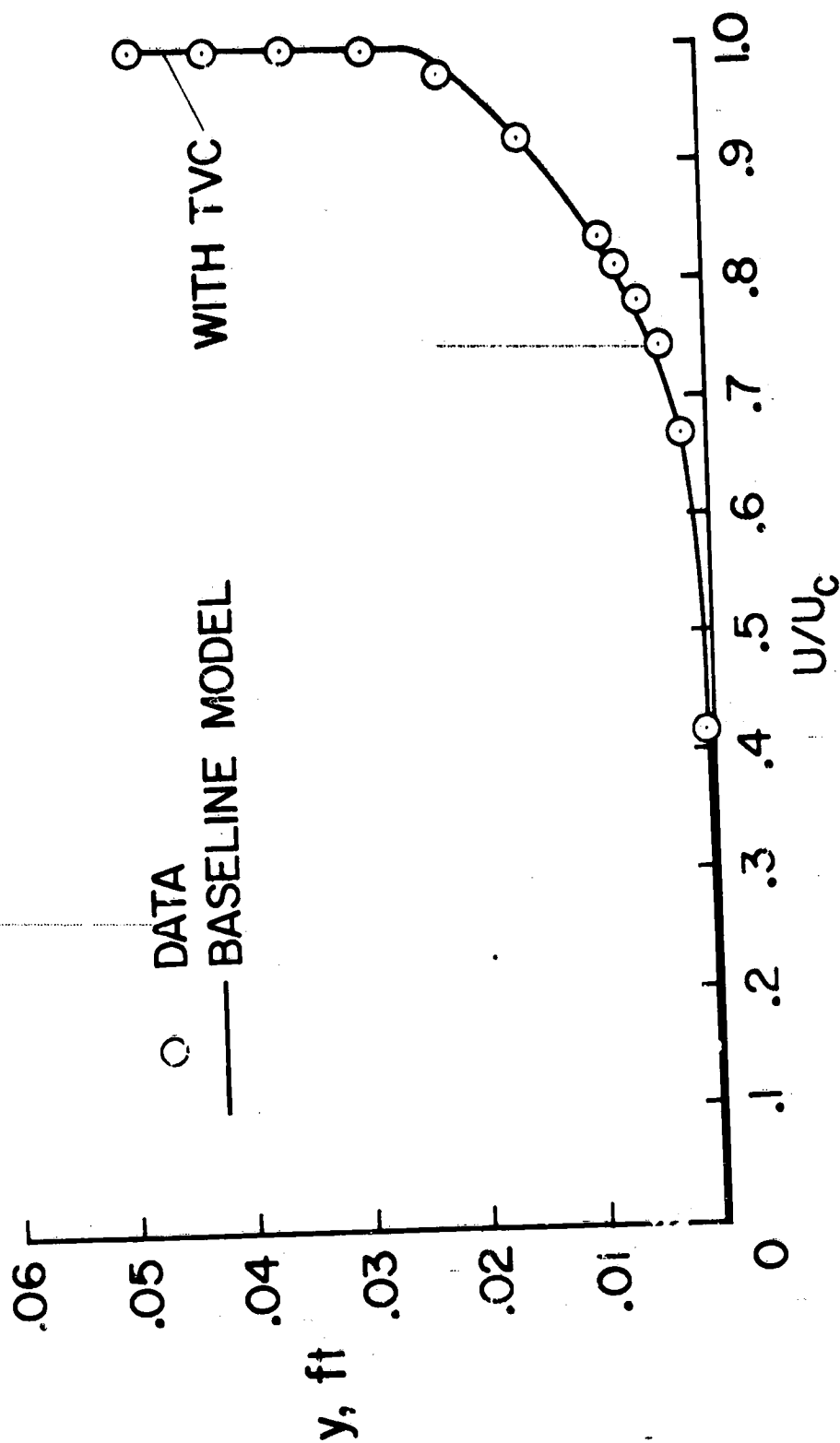
* NUMBERS REFER TO REFERENCES

Figure 12.- Model development for two-dimensional flows.



(a) Skin friction.

Figure 13.- Comparison of baseline turbulence model computation and data of Allen. (55)



(b) Velocity profile, $x = 2.08$ ft.

Figure 13.- Concluded.

$$\text{---}\triangle\text{---}\} \tau_t = -[\rho \langle u' v' \rangle + \langle \rho' u' v' \rangle]$$

$$\text{---}\text{---}\} \tau_t = -\rho \langle u' v' \rangle$$

$$Pr_t = 0.9$$

DATA	Me	T_w/T_o
○	7.367	0.172
□	7.4	0.418
◇	7.4	0.265

HOPKINS et al.

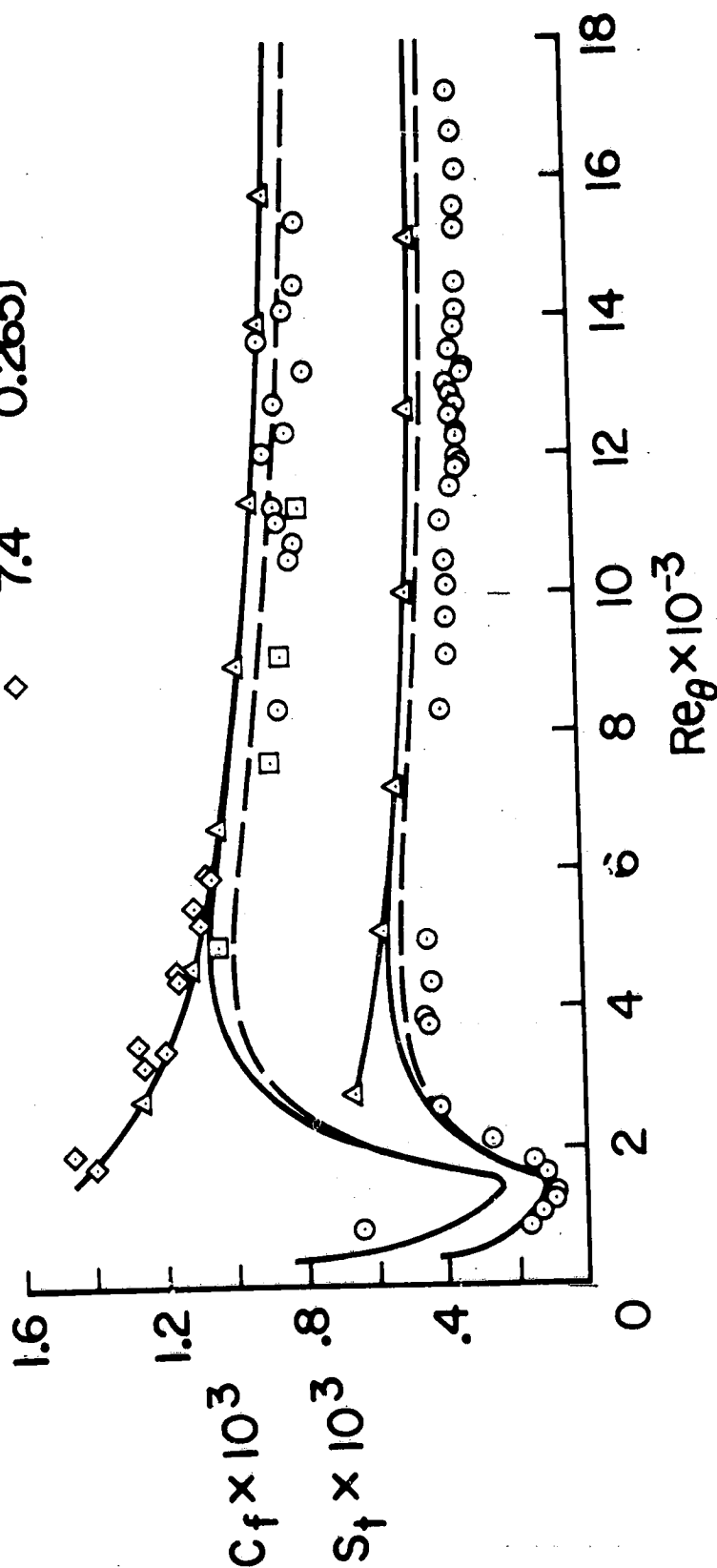


Figure 14.- Effect of density fluctuation on C_f and St at $Me = 7.4$.
(Taken from ref. 55.)

$$\text{---} \tau_t = -[\rho \langle u' v' \rangle + \langle \rho' u' v' \rangle]$$

$$\text{---} \tau_t = -\rho \langle u' v' \rangle$$

$$Pr_t = 0.9$$

DATA	M_e	T_w/T_o
○	10.72	0.194
□	10.57	0.201
◇	10.53	0.212
△	10.40	0.163

HOLDEN

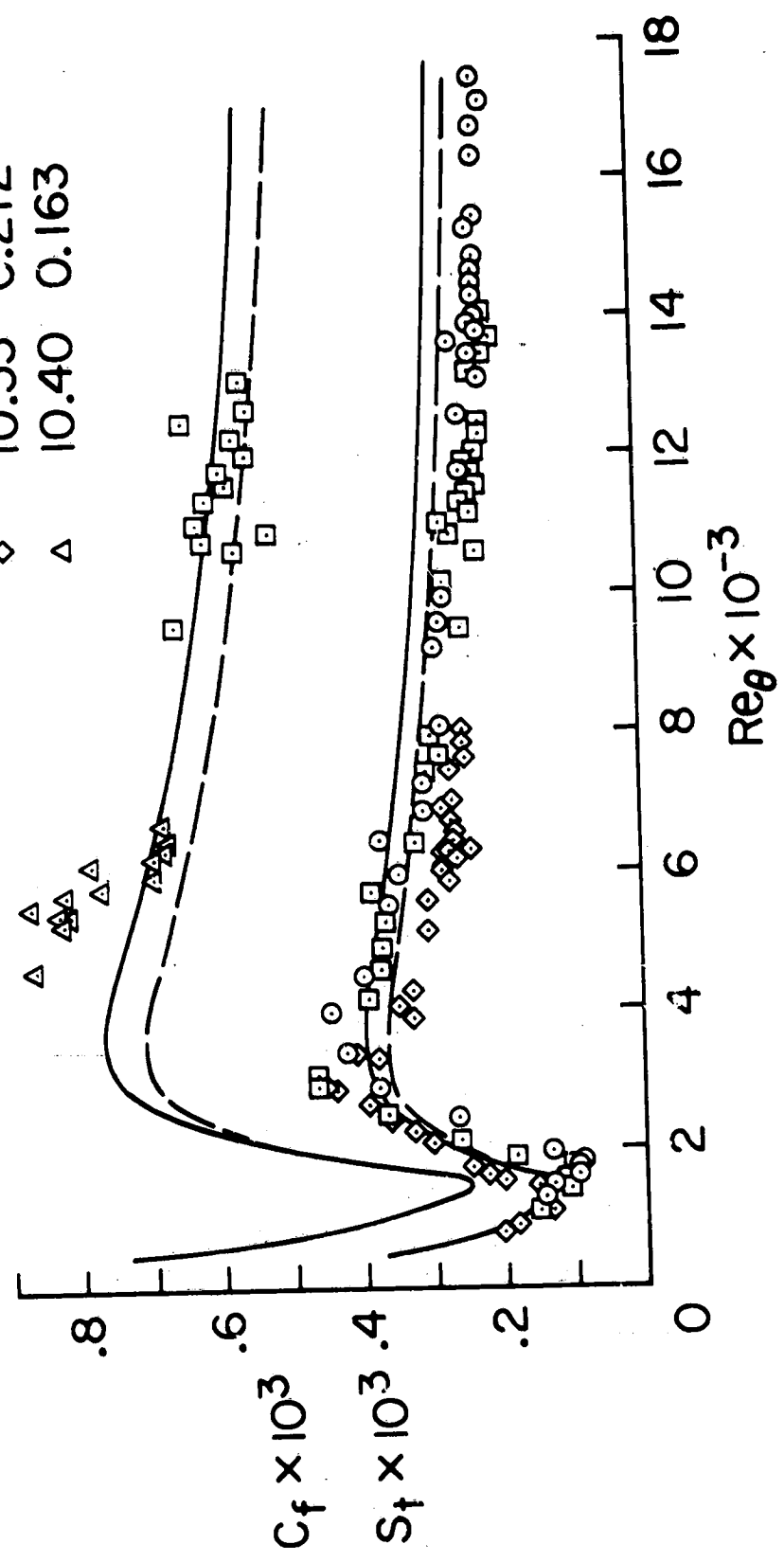


Figure 15.- Effect of density fluctuation on C_f and St at $M_2 = 10.5$.
(Taken from ref. 55.)

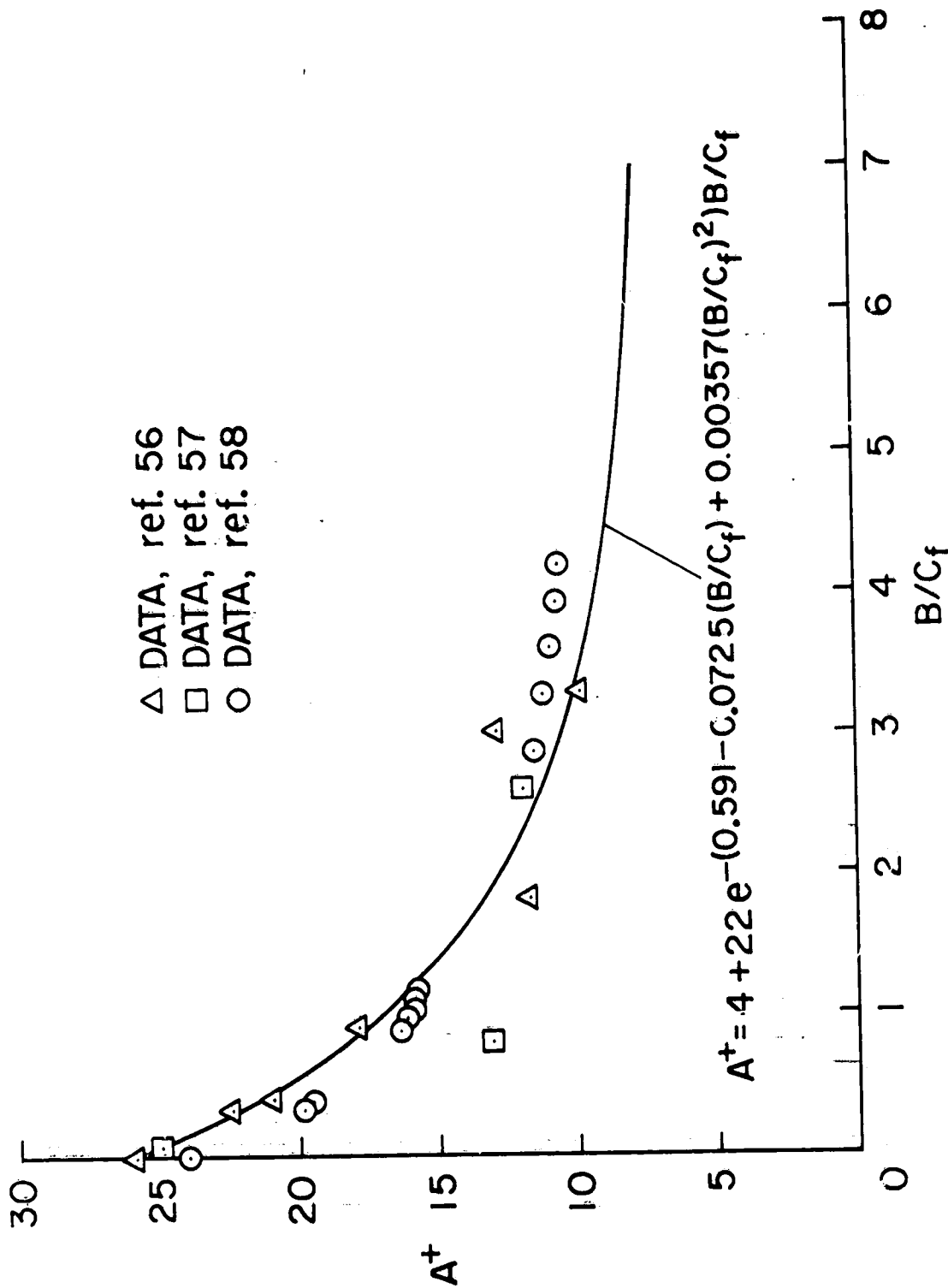
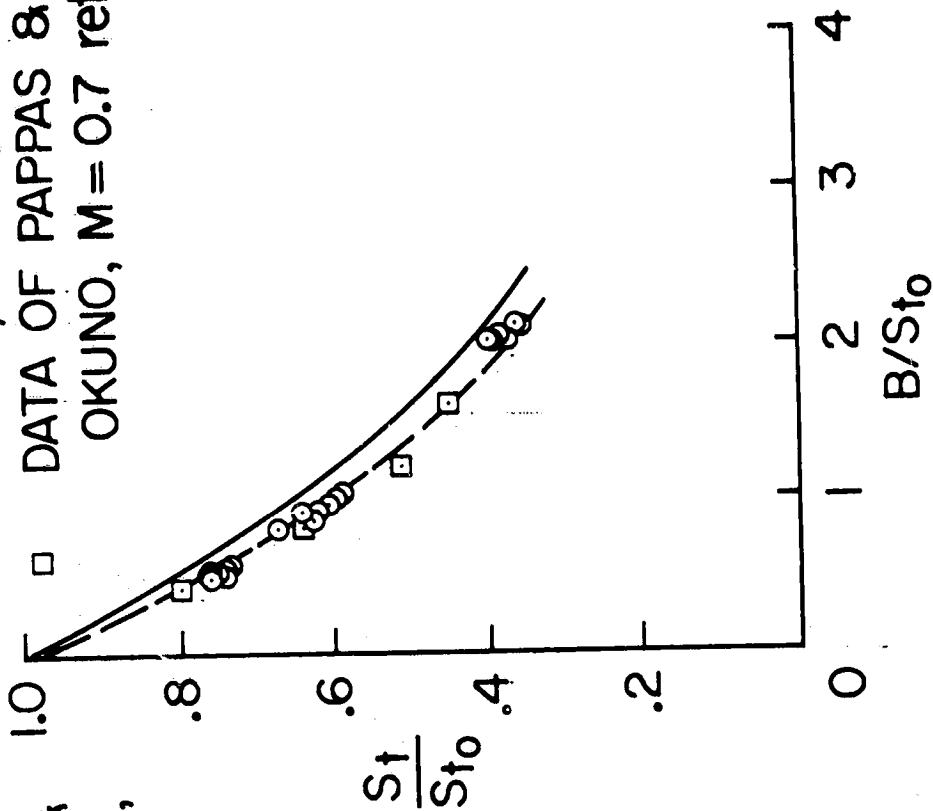


Figure 16.- Effects of mass transfer on baseline model constant, A^+ .

— THEORY, $M \approx 0$
 - - THEORY, $M = 0.7$
 ○ DATA OF MOFFAT &
 KAYS, $M \approx 0$, ref. 59
 □ DATA OF PAPPAS &
 OKUNO, $M = 0.7$ ref. 61



— THEORY, $M \approx 0$
 - - THEORY, $M = 3.67$
 ○ DATA OF ANDERSEN,
 $M \approx 0$, ref. 58
 △ □ DATA OF DERSHIN &
 LEONARD, $M = 3.2$,
 ref. 60

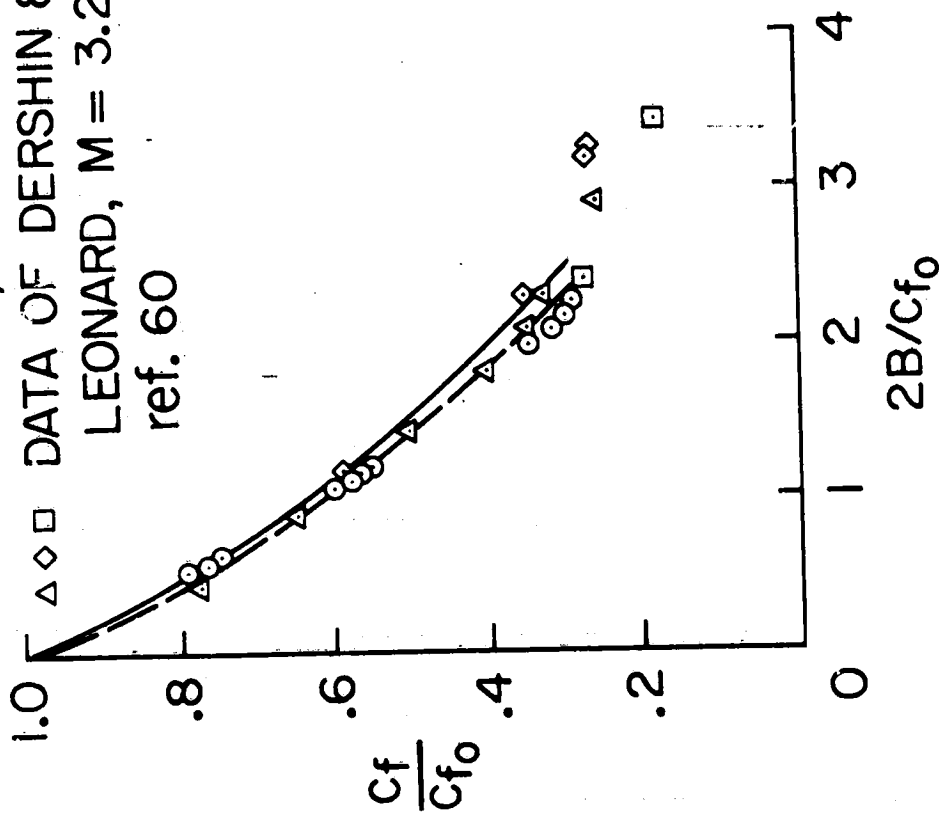


Figure 17.- Comparison between calculations using a modified baseline model and experiments for transpired boundary layers.


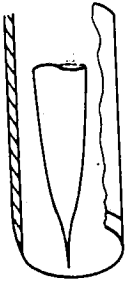

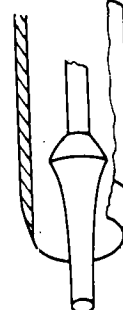
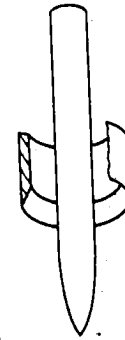
REFERENCE	EXPERIMENTAL CONFIGURATION	M_∞	$Re_{\theta_\infty} \times 10^{-4}$	T_w/T_0	P^+_{max}
ZWARTS		4.02	3.5	1	0.004
PEAKE, BRAKMANN AND ROMESKIE		3.93	1.1	1	0.006
STUREK AND DANBERG		3.54	2.0-2.8	1	0.0085- 0.0125
LEWIS, GRAN AND KUBOTA		3.98	0.5	1	0.011
KUSSOY AND HORSTMAN		6.7	0.8	0.43	0.07

Figure 18.- Experimental test flows used as standards of comparison for the turbulence models. (Taken from ref. 20.)

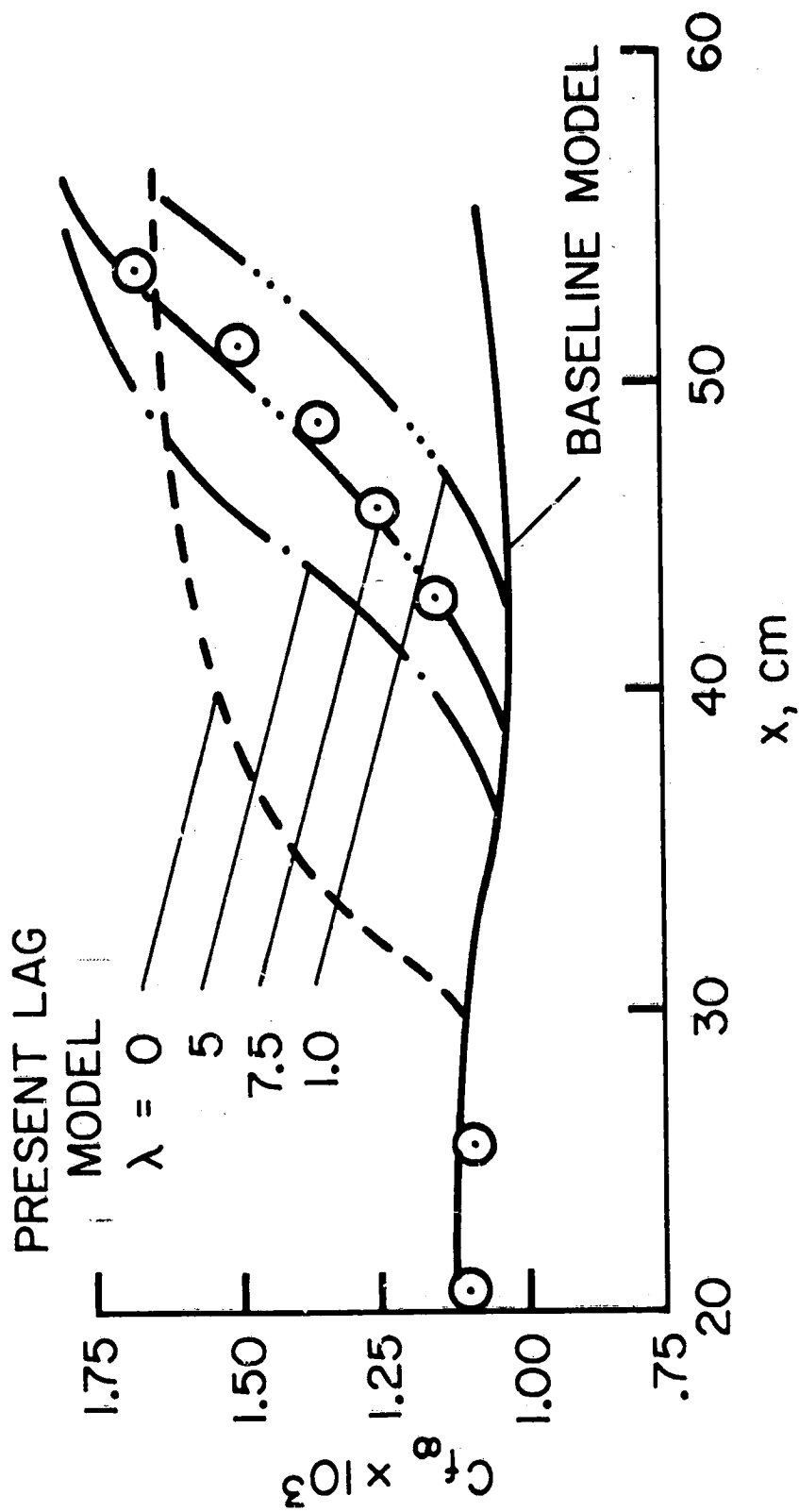
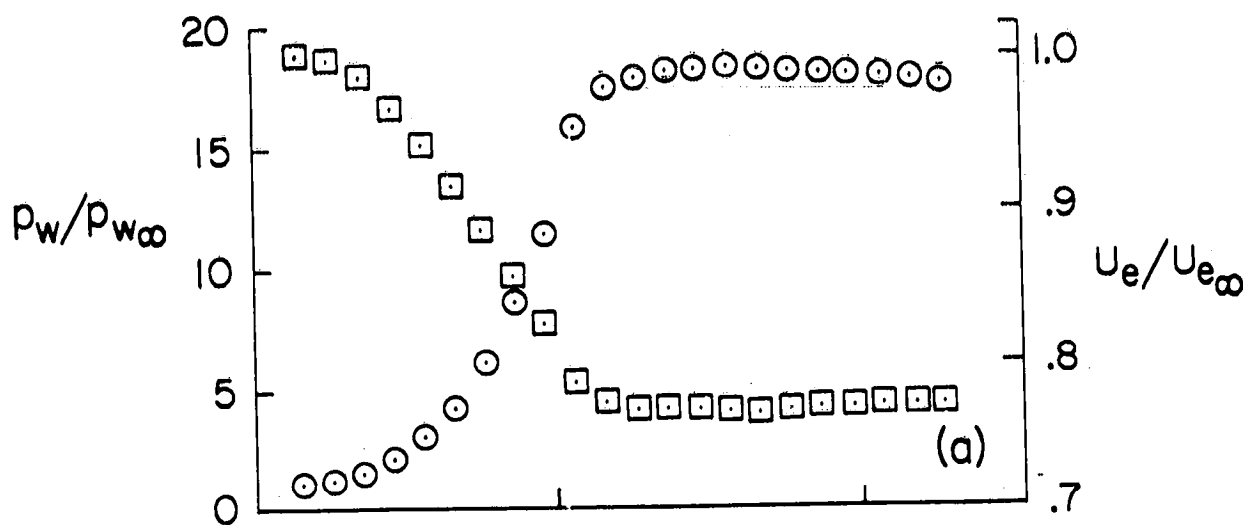
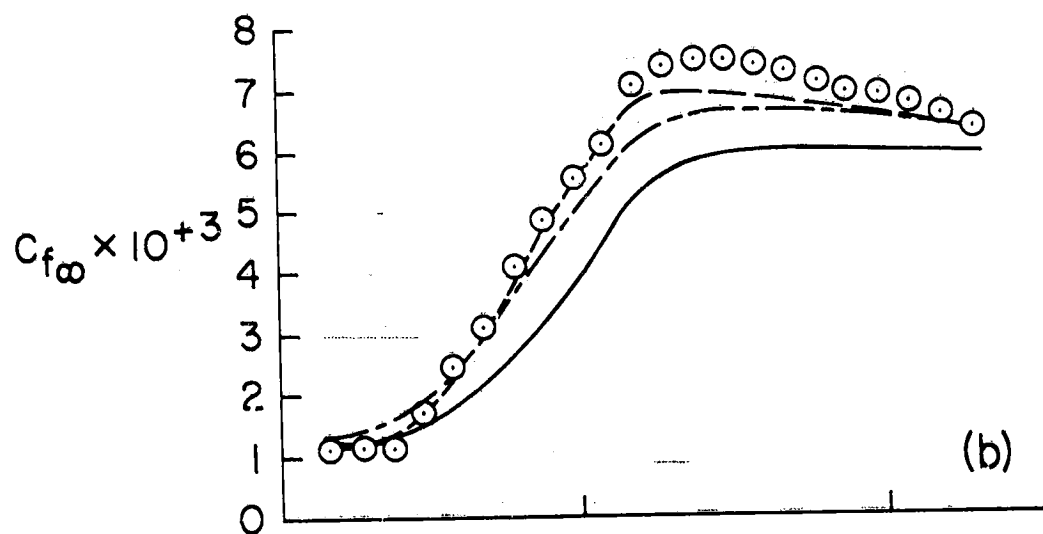


Figure 19.- Comparison of measured and computed skin friction distributions obtained using a turbulence model. (10)

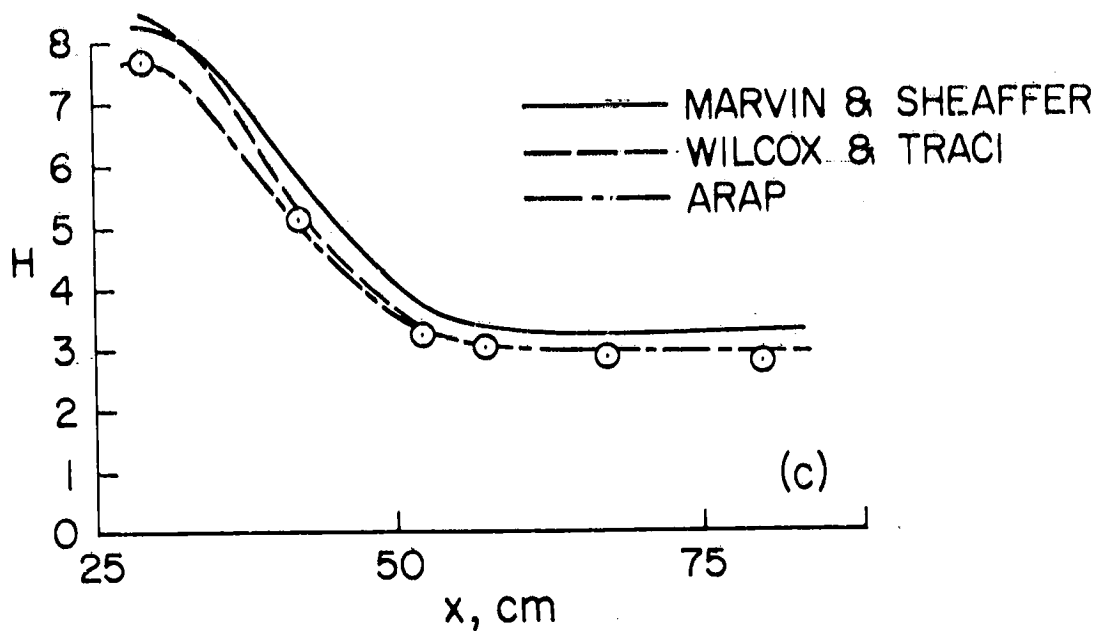


(a) Boundary-layer edge conditions.



(b) Local skin friction coefficient, based on free-stream dynamic pressure.

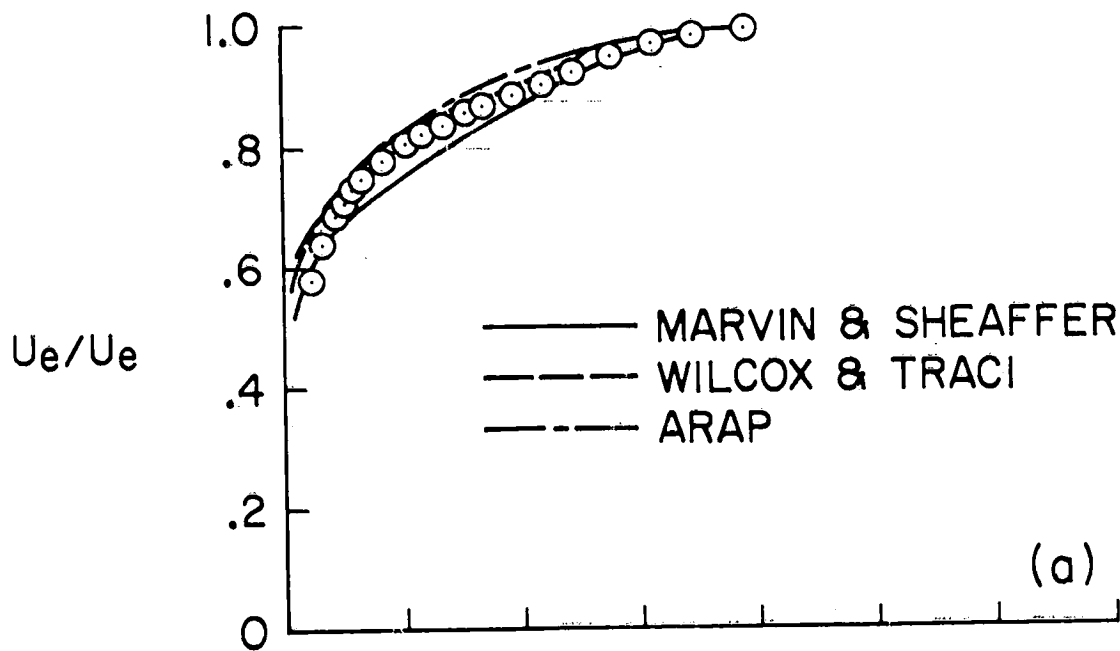
Figure 20.- Streamwise distributions of boundary-layer characteristics, experiment of Peake, Brakmann, and Romeskię. (Taken from ref. 20.)



(c) Local form factor.

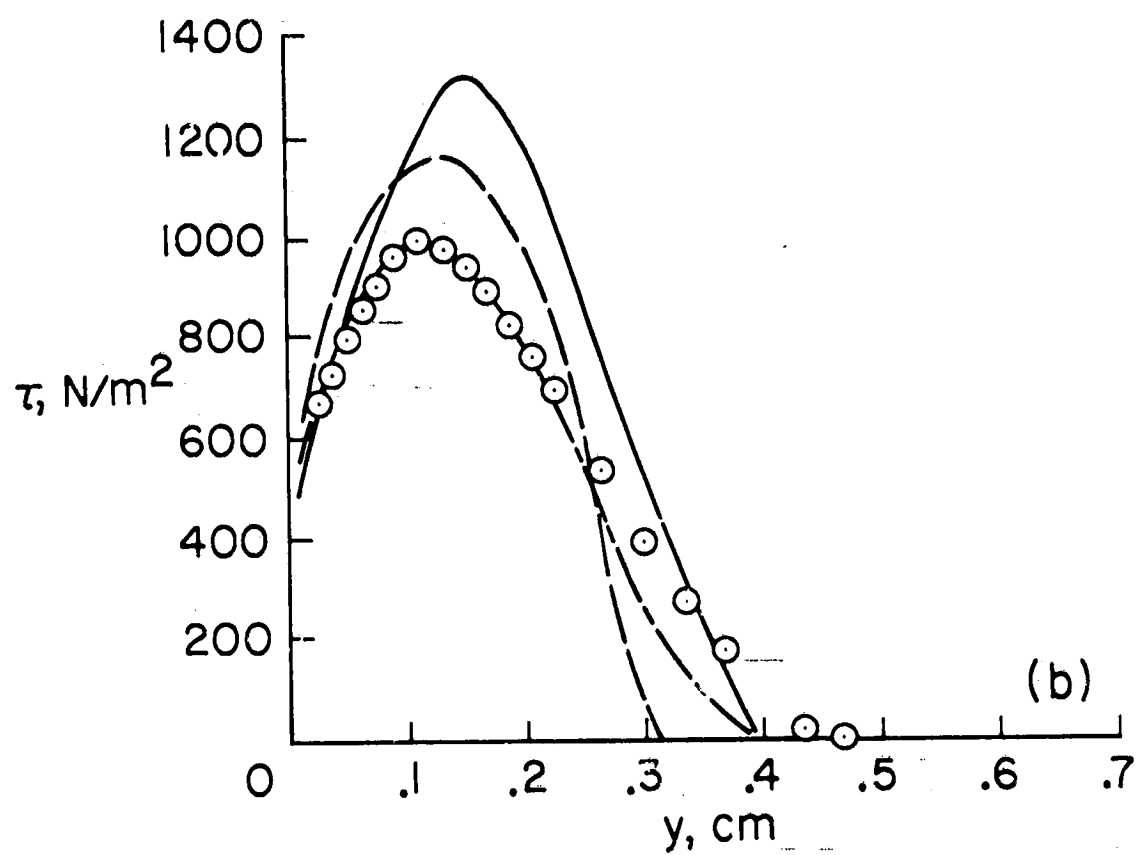
Figure 20.- Concluded.

$x = 52$ cm



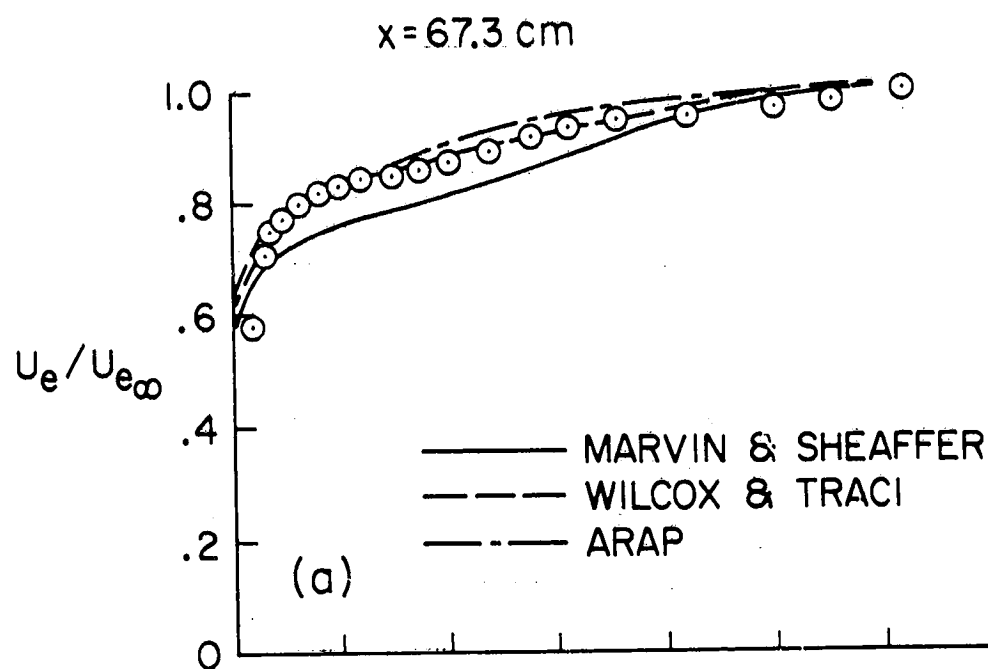
(a) Mean velocity profile.

Figure 21.- Velocity and turbulent shear stress profiles after run of adverse pressure gradient, data of Peake et al.: $x = 52$ cm. (Taken from ref. 20.)



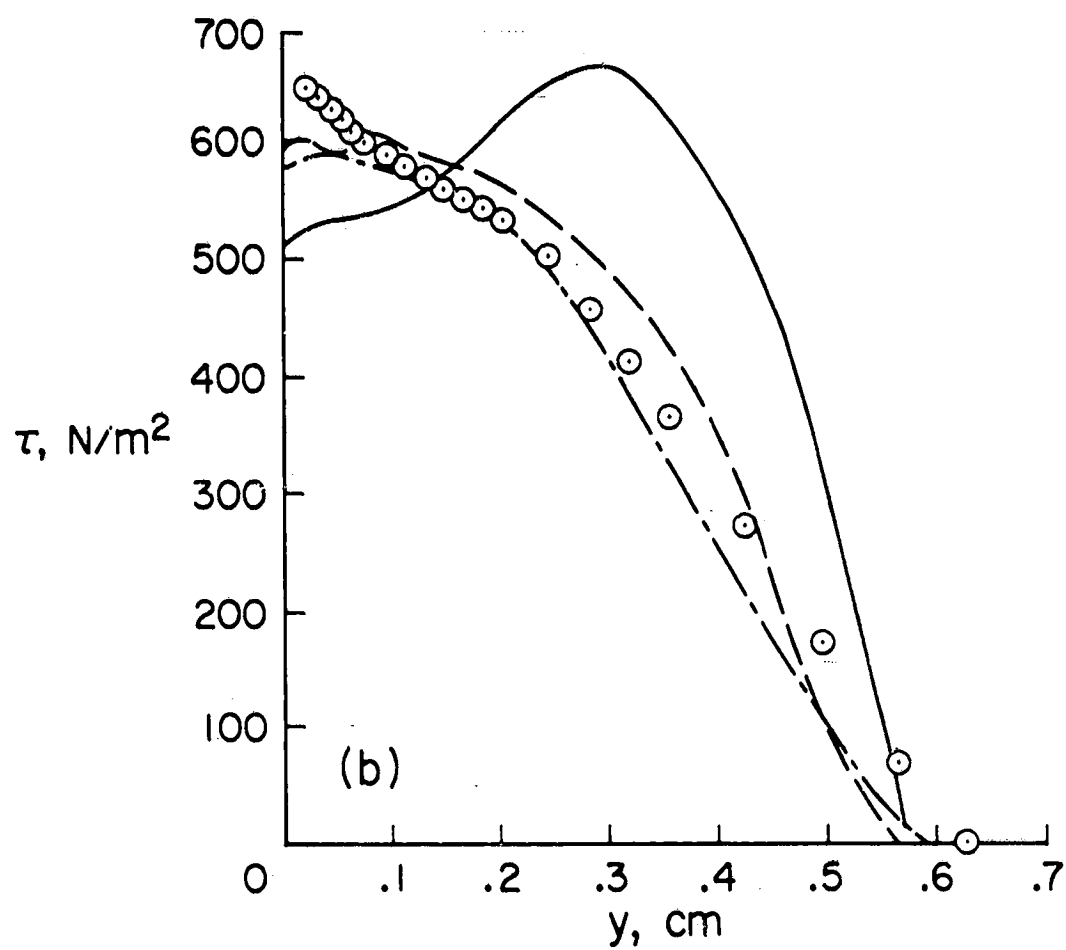
(b) Turbulent shear stress profile.

Figure 21.- Concluded.



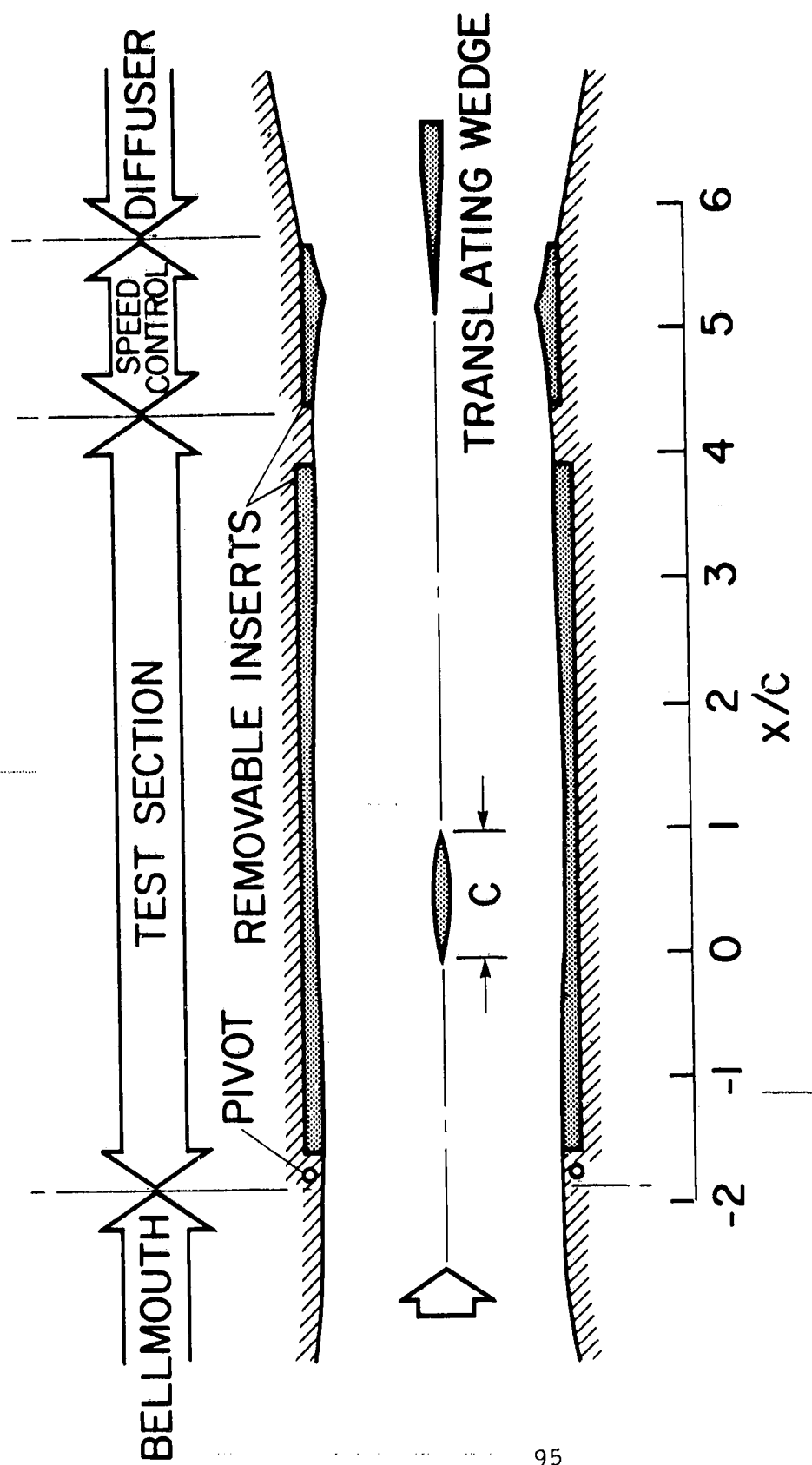
(a) Mean velocity profile.

Figure 22.- Mean velocity and turbulent shear stress profiles far downstream in Peake et al. experiment, $x = 67.3 \text{ cm}$. (Taken from ref. 20.)



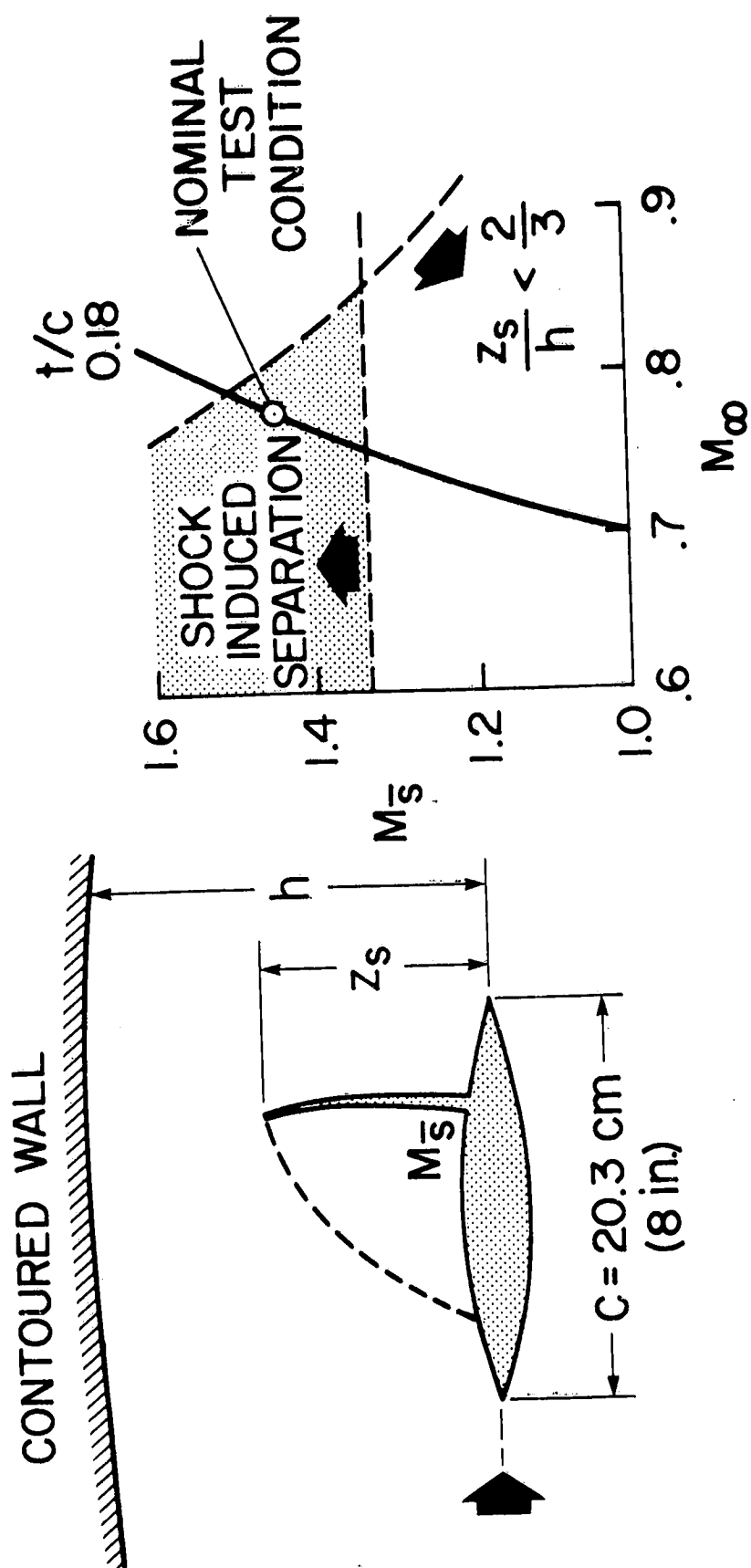
(b) Turbulent shear stress profile.

Figure 22.- Concluded.



(a) Overall arrangement.

Figure 23.- Experimental arrangement for a transonic wing undergoing shock-induced separation.



(b) Wing design.

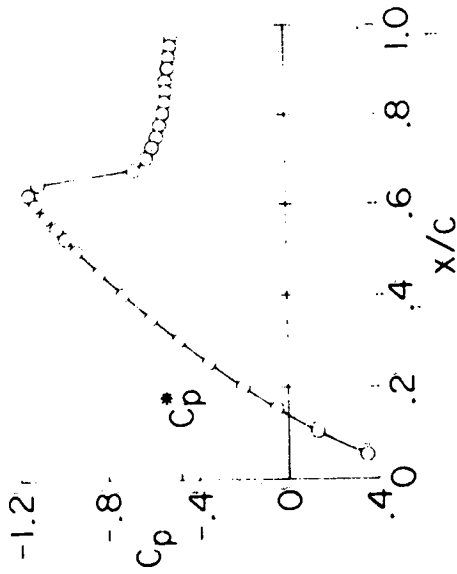
Figure 23.- Concluded.

TRANSONIC SHOCK-INDUCED SEPARATION

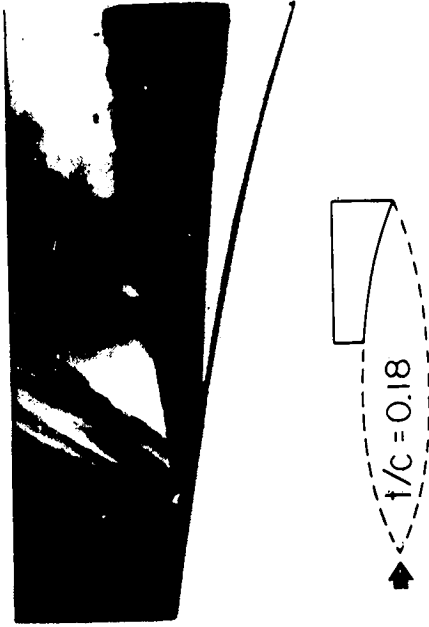
$M_\infty = .786$

$Re_c = 10.3 \times 10^6$

PRESSURE DISTRIBUTION



SHADOWGRAPH



OIL FLOW PATTERNS

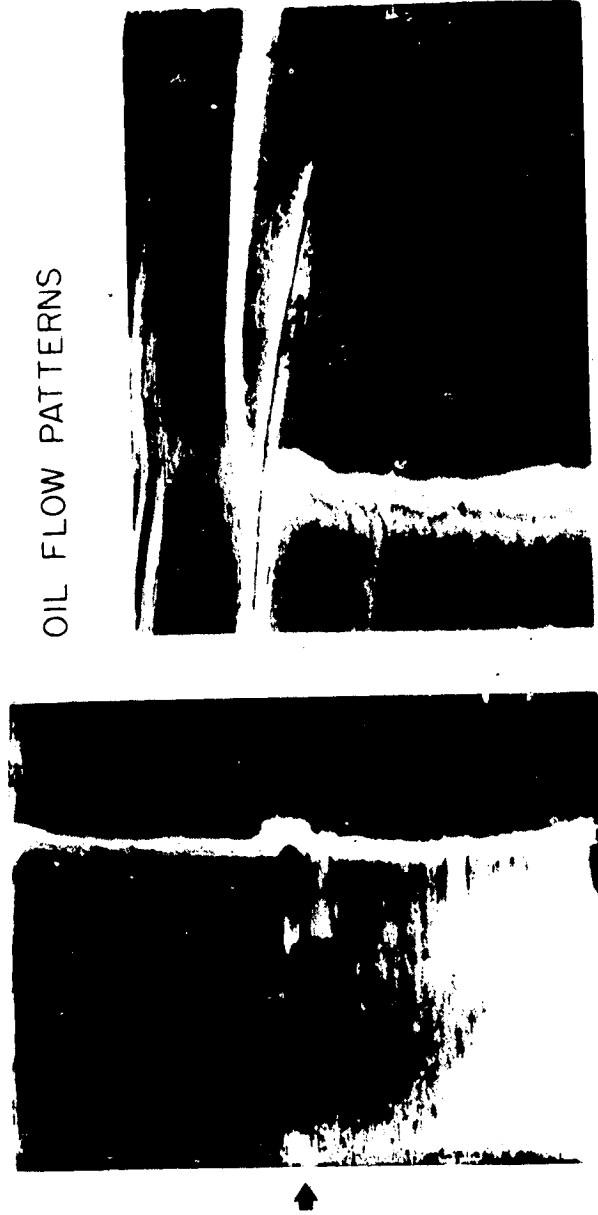


Figure 24.- Shock-induced boundary-layer separation experiment on a biconvex circular-arc airfoil; $Re = 10.3 \times 10^6$, $M_\infty = 0.786$.

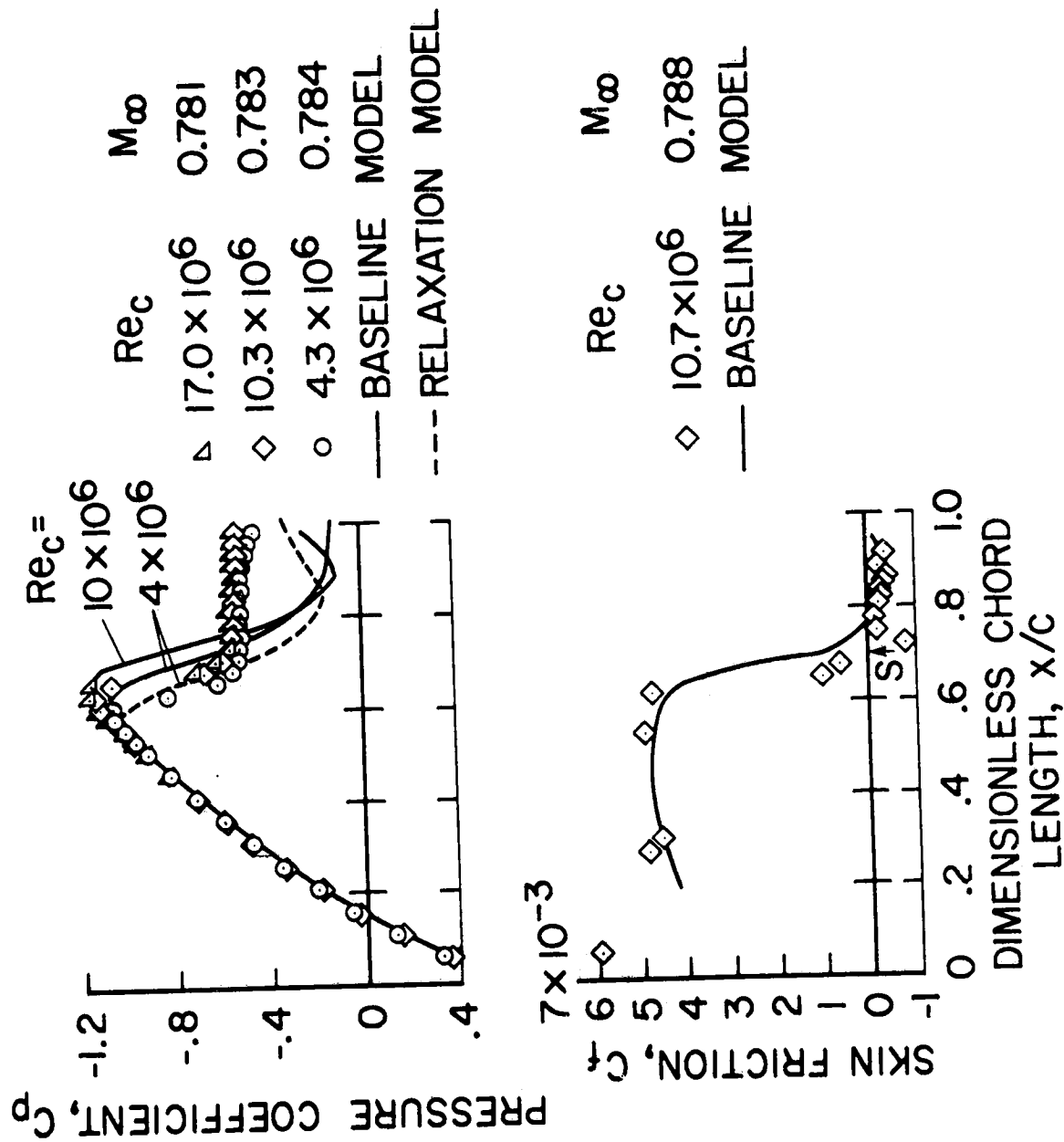


Figure 25.- Results from the shock-induced separation experiment on a biconvex circular-arc airfoil.

$$M_{\infty} = 1.5 \quad Re_{\delta_u} = 10^5 - 10^6$$

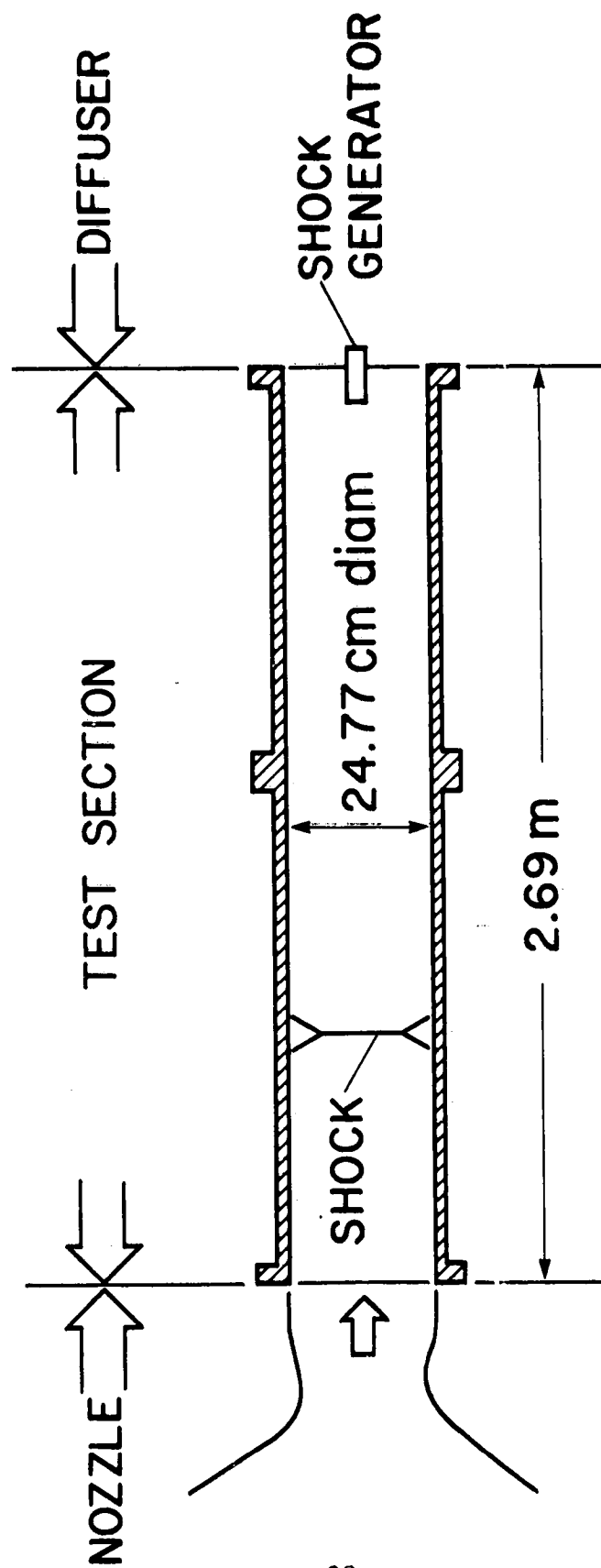


Figure 26.- Experimental arrangement for a normal shock-wave, turbulent boundary-layer experiment with separation.

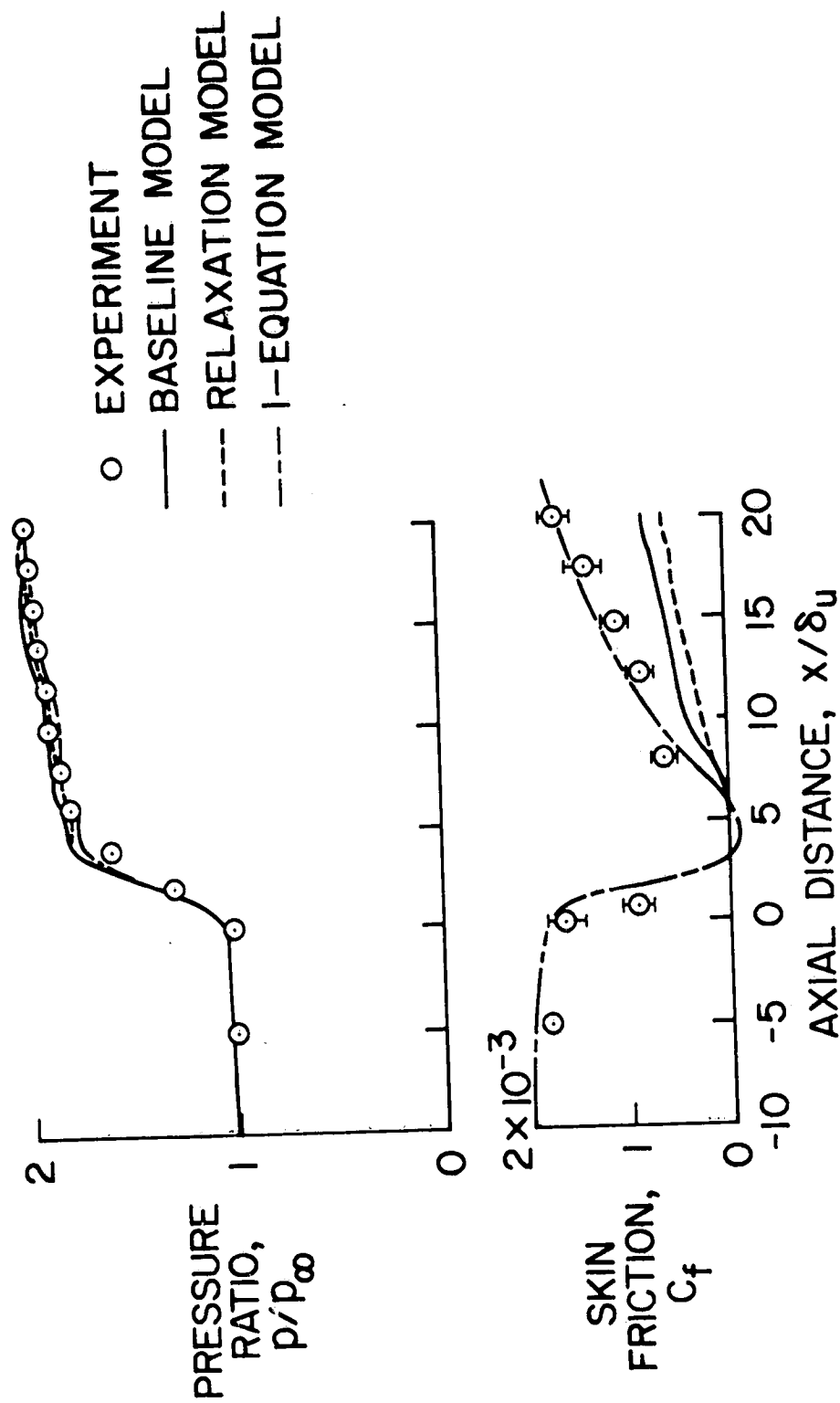


Figure 27.- Results from normal shock-wave experiment; $M_\infty = 1.44$ and $Re_x = 37 \times 10^6$.

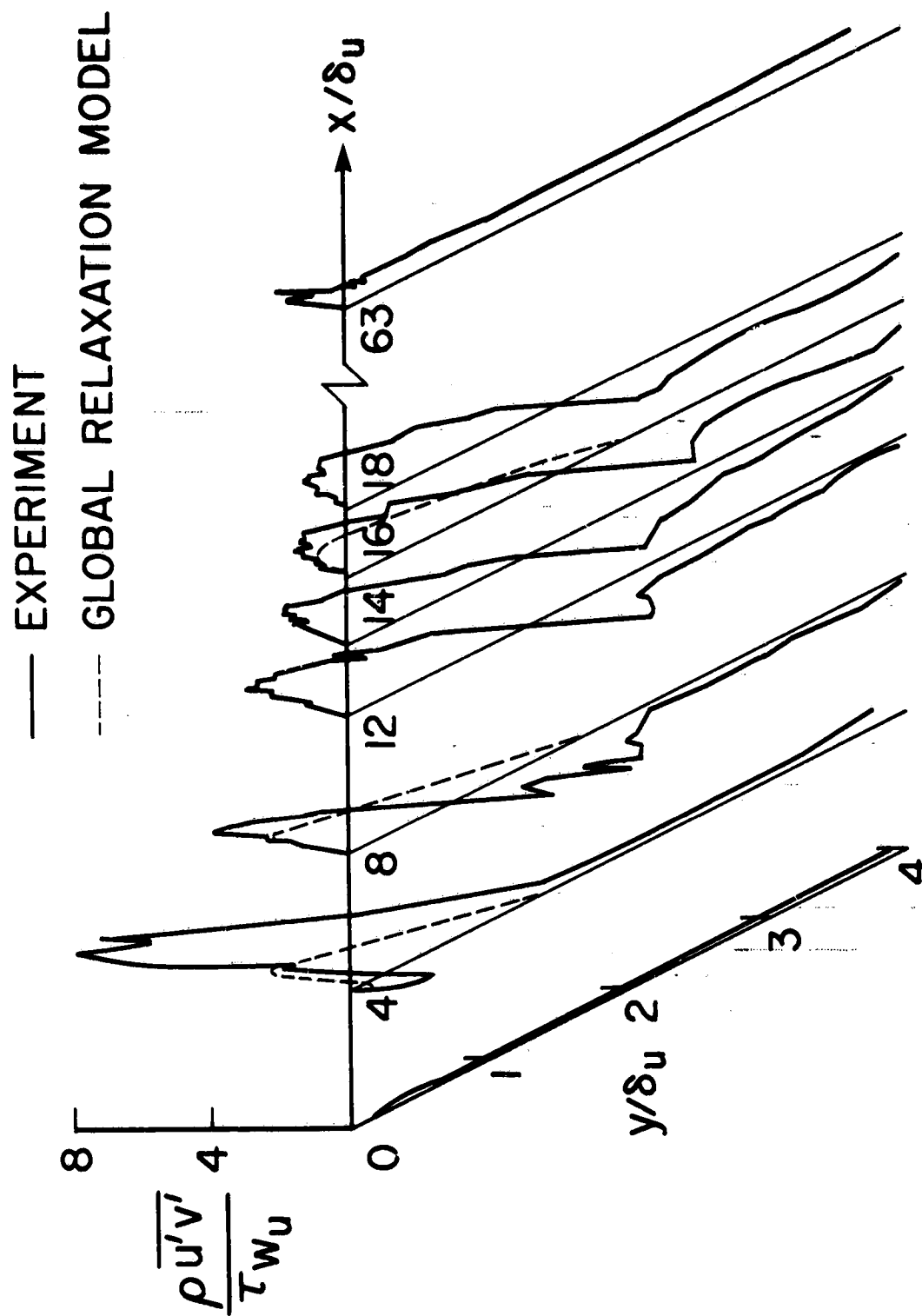


Figure 28.- Shear-stress profiles from the normal shock-wave experiment,
 $M_\infty = 1.44$ and $Re_x = 37 \times 10^6$.

$$M_\infty = 2.96 \quad Re_{\delta_0} = 9.73 \times 10^5$$

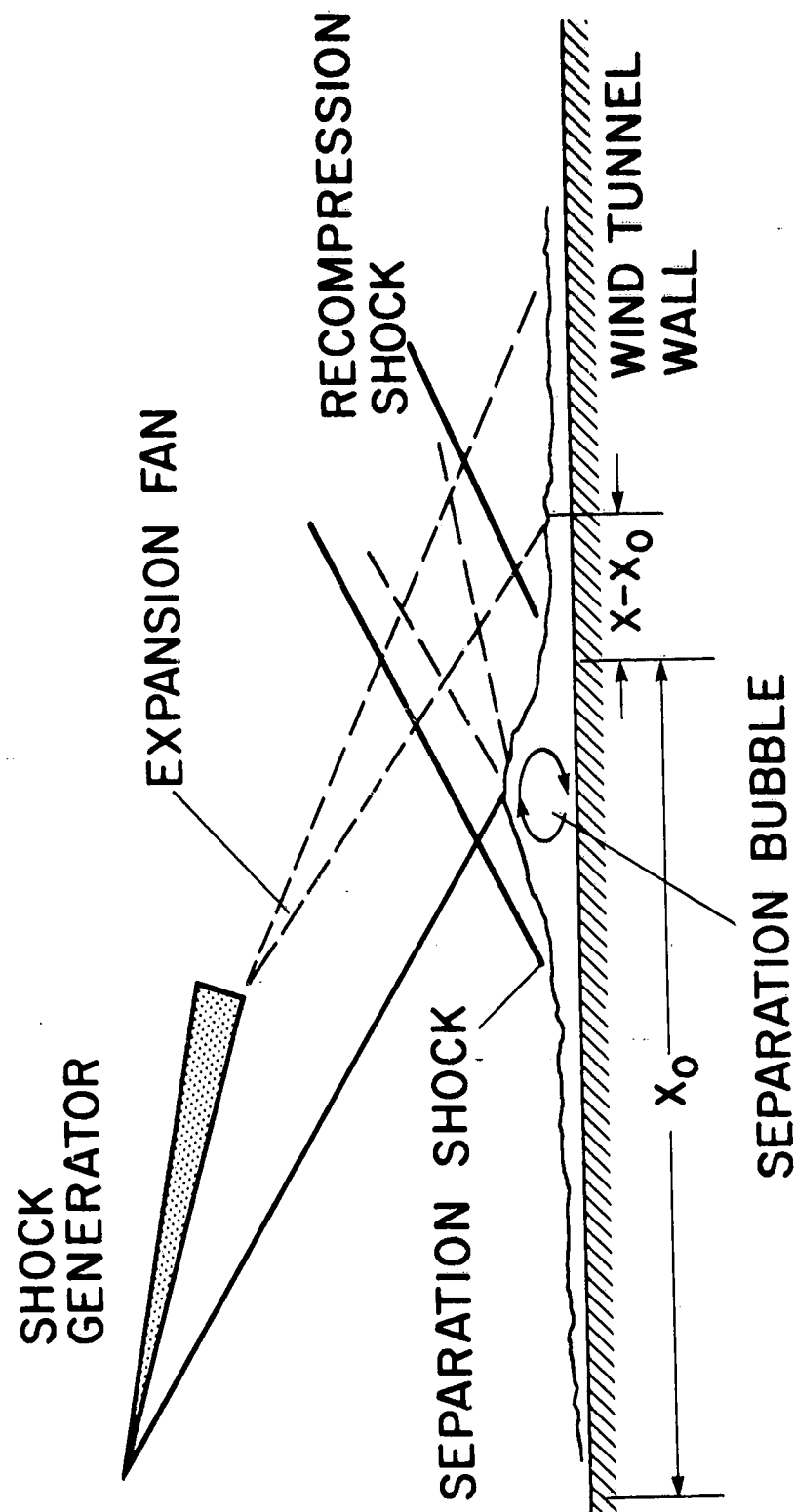


Figure 29.- Experimental arrangement for a supersonic oblique shock-wave, boundary-layer interaction experiment; $M_\infty = 3.0$ and $Re_{\delta_0} = 9.73 \times 10^5$.

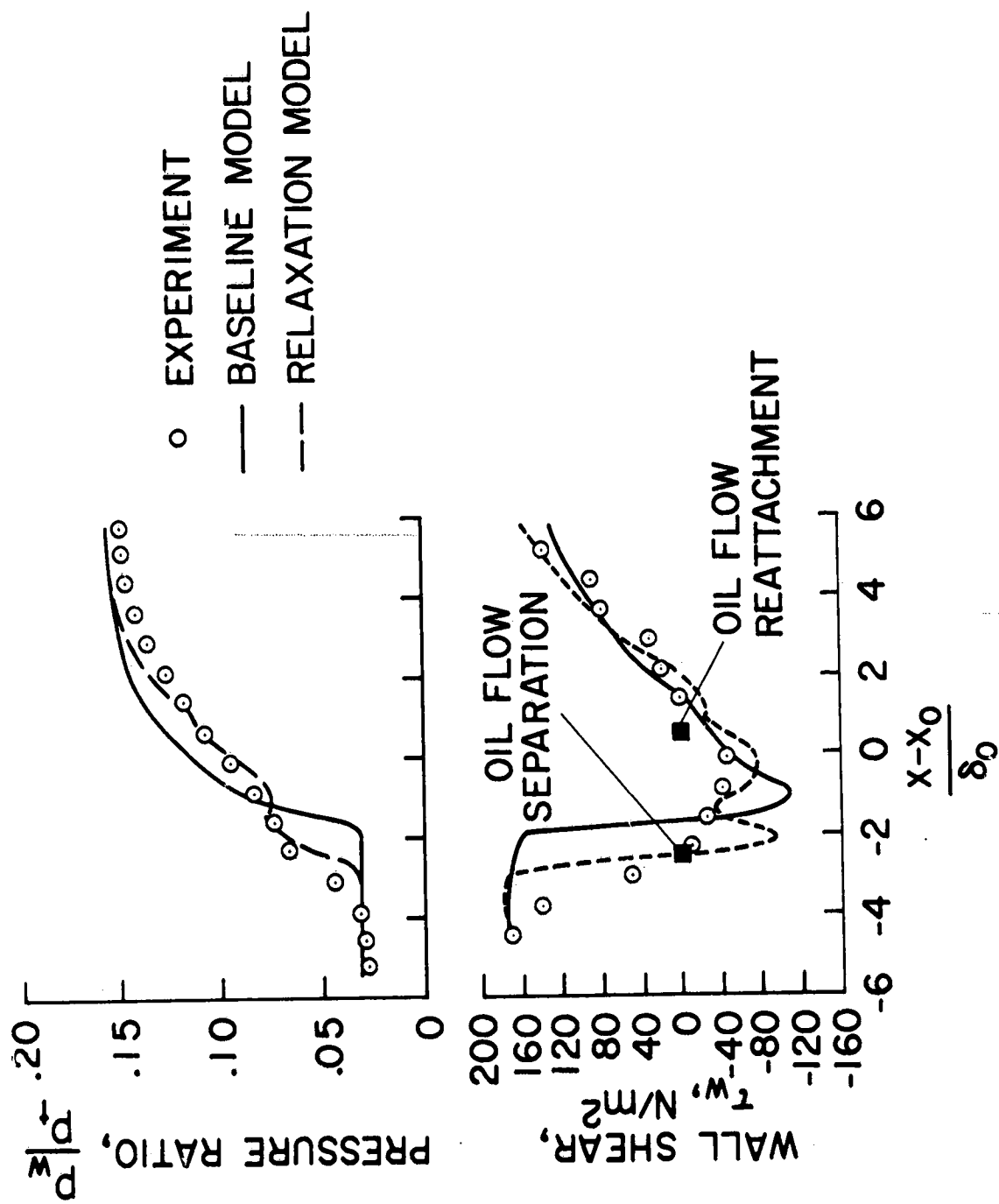


Figure 30.- Results from the supersonic oblique shock-wave, boundary-layer interaction experiment; $M_\infty = 3.0$ and $Re_{\delta_0} = 9.73 \times 10^5$.

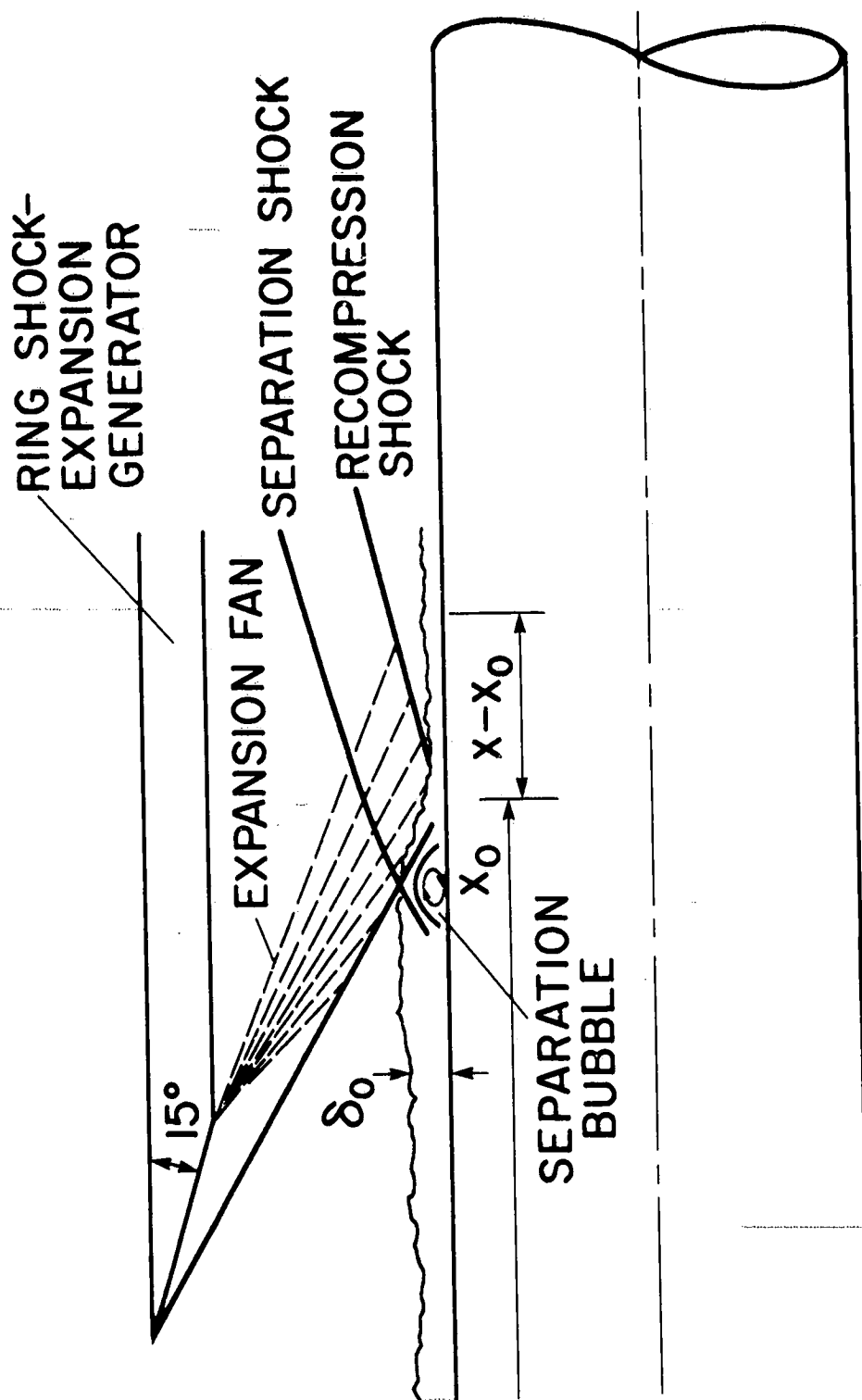


Figure 31.- Experimental arrangement for an axially symmetric hypersonic oblique shock-expansion, boundary-layer interaction experiment; $M_\infty = 6.9$ and $Re_x = 13 \times 10^6$.

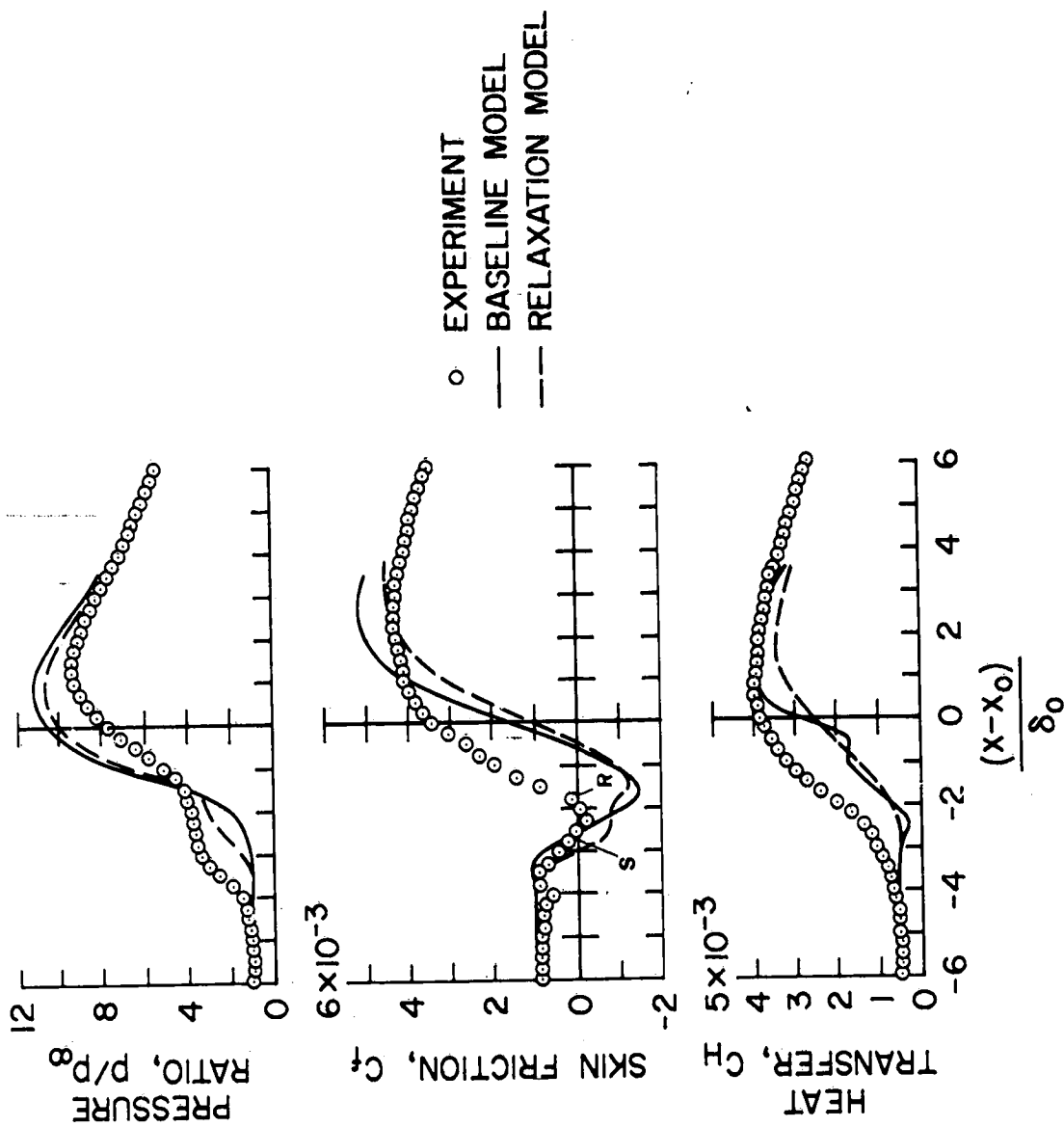


Figure 32.- Results from the hypersonic oblique shock-expansion, boundary-layer interaction experiment; $M_\infty = 6.9$ and $Re_x = 1.3 \times 10^6$.

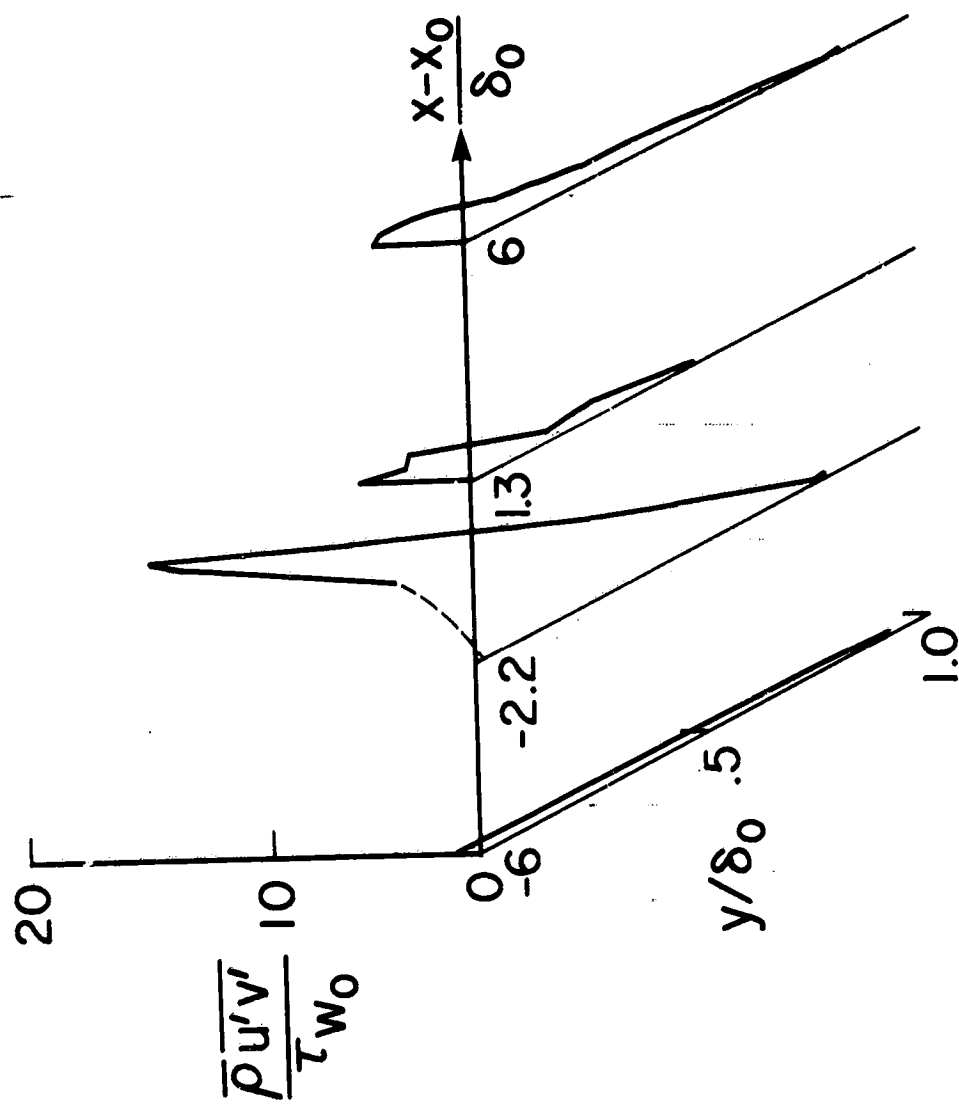


Figure 33.- Shear-stress distributions for the hypersonic oblique shock-expansion, boundary-layer interaction experiment; $M_\infty = 6.9$ and $Re_x = 13 \times 10^6$.

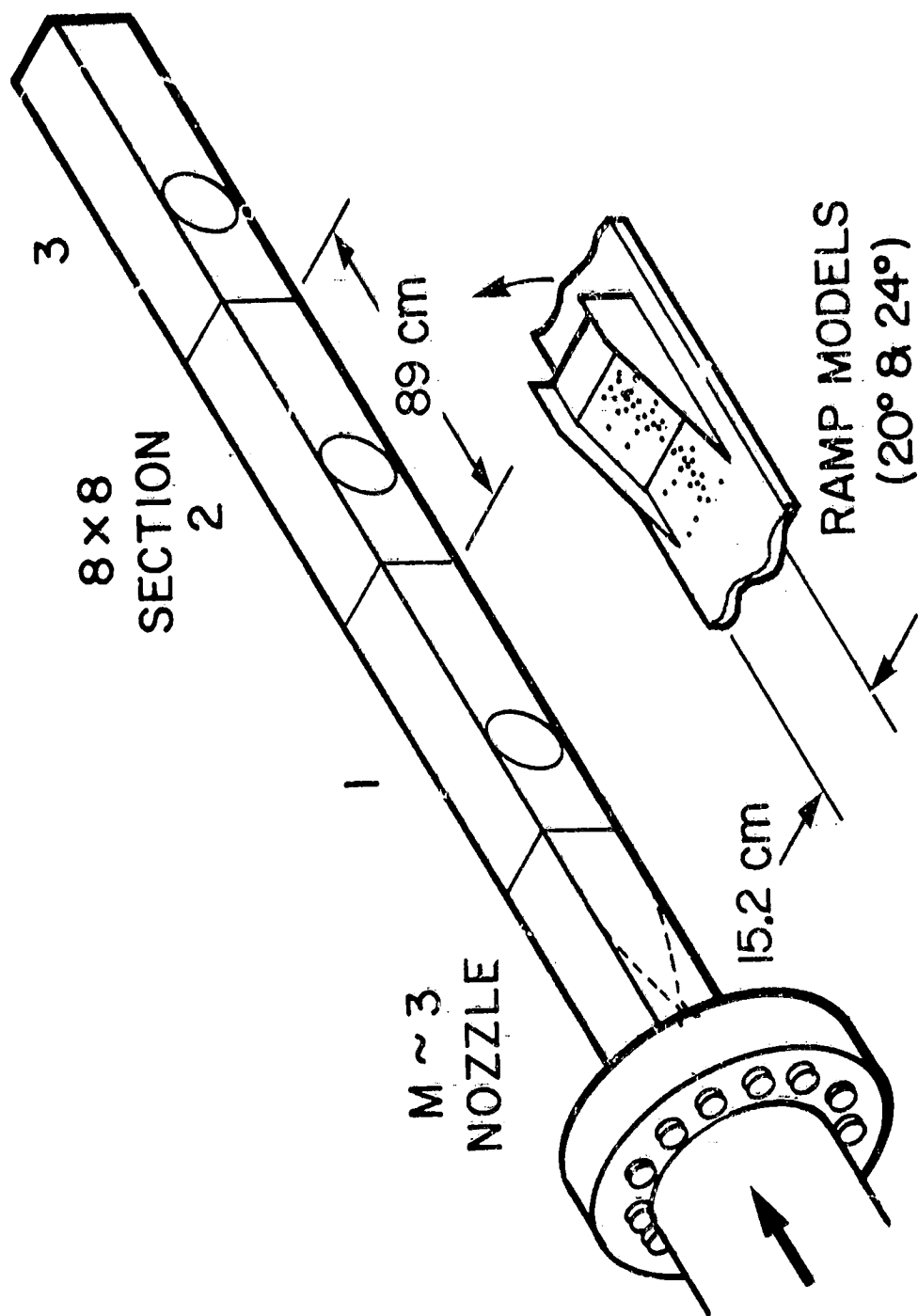


Figure 34.- Sketch of 8- by 8-in. supersonic wind-tunnel and test model.
(Taken from ref. 52.)